Mon. Not. R. Astron. Soc. **000**, 1–40 (2006) Printed 1 February 2008 (MN LATEX style file v2.2)

Spatially resolved kinematics and stellar populations of brightest cluster and group galaxies

S. Brough[1⋆], Robert Proctor[1], Duncan A. Forbes[1], Warrick J. Couch[1], C. A. Collins[2], D. J. Burke[3], R. G. Mann[4]
[1] *Centre for Astrophysics and Supercomputing, Swinburne University of Technology, Hawthorn, VIC 3122, Australia*
[2] *Astrophysics Research Institute, Liverpool John Moores University, Egerton Wharf, Birkenhead, CH41 1LD, UK*
[3] *Harvard-Smithsonian Center for Astrophysics, 60 Garden Street, Cambridge, MA 02138, USA*
[4] *SUPA, Institute for Astronomy, University of Edinburgh, Royal Observatory, Blackford Hill, Edinburgh, EH9 3NJ, UK*

Accepted... Received...; in original form 2006

ABSTRACT
We present an examination of the kinematics and stellar populations of a sample of 3 Brightest Group Galaxies (BGGs) and 3 Brightest Cluster Galaxies (BCGs) in X-ray groups and clusters. We have obtained high signal-to-noise Gemini/GMOS (Gemini South Multi-Object Spectrograph) long-slit spectra of these galaxies and use Lick indices to determine ages, metallicities and α-element abundance ratios out to at least their effective radii. We find that the BGGs and BCGs have very uniform masses, central ages and central metallicities. Examining the radial dependence of their stellar populations, we find no significant velocity dispersion, age, or α-enhancement gradients. However, we find a wide range of metallicity gradients, suggesting a variety of formation mechanisms. The range of metallicity gradients observed is surprising given the homogeneous environment these galaxies probe and their uniform central stellar populations. However, our results are inconsistent with any single model of galaxy formation and emphasize the need for more theoretical understanding of both the origins of metallicity gradients and galaxy formation itself. We postulate two possible physical causes for the different formation mechanisms.

Key words: Galaxies: clusters: general – galaxies: elliptical and lenticular, cD – galaxies: evolution – galaxies: formation

1 INTRODUCTION

Large, bright, elliptical galaxies are found at the centres of most galaxy clusters. These brightest cluster galaxies (BCGs) are the most luminous stellar systems known, yet their intrinsic luminosities are remarkably uniform. Their luminosity and photometric uniformity mean that they do not appear to be the bright extension of the luminosity function of other cluster galaxies (Bernstein & Bhavsar 2001). The position of these galaxies at the centre of clusters and their unique properties link their formation and evolution to that of their environment. However, the mechanisms behind their growth are still poorly understood. Hierarchical models of galaxy formation (e.g. de Lucia & Blaizot 2006; henceforth dLB) suggest that these most massive galaxies should have assembled more recently than other galaxies, with those in the densest environments of galaxy clusters being at a later stage in their evolution to those in the lower density environments of galaxy groups. Understanding the processes by which these galaxies form and evolve is, therefore, vital to the understanding of how both galaxies and clusters form and subsequently evolve.

The studies of Collins & Mann (1998), Burke et al. (2000) and Brough et al. (2002) compared the K-band properties of BCGs with the X-ray luminosities of their host clusters. Near-infrared luminosities are dominated by long-lived stars, such that these wavebands are more sensitive to the underlying stellar mass of galaxies than shorter wavelengths. Cluster X-ray luminosity is directly proportional to the square of the density of the intra-cluster medium and provides a quantitative and objective measure of environmental density. Brough et al. (2002) observed that BCGs in the most X-ray luminous clusters ($L_X > 1.9 \times 10^{44}$ erg s^{-1} [0.3−3.5 keV]) have uniform absolute magnitudes (after correction for passive evolution) over redshifts $0.02 < z < 0.8$. This suggests that they have not experienced any significant stellar mass evolution, beyond that expected for passive evolution, since a redshift ~ 1. In contrast, the absolute magnitudes of BCGs in less X-ray luminous clusters show significant scatter suggesting that they have increased

⋆ E-mail: sbrough@astro.swin.edu.au

their mass by up to a factor ~ 4 over the same timescale. An analysis of the structure of the low-redshift ($z < 0.1$) BCGs adds further evidence of environmentally dependent evolution: BCGs in high-L_X clusters have larger radii with fainter mean surface brightnesses than those in low-L_X clusters (Brough et al. 2005). This suggests that the BCGs in high-L_X clusters have undergone more accretion than those in low-L_X clusters. Taken together with the analysis of the magnitudes, these results suggest that BCGs in high-mass clusters assembled their stellar mass at redshifts > 1 (i.e. ~ 8 Gyrs ago), and have been passively evolving since, in contrast to BCGs in low-mass clusters which appear to still be in the process of assembling today. This picture is consistent with models of hierarchical structure formation.

Another important prediction of the hierarchical structure formation model is that BCGs originate in groups - where they are the brightest group galaxies (BGGs), generally observed to be large ellipticals (Zabludoff & Mulchaey 1998; Osmond & Ponman 2004; Brough et al. 2006). As the groups fall into clusters, the BGG sinks to the bottom of the potential well by dynamical friction and merges with the central galaxy. In Brough et al. (2006) we found that, while the luminosity of the BGG correlates with its total group luminosity, the fraction of group luminosity contained in the BGG decreases with increasing total group luminosity. This suggests that BGGs themselves grow in step with their host group, but at a slower rate than the group.

These observations give indirect evidence for the hierarchical structure formation paradigm with BCGs in low-mass clusters having undergone accretion events since $z \sim 1$, possibly from mergers with infalling BGGs. However, confirming the paradigm requires direct evidence that BCGs have undergone mergers. We can use the predictions of dLB to do this in a quantitative fashion. Their study uses merger trees from the Millennium cosmological N-body simulation (Springel et al. 2005) as an input for their semi-analytic model which includes a model for the suppression of cooling flows by AGN feedback. The model is described in more detail in de Lucia et al. (2006). dLB predict that the stars that will end up in the BCG form at high redshift (with 50 per cent of the stars having formed by $z \sim 5$, i.e. they are now 12.5 Gyrs old), the BCGs then evolve through the accretion of old, passive galaxies of mass $> 10^{10} M_{\odot}$, with ~ 50 per cent of the mass of the eventual BCG not *assembling* until $z \sim 0.5$, i.e. ~ 5 Gyrs ago. The late mergers are not predicted to significantly change the ages or metallicities of the BCGs because the progenitor galaxies are predicted to be massive, old, metal-rich, gas-poor galaxies themselves. dLB also show that the BCG mass grows in step with the growth in mass of the cluster. We therefore assume that observing BCGs in clusters with a range in mass (down to group-sized systems) is equivalent to observing them at different stages in their evolutionary history.

The stellar populations of galaxies provide us with a means by which to determine their evolutionary histories. The populations are a result of many factors including the efficiency of star formation, gas fraction, gas dissipation and possible interactions with other galaxies. This information should leave imprints in the radial distributions of these populations and the different models of galaxy formation make different predictions of the radial dependence of the stellar populations:

In classic models of dissipative collapse (e.g. Eggen et al. 1962; Larson 1974; Carlberg 1984; Arimoto & Yoshii 1987), stars form during the collapse and remain in their orbits, while gas dissipates to the centre of the galaxy, being continually enriched by the evolving stars as it does so. This results in stars in the centres of galaxies being more metal-rich than those in the outer regions. In the models the degree of dissipation is controlled by the size of the potential well. The continuous enrichment by evolving stars means that the centres are less α-element enhanced (i.e. the ratio of the abundance of α-elements to the abundance of iron-peak elements is $>$ solar; Thomas et al. 2003) than the outer regions, unless the collapse, and star formation, occur over very short timescales. The observed central α-element enhancement ratios in galaxies require collapse times $\leqslant 1$ Gyr (Arimoto & Yoshii 1987; Matteucci 1994). More recent numerical models of dissipative collapse (e.g. Martinelli et al. 1998; Chiosi & Carraro 2002; Kawata & Gibson 2003) show that the observed chemical abundances can be obtained by assuming that metallicity gradients are established by the onset of a galactic wind which varies depending on the local depth of the potential well. Dissipative collapse, therefore predicts strong negative metallicity gradients (i.e. metallicity decreases with increasing radius) that correlate with galaxy mass (Chiosi & Carraro 2002; Kawata & Gibson 2003), negative α-element enhancement gradients, and small positive to null age gradients (due to the speed of the collapse).

Simulations of the hierarchical formation of galaxies (e.g. dLB, de Lucia et al. 2006) predict that massive elliptical galaxies are produced by mergers. Early numerical simulations of the properties of merger remnants suggested that mergers lead to a flattening of the metallicity gradients (White 1980). However, van Albada (1982) suggested that the gradients of the progenitor galaxies are not heavily affected as violent relaxation preserves the position of the stars in the local potential. More recent simulations including gas physics suggest that the gradients of the remnant depend on the amount of gas present in the merger. The predicted signatures of gaseous (dissipative) mergers are qualitatively similar to the dissipative collapse models described above as a significant fraction of the gas in the progenitor galaxies is funnelled towards the central regions of the merger remnant, resulting in a starburst (Barnes 1991). Starbursts can also produce metallicity gradients, although those produced by Bekki & Shioya (1999) in their dissipative merger simulation are shallower than those found for dissipative collapse models. Kobayashi (2004) simulated the formation of ellipticals in a cold-dark matter cosmology, examining the effects of dissipative collapse, and dissipative and dissipationless mergers on the chemodynamical evolution of ellipticals. She found that galaxies of given mass had steep metallicity gradients if formed by collapse and shallower gradients (a few Gyrs after the merger) if formed by a major merger (dissipative or not). Therefore, hierarchical galaxy formation models predict negative metallicity gradients that are shallower than those predicted by dissipative collapse models. Depending on the duration and location of the starburst and the original α-element enhancement of the gas, the resulting α-element enhancement ratio and age gradients of the merger remnant can be either positive or negative (e.g. Thomas & Kauffmann 1999)

If environment has an effect on the star formation, the number of interactions a galaxy undergoes, or the dissipation of gas within the galaxy's potential well, we would expect to see an environmental dependence on the inferred stellar population gradients.

The theoretical models indicate that the radial structure of a galaxy provides a fossil record of its evolutionary history. Therefore, studying the radial kinematics and stellar populations of BGGs and BCGs and their dependence on environment will enable us to determine their merger history. If the predictions of dLB are correct we would expect to see evidence of dissipationless mergers in these galaxies; i.e. little dependence of metallicity on system mass and no evidence of star formation in the last 5 Gyrs. As the BCGs are predicted to be at a later stage of their evolution than the BGGs, we would also expect evidence that the BCGs have undergone more mergers than the BGGs. This would predict, for example, shallower metallicity gradients in the BCGs and the velocity dispersions of the BGGs/BCGs increasing with increasing group/cluster mass.

There have been few studies of the kinematics and stellar populations of BCGs and fewer that are spatially resolved to enable a study of radial trends. Forbes et al. (2001) found the BCG in the Fornax cluster, NGC 1399, to be old (10 ± 2 Gyrs). In studies of radial gradients, Gorgas et al. (1990) found that the Mg_2 gradients of 3 BCGs are shallower than the mean gradient of normal ellipticals, suggesting that BCGs have undergone more mergers than normal elliptical galaxies. In contrast, Davidge & Grinder (1995) found the D4000 gradients of 6 BCGs to be steeper than for non-BCGs, suggesting that BCGs experienced dissipative collapse and cannot have formed solely through mergers with passive galaxies. The study of 13 BCGs by Fisher et al. (1995a) found that the velocity dispersion profiles of BCGs were similar to those in normal elliptical galaxies. Fisher et al. (1995b) examined the line strengths of 9 of the 13 BCGs presented in Fisher et al. (1995a) and found that BCGs follow the same Mg*b* – velocity dispersion ($\sim$ metallicity – mass) and [Mg/Fe] – velocity dispersion ($\sim$ α-element enhancement – mass) relationships as normal elliptical galaxies. The Hβ gradients of their sample are flat, and combined with declining Mg*b* gradients, suggest that BCGs are younger in their centres than in their outer regions. Carter et al. (1999) found similar results in their sample of 3 BCGs. Mehlert et al. (2003) calculated stellar population gradients for the two cD galaxies in the Coma cluster, finding shallow age gradients, shallow metallicity gradients, and no α-element enhancement ratio gradients, consistent with their results of other early-type galaxies in Coma. The results from metallicity gradients are clearly contradictory while the other relationships are generally consistent with BCGs sharing similar properties and, therefore, a similar evolutionary history, to normal early-type galaxies. However, these samples only cover a limited environmental range and only a few studies have data that extend to the effective radius (r_e; the radius containing half the light) of these galaxies.

In this paper we test whether BCGs evolve hierarchically by examining high signal-to-noise, Gemini long-slit spectra for a sample of 3 BGGs and 3 BCGs in X-ray groups and clusters spanning an unprecedented range in X-ray luminosity and hence environmental density ($10^{40} < L_X$ ergs^{-1} $< 10^{45}$). Our aim is not to compare BGGs with BCGs; instead we are using the range in system X-ray luminosity to observe these galaxies at different stages in their evolutionary history. Observing the same systems over a range of look-back times would require going to redshifts that are too high for a detailed stellar population analysis to be conducted. However, we do note that it is possible that these galaxies are at different stages of their evolution and *also* in different environments. If this is so then we might expect the properties of BGGs and BCGs to show scatter in their relationships and not to depend on their environment.

We build on previous studies by examining galaxies in a wider range of environments and by measuring their spectral properties out to at least 1 effective radius. We also use the multi-index χ^2-fitting technique of Proctor & Sansom (2002; see also Proctor et al. 2004a,b, 2005) to measure their stellar populations. The rationale behind this technique is that all the indices defined in the Lick system have *some* sensitivity to both age *and* metallicity. Using them all together, in conjunction with the best available single stellar population (SSP) models, overcomes uncertainties in both the data reduction and from the SSP models themselves. Proctor et al. (2004b) demonstrate that this method is significantly more reliable than the more widely-used technique of using only single or a few indices at a time.

This is the first in a series of papers studying the kinematics and stellar populations, and their gradients, in BGGs and BCGs. At present we only have a small sample of 6 galaxies. It is therefore not possible to determine whether these galaxies follow statistically significant correlations. However, the sample is useful for an initial identification of trends that might be germane to the aforementioned issues.

We introduce our sample in Section 2 and the observations made and data reduction process in Section 3. In Section 4 we discuss our method for extracting the kinematics, Lick indices and ages and metallicities for these data. In Section 5 we discuss the results we obtain for individual galaxies before studying the relationships between the sample in Section 6 (environment), Section 7 (central stellar populations) and Section 8 (stellar population gradients). We draw our conclusions in Section 9. Throughout this paper we assume $H_0 = 70$ km s^{-1} Mpc^{-1}, $\Omega_m = 0.3$ and $\Omega_\Lambda = 0.7$.

2 SAMPLE

The BGG and BCG galaxy samples were selected from the Group Evolution Multi-wavelength Study (GEMS; Osmond & Ponman 2004; Forbes et al. 2006) and the BCG sample presented in Brough et al. (2005). In both these samples the galaxy is selected as the brightest galaxy closest to the X-ray centroid, i.e. closest to the centre of the potential well of these structures. The specific galaxies were chosen to be accessible within the Gemini telescope's 'A' (February–July) observing semester and to cover a wide range in group/cluster X-ray luminosity. The sample of galaxies studied and the properties of their host group/cluster systems are summarised in Table 1.

The absolute magnitudes given in Table 1 are calculated from the total K_s-band magnitudes (henceforth denoted as K) given in the 2-micron All Sky Survey Extended

Source Catalogue (2MASS; Jarrett et al. 2000). There are no independent distance measurements for our BCGs. We, therefore, convert to absolute magnitudes using luminosity distances (given in Table 1) calculated from the measured central recession velocities and our choice of cosmology . Due to the scatter in the absolute magnitudes of this sample, it makes no difference to our results if we use luminosity distances for the BGGs or those based on distance moduli from surface brightness fluctuation studies by Tonry et al. (2001). The magnitudes are then K+E-corrected (i.e. also corrected for passive evolution; Yoshii & Takahara 1988), using spectral energy distributions produced by the GISSEL96 stellar population synthesis code (Bruzual & Charlot 1993), assuming that the galaxies are 10 Gyrs old and formed in an instantaneous burst, and have evolved passively since $z \sim 2$. The correction is only -0.2 mag for our most distant galaxy (2MASX J10172568-1041206 at $z \sim 0.054$) and the assumptions of age and redshift of formation have negligible effect on the correction value. The magnitudes were also corrected for galactic absorption using the maps of Schlegel et al. (1998), these corrections are $A_K \sim 0.02$ mag.

We take cluster X-ray luminosities from the *ROSAT*-ESO Flux-Limited X-ray galaxy cluster catalogue (REFLEX; Boehringer et al. 2004). These are calculated from the *ROSAT* [0.1-2.4 keV] band and extrapolated to 12 times the core radius of the cluster. Our group X-ray luminosities are taken from the GEMS group catalogue (Osmond & Ponman 2004). These luminosities are bolometric and extrapolated to the radius corresponding to an overdensity of 500 times the critical density – r_{500}. There is one object in common between the two samples: the NGC 5044 group. This group has Log $L_{X,GEMS} = 43.09 \pm 0.01$ (ergs^{-1}) and Log $L_{X,REFLEX} = 43.04$ (ergs^{-1}). REFLEX do not provide errors on their X-ray luminosities. Therefore, we assume that the two catalogues are consistent within errors of $\Delta\mathrm{Log}(L_X) = 0.05$ dex.

The 3 BCGs are henceforth referred to by the name of their clusters i.e. 2MASX J09083238-0937470 – A754#1; 2MASX J10172568-1041206 – A970#1; MCG -01-27-002 – A978#1.

3 OBSERVATIONS AND DATA REDUCTION

We observed the 6 galaxies using the Gemini Multi-Object Spectrograph (GMOS) on the Gemini (South) telescope in long-slit mode. All 6 galaxies were observed in queue mode in early 2005; the observation parameters are summarised in Table 2. The galaxies cover a range of surface brightnesses and the exposure times reflect this.

Table 2 also gives the position angle (PA) that these galaxies were observed at, and their respective major axis, from 2MASS. We note that the spectra of NGC 3557 and NGC 5044 were taken at the position angles of their major axis whilst the spectra of NGC 3640, A754#1, A970#1 and A978#1 were taken at position angles other than their major axis, in an attempt to avoid other galaxies lying on the slit. This has an effect on the relative sizes of the galaxies at these position angles. We therefore also give the effective radius along the semi-major axis, r_e, of the galaxies. This is calculated from the 2MASS K-band 20$^{\mathrm{th}}$ magnitude arcsec^{-2} isophotal radius, r_{K20}: Jarrett et al. (2003) show that this is proportional to r_e, as Log $r_e \sim$ Log $r_{K20} - 0.4$. This was transformed to an effective radius at the PA we observed, a_e, using the ellipticities of the galaxies (also from 2MASS Jarrett et al. 2003):

$$a_e = \frac{r_e(1-\epsilon)}{1-\epsilon\cos(|PA-MA|)} \quad (1)$$

We also indicate the fraction of a_e our radial profiles span and note that the profiles of all our galaxies extend beyond $1a_e$.

The GMOS slit is $5.5'$ long and we used a slit width of $0.5''$ with the B600 grating. The data were binned by 2 in both the spatial and spectral directions. This set-up gave a dispersion of 0.9 Å pixel^{-1} and a spectral resolution of ~ 3.4Å full width at half-maximum (FWHM; ~ 80 kms^{-1}). The seeing was generally $\leqslant 1''$ and the binned pixel scale was $0.15''$ pixel^{-1}. The total wavelength range covered is $\sim 3700 - 6700$Å .

We used the GEMINI/GMOS tasks in IRAF for basic data reduction. The data were then binned in the spatial direction using the STARLINK/FIGARO package EXTRACT, to guarantee a minimum signal-to-noise ratio per Å (S/N) of 60 (with the exception of A970#1, where only a S/N of 30 was possible) at the wavelength of the $H\beta$ line. We also extracted a central aperture of size $a_e/8$ and our slit-width of $0.5''$. Reliable index estimates were obtained for 22 Lick indices from $H\delta_A$ to Fe5782 (Trager et al. 1998).

Neither Lick index nor flux calibration standards were observed for this program. We therefore used standards observed on a different program using the same GMOS grating in multi-object spectroscopy mode (Pierce et al. 2006; c.f. Proctor et al. 2005). These stellar templates were used to calculate the kinematic properties of the galaxies.

The spectra of the central aperture of each galaxy are illustrated in Figure 1.

4 ANALYSIS

4.1 Kinematics

Determination of the recession velocities and velocity dispersions was carried out by cross-correlating the galaxy spectra with the stellar spectra, using the IRAF package FXCOR. As emission lines could affect the measurement of the kinematics we manually excised emission lines from the spectra using the IRAF task *splot* for this measurement.

We measured velocity dispersions in the central aperture of size $a_e/8\times$ our slit-width of $0.5''$. These are given in Table 3, along with values from the literature. The table also indicates that the literature values are all measured in apertures of different sizes. We therefore use the equations provided in Jørgensen et al. (1995) to adjust their apertures to the size used here: $a_e/8$. The corrected literature values are also given in Table 3.

An accurate comparison of the central value for the velocity dispersion with literature values is difficult due to the wide range in systematic errors between studies. However, we observe an absolute mean difference between our values and the literature values corrected to our aperture (Table 3) of 21 ± 8 kms^{-1} (Figure 2). This is slightly larger than the statistical errors and provides a measure of the systematic error on our measurements. The corrected literature values

Table 1. A summary of the properties of the sample of galaxies.

Galaxy	System	RA (J2000)	Dec (J2000)	Distance (Mpc)	M_K (mag)	Log (L_X) (erg s^{-1})
NGC 3557	NGC 3557	11:09:57.4	-37:32:17	44.2	-24.54±0.01	42.11±0.05
NGC 3640	NGC 3640	11:21:06.9	03:14:06	19.2	-23.90±0.02	< 40.74
NGC 5044	NGC 5044	13:15:24.0	-16:23:06	39.6	-25.28±0.02	43.09±0.05
2MASX J09083238-0937470	Abell 754	09:08:32.3	-09:37:48	245.1	-26.56±0.05	44.63±0.05
2MASX J10172568-1041206	Abell 970	10:17:25.6	-10:41:20	261.3	-25.39±0.09	44.00±0.05
MCG -01-27-002	Abell 978	10:20:26.5	-06:31:36	264.1	-26.50±0.07	43.43±0.05

The columns indicate (1) galaxy name, (2) Group (NGC) or cluster (Abell) name, (3,4) the position of the galaxy, (5) the luminosity distance to the galaxy, (6) Absolute total K-magnitude from 2MASS corrected for galactic extinction and evolution as described in the text, with 1σ error, (7) System X-ray luminosity and assumed 1σ error.

Table 2. Observing parameters and relative galaxy sizes.

Name	Exp. Time (s)	PA (degrees)	MA (degrees)	r_e ($''$)	ϵ	a_e ($''$)	Fraction
NGC 3557	3×1200	31	31	36.7	0.25	36.7	1.23
NGC 3640	3×900	80	95	36.6	0.2	25.4	1.77
NGC 5044	5×1800	20	20	24.3	0.08	24.3	2.06
A754#1	3×1800	96	125	10.0	0.3	5.7	3.68
A970#1	3×1800	177	45	4.4	0.08	4.4	1.60
A978#1	4×1800	18	10	8.4	0.2	6.6	2.13

The columns indicate (1) galaxy name, (2) exposure time, (3) observed position angle, (4) position angle of major axis from 2MASS, (5) effective radius of major axis, r_e, calculated from 2MASS K-band 20$^{\rm th}$ magnitude arcsec^{-2} isophotal radius, (6) ellipticity of galaxy, from 2MASS, (7) effective radius along observed position angle, a_e, (8) fraction of a_e our radial profiles extend to.

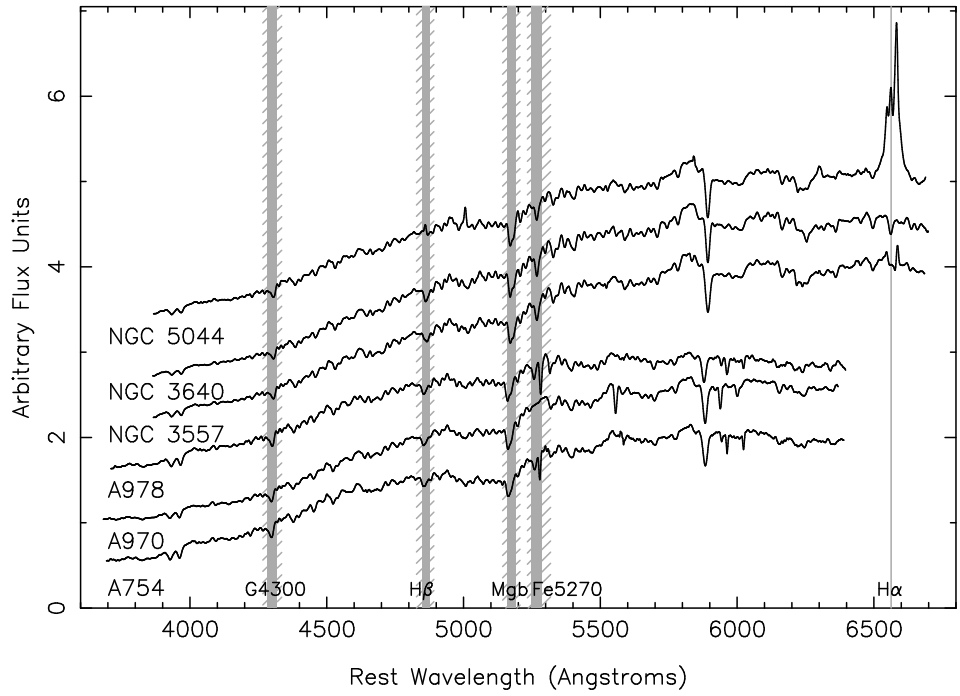

Figure 1. The central spectra for all 6 galaxies, adjusted to the restframe. The flux scale is arbitrary. The blue and red continuum (hashed regions) and central bands (solid regions) of several important Lick indices are also indicated for information.

Table 3. Central kinematics measured within an aperture of $a_e/8$ and a slit width of 0.5″ and literature values.

Name	V_o (kms^{-1})	σ_o (kms^{-1})	$\sigma_{\rm lit}$ (kms^{-1})	Aperture Size (″)	$\sigma_{\rm lit,corr}$ (kms^{-1})
NGC 3557	3072± 8	282± 16	244± 9 (F)	LS 1×1.5	226± 8
NGC 3640	1341± 5	154± 6	178± 9 (D)	LS 2.5×1.5	171± 9
NGC 5044	2755± 12	223± 6	240±13 (C)	LS 3×1.5	231± 13
A754#1	16468± 11	309± 14	323±19 (G)	LS 2×4	334± 20
A970#1	17512± 6	264± 15	238±13 (S)	F 2	242± 13
A978#1	17695± 15	274± 19	260±25 (O)	LS 8×2	271± 26

The columns indicate (1) galaxy name, (2) central recession velocity, (3) central velocity dispersion,(4) Previously measured velocity dispersion from F (Franx et al. 1989), D (Denicoló et al. 2005), C (Carollo et al. 1993), G (Gorgas et al. 1990), S (Smith et al. 2004), O (Oegerle & Hoessel 1991), (5) Aperture type (long-slit, LS, or fibre, F) and size, (6) literature value, corrected to our aperture size as per text.

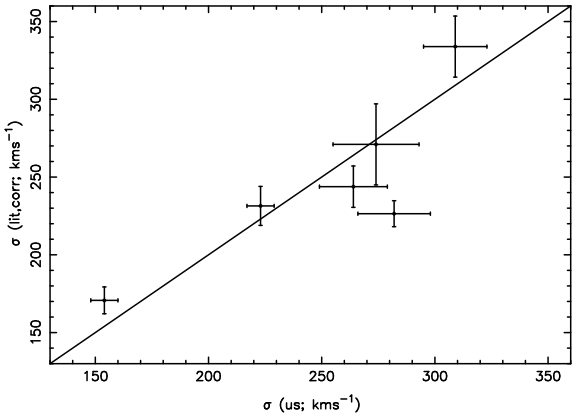

Figure 2. Central velocity dispersion values calculated here compared to values from the literature corrected to our aperture size (given in Table 3). The error bars indicate 1σ errors. The solid line indicates the one-to-one relationship. The absolute mean difference between our values and those of the literature is $|\ \sigma$ (us) - σ (lit., corr)$|= 21 \pm 8$ kms^{-1}.

are illustrated against the observations in Figures 3, 4, 5, 7, 8 and 9

4.2 Indices

Lick indices were measured using the method described in Proctor et al. (2006; see also Proctor et al. 2004a,b, 2005, 2007). Trager et al. (1998) and Worthey & Ottaviani (1997) index definitions were used throughout. The indices were measured at the wavelength-dependent resolution detailed in Worthey & Ottaviani (1997).

The measured indices require correcting for velocity dispersion broadening and differences in flux calibration between the Lick system and these observations. For galaxy apertures whose velocity dispersions, when combined in quadrature with the instrumental broadening, resulted in resolutions higher than that of the relevant index in the Lick system, the spectra are convolved with an appropriate Gaussian prior to index measurement. For apertures whose velocity dispersions, when combined in quadrature with the instrumental broadening, resulted in resolutions lower than that of the Lick system, indices were corrected using a factor interpolated from indices measured in the 5 standard stars after convolving the stellar spectra with a series of Gaussians. Due to the varying resolution across the Lick system and the velocity dispersion profile of galaxies, the second correction is only applied to low resolution indices ($H\beta$ – Fe5406) measured in the central apertures (highest velocity dispersions) of our sample.

To correct for the difference in flux calibration between observations and the Lick system and for the wavelength-dependent resolution of the Lick system, Lick indices are usually measured for Lick library stars and compared to the indices measured in the original Lick system (Worthey et al. 1994). As no Lick standards were observed, we cannot apply these offsets. As a compromise, instead, we use the error in the mean of the offsets measured for 7 Lick standard stars observed by Proctor et al. (2004a) to add a measure of the systematic error due to our lack of flux calibration. The differences are generally smaller than the scatter and the typical rms per observation of the Lick calibrators (Worthey et al. 1994).

The index errors were calculated combining the error from Poisson noise and the uncertainties in recession velocity and velocity dispersion. These are the random statistical errors. We also add, in quadrature, the error on the mean of the offset between the measurements of Lick standard stars and those taken on the Lick/IDS system from Proctor et al. (2004a; Table 4). These provide a measurement of the systematic error due to conversion onto the Lick system and are of the order of the random errors.

The indices and their errors measured for the central apertures are given in Appendix A while the indices and errors measured in the radial apertures are given in Appendix B for each galaxy.

4.3 Stellar Populations

We compare the measured Lick indices to predictions from single stellar population (SSP) models in order to estimate the relative *luminosity-weighted* ages and metallicities of the stellar populations and also the relative abundances of their α-elements. We use the luminosity-weighted α-element enhancement ratio defined by Thomas et al. (2003, 2004) - [E/Fe]. This is a proxy for the ratio of the abundances of

Table 4. Offsets from index measurements to those of the Lick system from Proctor et al. (2004a; P04a).

Index	Units	Lick-P04a	Error in Mean
Hδ_A	Å	0.229	0.226
Hδ_F	Å	-0.153	0.162
CN_1	mag	-0.014	0.013
CN_2	mag	-0.012	0.004
Ca4227	Å	-0.089	0.060
G4300	Å	-0.489	0.079
Hγ_A	Å	-0.253	0.153
Hγ_F	Å	-0.118	0.064
Fe4383	Å	-0.015	0.192
Ca4455	Å	0.070	0.155
Fe4531	Å	-0.382	0.091
C4668	Å	-0.839	0.095
Hβ	Å	-0.052	0.048
Fe5015	Å	-0.104	0.104
Mg_1	mag	0.016	0.004
Mg_2	mag	0.023	0.003
Mgb	Å	0.024	0.043
Fe5270	Å	-0.324	0.090
Fe5335	Å	-0.394	0.077
Fe5406	Å	-0.181	0.045
Fe5709	Å	-0.030	0.052
Fe5782	Å	0.045	0.045

the α-elements to the abundance of the iron-peak elements. Total metallicity is denoted by [Z/H].

The determination of Log (age), [Z/H] and [E/Fe] were carried out by comparison of the observations to the Thomas et al. (2004) SSP models and Korn et al. (2005) index sensitivities. The index sensitivities describe the sensitivity of Lick indices to variations in the chemical abundance ratios, as computed in stellar atmosphere models. The SSP values for each index are interpolated to give a grid of values for $-1 <$ Log (age)$<$ 1.175 dex and $-1.675 <$[Z/H]$<$ 0.5 dex in 0.025 dex steps. For each index, at each Log (age), [Z/H] step, values of the index were also estimated for $-0.3 <$[E/Fe]$<$ 0.6 dex in $\sim$ 0.03 dex steps. The fractional change in each index is calculated assuming that all elements in the enhanced group vary by the same amount relative to the Fe elements. A 3-dimensional grid of model Log (age), [Z/H] and [E/Fe] values are constructed for each index. The best fit Log (age), [Z/H] and [E/Fe] values are then found by simultaneously fitting the 3-dimensional model grids by χ^2 minimization to as many observed index values as possible.

Like many fitting routines we employed a 3σ 'clipping' process so that indices lying $> 3\sigma$ from the model fit are clipped and the fit is re-iterated until there are no indices outside 3σ. Seeking stability, certain further indices were also clipped from the fitting, until removal of no single index resulted in changes significantly different from that implied when including the clipped index.

The main causes for clipping further indices were:

(1) The GMOS long-slits have two small bridges, of width $3''$, which result in gaps in the spectra - henceforth termed as 'chip gaps'. Depending on the redshift of each galaxy, we changed the blaze wavelength of the slit, so as to move these chip gaps into wavelength ranges without indices. However, this was not always successful and some indices were lost as a result.

(2) Sky-line residuals lying in regions an index is redshifted into.

(3) Indices whose passbands lie at some distance from the index itself (e.g. CN_2, G4300, Mg_1, Mg_2) are subject to their continuum being incorrectly estimated, relative to the index, if the data are not flux calibrated.

(4) Emission lines contaminate the absorption indices, particularly the Balmer lines and Fe5015. We chose not to use simplistic corrections to the absorption indices to resolve this issue due to their intrinsic uncertainties (Nelan et al. 2005; Kuntschner et al. 2006). Furthermore, the multi-index fitting method we are using enables us to measure ages from the combined age dependencies of the remaining indices (Proctor et al. 2004a).

The extra indices clipped and the reasons for doing so are summarised in Table 5.

The errors on the stellar population values were calculated by means of a Monte Carlo analysis: the model indices associated with the fitted Log (age), [Z/H] and [E/Fe] value were extracted and a Gaussian of width equal to the observed index errors was applied to each index. Index values were then drawn at random from that distribution and the stellar populations refitted. This was repeated 50 times and the rms of the values derived gives the errors we present below.

Previous authors examining GMOS long-slit data have noted that scattered light in the spectrograph is a significant problem that would compromise their index measurements (Norris et al. 2006), while Proctor et al. (2005) have shown that scattered light made negligible difference to their results. Scattered light would have the effect of lowering measured index values by applying a constant offset to the spectra, which would lead to incorrect age gradients at large radii. It is possible to examine the effects of this problem as the 2-dimensional GMOS spectrum contains 3 unexposed regions: at the bottom of the slit and 1/3 and 2/3 of the distance along the spatial direction of the image. After bias subtraction these regions should contain no flux, such that any scattered light will be evident here. Norris et al. (2006) solve this problem by interpolating across the three unexposed regions and subtracting that level from the image. We fitted a Gaussian to the three unexposed regions in our closest galaxy, NGC 3640, and subtracted that Gaussian from the 2-dimensional image. We then proceeded with our analysis as described above. We found that, with the exception of the outermost aperture, the kinematics and stellar populations measured were within the errors of our original measurements. We therefore conclude that scattered light in the GMOS spectrograph has negligible effect on the results presented below.

The derived central (within an $a_e/8$ aperture and a slit-width of $0.5''$) velocities and velocity dispersions are given in Table 3 and central ages, metallicities and α-index enhancements in Table 6. We note that the central values and the results we obtain are consistent, within the errors, for values measured within $r_e/8$. The observed radial aperture measurements are given in Appendix C and are plotted in Figures 3, 4, 5, 7, 8 and 9. The Figures illustrate the data at the position angle they were observed at. We have indicated the observed PA and illustrated the effective radius at those

Table 5. A summary of indices clipped from the stellar population analysis of each galaxy.

Galaxy	Chip Gap	Sky Line	Flux Calibration	Emission
NGC 3557	C4668, Fe5782		CN_2, G4300	
NGC 3640			$H\delta_A$, CN_1, CN_2, G4300	
NGC 5044			CN_2, G4300, Mg_2	$H\beta$
A754#1	C4668	Mg_1		
A970#1		Mg_1, Fe5270	G4300	
A978#1		Mg_1	$H\delta_A$, G4300	

Table 6. Central values calculated within an aperture of $a_e/8$ and slit-width of $0.5''$.

Galaxy	age_o (Gyr)	$[Z/H]_o$ (dex)	$[E/Fe]_o$ (dex)
NGC 3557	11.2± 0.7	0.25± 0.01	0.21± 0.02
NGC 3640	7.5± 0.6	0.17± 0.02	0.18± 0.02
NGC 5044	15.0± 0.9	0.10± 0.02	0.40± 0.03
A754#1	15.0± 0.9	0.20± 0.01	0.24± 0.03
A970#1	15.0± 0.9	0.22± 0.02	0.27± 0.03
A978#1	11.2± 0.7	0.08± 0.04	0.18± 0.04
Mean	12.1±1.4	0.17±0.03	0.25±0.03

angles (i.e. a_e) for each galaxy. For those readers interested in the major axis gradients, the transformation is given in Equation 1. The gradients illustrated in these figures were fitted with linear relationships using a χ^2 minimization with errors in the Y-direction. To avoid the uncertainties and radial flattening due to seeing effects, the data within the central $1''$ were excluded from the fit.

We also note that there are intrinsic uncertainties in the models themselves that add a systematic error beyond that measured by our Monte Carlo analysis. These errors are not relevant when calculating gradients, or relationships within our sample, however they are relevant when comparing our results to those of other authors as in Section 5 below and in comparing our relationships with those of other studies in Section 7. In these sections we therefore add a factor of 0.1 dex in quadrature to our Monte Carlo errors as an indicator of the combined random plus systematic errors.

5 INDIVIDUAL GALAXIES

The kinematics and stellar populations are plotted in Figures 3, 4, 5, 7, 8 and 9. Here we discuss the results specific to each galaxy.

5.1 NGC 3557

NGC 3557 lies at the spatial centre of the NGC 3557 group (Brough et al. 2006). This is a dynamically mature group (e.g. Brough et al. 2006) with associated intra-group X-ray emission (Osmond & Ponman 2004).

The results of the stellar population analysis of this galaxy are illustrated in Figure 3. There is a small galaxy on one side of our slit which contaminates the spectrum from $r \geqslant +8.5''$. These data are illustrated in the top two panels of Figure 3 as open symbols, and are not included in the calculation of the gradients. The stellar populations of NGC 3557 were also studied by Annibali et al. (2006): Within an aperture of size $r_e/8$ and a slit-width of $2''$, they found NGC 3557 to have an age of 5.8 ± 0.8 Gyrs, [Z/H]$= 0.034 \pm 0.004$ dex and [E/Fe]$= 0.17 \pm 0.02$ dex. In contrast, within an aperture of $a_e/8$ and a slit-width of $0.5''$ we find an age of 11.2±3.5 Gyrs, [Z/H]$= 0.25 \pm 0.10$ dex and [E/Fe]$= 0.21 \pm 0.10$ dex; i.e. we find an older and more metal-rich centre to this galaxy but a consistent [E/Fe] ratio. These differences are not due to the age-metallicity degeneracy as this would result in us calculating an older age but a lower metallicity. Annibali et al. (2006) apply an emission correction to their $H\beta$ index and only use a few indices to measure their ages, metallicities and α-element enhancement ratios. Given these differences, the possibility for slit mis-alignment between the two studies, and the evidence that our method is robust to the effects of emission (Proctor et al. 2005), thus avoiding the need to apply uncertain emission corrections, we are convinced that our method is the more robust. Below, we show that when other data are reanalysed using the same techniques and models used here, the differences between the results obtained are less significant.

NGC 3557 galaxy shows extreme rotation (Figure 3). The degree by which a galaxy is rotationally supported, in terms of that expected for a rotationally flattened, oblate spheroid is quantified by the ratio $(v/\sigma)^* = (V_{max}/\langle\sigma\rangle)/[\epsilon/(\epsilon - \epsilon)]^{1/2}$ (Davies et al. 1983). This is normally $\ll 1$ for elliptical galaxies brighter than $M_B > -20$ mag (i.e. $M_K > -24$ mag), suggesting that these bright galaxies are supported by velocity anisotropy. NGC 3557 has $M_K \sim -20.5$ mag and $(v/\sigma)^* \sim 1$ (Fried & Illingworth 1994), making it a rotationally flattened, oblate spheroid. Numerical simulations suggest that rotationally supported galaxies are formed by different formation mechanisms to galaxies that are supported by velocity anisotropy: Isotropic oblate rotators form either from major (1:1) dissipational mergers (Cox et al. 2006) or minor (3:1) dissipationless mergers (Naab et al. 2006), whilst anisotropic galaxies are formed by major dissipationless mergers (Cox et al. 2006; Naab et al. 2006). However, NGC 3557 has a relatively steep metallicity gradient and an older central age, consistent with forming by collapse at high redshift while the kinematics may be a result of a dissipationless or dissipative collapse.

5.2 NGC 3640

NGC 3640 is the brightest galaxy in the NGC 3640 group. This group appears to be dynamically young as no X-ray

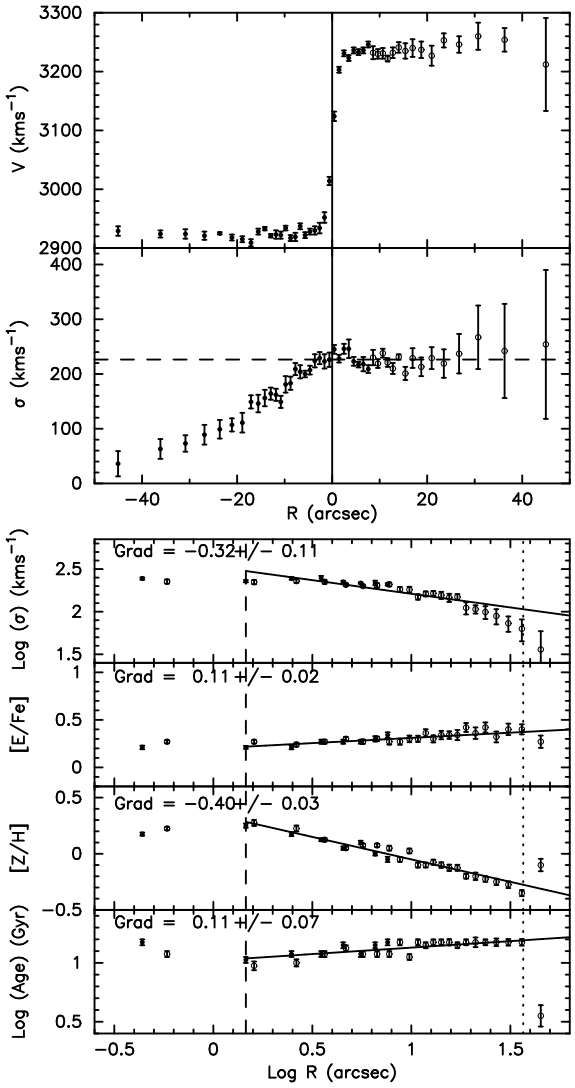

Figure 3. The radial profiles for NGC 3557 measured along the major axis of 31° (Table 2). The top two panels show the recession velocity and velocity dispersion profiles with linear radius. The open points in the top two panels indicate those contaminated by another galaxy in the slit (see text) – these points are not used in the gradient calculation. The errors indicate 1σ errors. The horizontal dashed line in the velocity dispersion panel indicates the corrected literature value given in Table 3. The lower 4 panels show measured quantities with logarithmic radius. Here the vertical dashed line indicates the seeing radius, the dotted line indicates the effective radius at the observed position angle (Table 2) and the solid line the linear fit to the data (whether it is significant or not) with the gradient and 1σ error on the gradient given in the top left-hand corner of each panel. The open points in the lower 4 panels indicate the right-hand side of the galaxy and the closed points the left-hand side. The error bars are the 1σ errors from the Monte Carlo analysis described in the text.

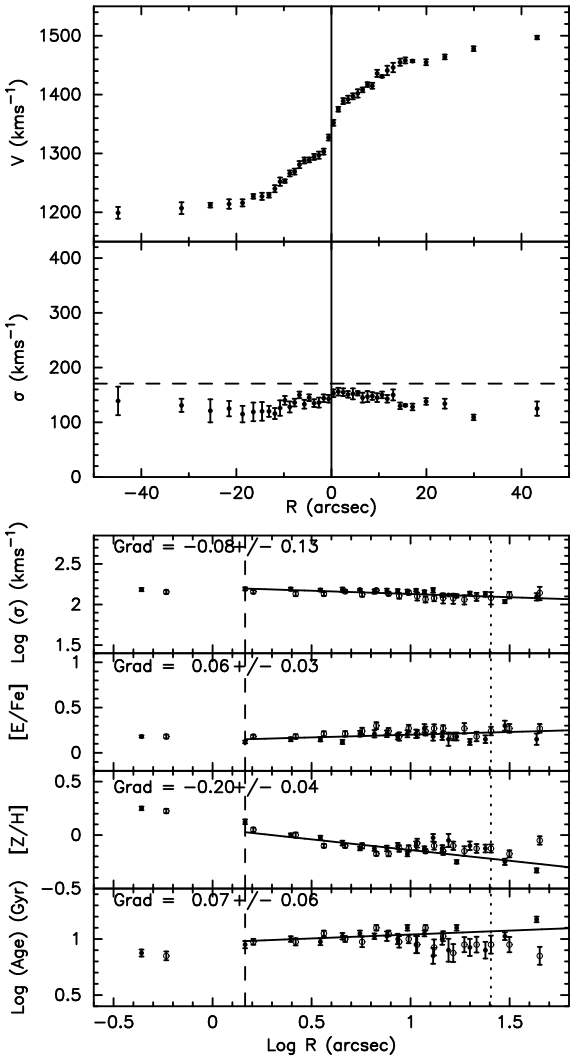

Figure 4. The radial profiles for NGC 3640, measured along the observed axis, PA = 31° (major axis = 95°; Table 2). The caption is as for Figure 3.

emission was detected above 3σ of the background level by *ROSAT* (Osmond & Ponman 2004).

We found emission in the central arcsecond of this galaxy (consistent with Goudfrooij et al. 1994), so the Hβ and Fe5015 indices which are heavily affected by emission were excluded from the analysis of the central two apertures. The results are illustrated in Figure 4.

Denicoló et al. (2005) studied this galaxy and found an age (within an $r_e/8$ aperture and 1.5″ slit-width) of $2.5^{+0.7}_{-0.3}$ Gyrs, [Z/H]= 0.53 ± 0.13 dex and [E/Fe]= 0.12 dex. In contrast, within an aperture of $a_e/8$ and a slit-width of 0.5″ our central age = 7.5 ± 1.8 Gyrs, [Z/H] = 0.17 ± 0.10 dex and [E/Fe] = 0.18 ± 0.10 dex. We find an older and less metal-rich centre to this galaxy but a consistent [E/Fe] ratio, despite using similar models to Denicoló et al. (2005) (who use the Thomas et al. 2003 models with Tripicco & Bell 1995 α-element enhancements). Denicoló et al. (2005) apply an emission correction to their Hβ indices and only use a few indices to measure ages, metallicities and α-element enhancement ratios. They find their galaxies to be systematically younger and more metal-rich when comparing to results obtained by Terlevich & Forbes (2002), even when using the same models. The Denicoló et al. (2005) data have been reanalysed using the same models and techniques as used here, finding an age of 4 Gyr, [Z/H]= 0.35 dex and [E/Fe]= 0.06 dex, within 1.5σ of our results. We therefore conclude that, given the different apertures involved, the un-

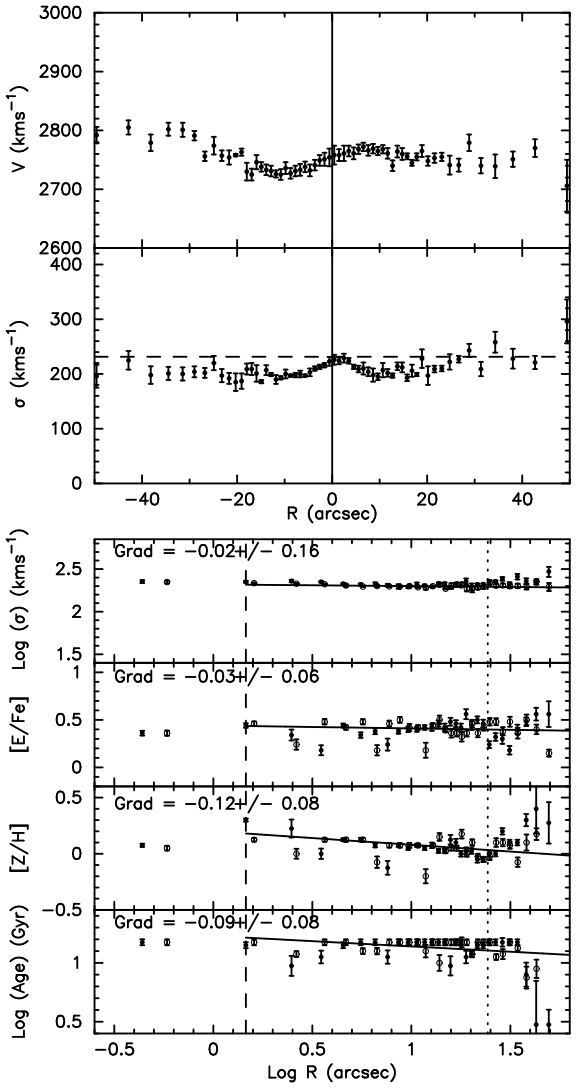

Figure 5. The radial profiles for NGC 5044 measured along the major axis of 20° (Table 2). The caption is as for Figure 3.

certainty of emission corrections and the possibility for slit mis-alignment between these studies, our results are robust.

The recession velocity profile of NGC 3640 shows indications of a possible disk in the central $r \sim 5''$ and of rotation: Bender et al. (1992) found $(v/\sigma)^* = 0.8$ for this galaxy. This is not unusual given that $M_K \sim -24$ mag. NGC 3640 also has a shallow metallicity gradient and a younger central age than other galaxies in the sample. These results are consistent with NGC 3640 having undergone a dissipational merger up to 7.5 Gyrs ago.

5.3 NGC 5044

NGC 5044 lies at the spatial and kinematic centre of the NGC 5044 group. This is a large, dynamically-evolved group (e.g. Brough et al. 2006) with associated intra-group X-ray emission (Osmond & Ponman 2004). X-ray observations with the *XMM* and *Chandra* satellites by Buote et al. (2003) and Tamura et al. (2003), respectively, have shown that the hot gas in the NGC 5044 group is dominated by a cooler component of $T_X \sim 0.7$ keV within a radius of 10 kpc ($r \leqslant 63''$) and by a warmer component of $T_X \sim 1.4$ keV beyond a radius of 40 kpc. The cooler component is similar to the kinetic temperature of the stars in the central galaxy suggesting the presence of stellar ejecta from NGC 5044 itself, while the hot phase is more characteristic of the halo of the group.

NGC 5044 is particularly interesting as, despite appearing in the optical as a very ordinary elliptical, it has been found to have very bright ionized gas emission, extending to radii of $40''$ in large filaments (Goudfrooij et al. 1994; Macchetto et al. 1996). Caon et al. (2000) compared the kinematics of the gas emission to that of the stellar component, finding the gas velocity profile to be very irregular at the 3 position angles (PA) that they studied and that the gas is systematically blue-shifted with respect to the stellar velocity profile by $\sim 60 - 100$ kms^{-1}, i.e. the gas is not in dynamical equilibrium. They concluded that the gas has recently been accreted from outside of the galaxy.

Following Caon et al. (2000), we examined the gas emission by fitting a Gaussian profile to the [NII]λ6583.6 line using the IRAF task *splot*. This line is the strongest and most prominent throughout the galaxy. We also examined the Hα and [OIII] lines - finding them to have similar equivalent width and recession velocity profiles as [NII]λ6583.6.

Figure 6 shows the equivalent width of the [NII]λ6583.6 line and the gas kinematics we derived, with respect to those from Caon's PA = 10° spectra. We observe significant emission across all radii we study, including highly broadened Hα emission in the central two apertures (Figure 1). We also observe the same central blue-shifting of the emission as Caon et al. (2000), despite the different position angle observed. The blue-shifted gas emission with respect to the stellar suggests that there is an outflow of material over these radii. This could be from a jet linked to the low-luminosity (flux at 1.4 GHz = 0.0347 Jy) compact ($r \sim 1''$) nuclear radio source observed by Condon et al. (1998) and the X-ray observations of Buote et al. (2003). The offset in emission velocities between this study and that of Caon et al. (2000) outside the central $5''$ is easily understood as a result of the different position angles observed and the filamentary nature of the observed Hα emission.

In order to determine whether the emission from NGC 5044 is due to star formation or an AGN we examine the radial distribution of the [NII]/$H\alpha$ ratio (Figure 6) and find it to be $\geqslant 1.5$ over most of the galaxy, peaking at 3-6 in the central $r < 5''$. Examining the diagnostic diagrams of Kewley et al. (2006) it is clear that all galaxies with [NII]/$H\alpha > 1$ are AGN. Our findings are consistent with Rickes et al. (2004) who concluded that in the central $r < 1$ kpc the ionization source must be an AGN.

The presence of a low-luminosity nuclear radio source and low-temperature central X-ray component, in addition to the broadened Hα emission, blue-shifted gas emission and high [NII]/$H\alpha$ ratio we observe here lead us to believe that NGC 5044 contains a low-luminosity AGN at its centre, with a jet pointing towards us.

Due to the presence of emission throughout this galaxy, and the resulting exclusion of the Balmer lines, this was one of the more difficult galaxies to fit, resulting in a noisy profile (Figure 5). We do, however, note good agreement with Rickes et al. (2004) and Annibali et al. (2006) for the old

central age of this galaxy: Rickes et al. (2004) fit 3 old components (age = 10 Gyrs) with different metallicities to the spectrum of NGC 5044 and compare that fit to one with solar metallicity and 3 different age components, finding that the spectra are better fitted by a range in metallicity than a range in age. Annibali et al. (2006) use a similar comparison of Lick indices to SSP models as we do here and, within an aperture of $r_e/8$ and a $2''$ slit-width, they find NGC 5044 to have an age of 14.2 ± 10 Gyrs, consistent with our central age of $= 15.0 \pm 3.9$ Gyrs (this is the maximum age modelled). Their α-element enhancement ratios and metallicities are also consistent with ours: $[\mathrm{E/Fe}]_{A06} = 0.34 \pm 0.17$ dex; $[\mathrm{E/Fe}]_{us} = 0.40 \pm 0.10$ dex and $[\mathrm{Z/H}]_{A06} = 0.015 \pm 0.022$ dex; $[\mathrm{Z/H}]_{us} = 0.10 \pm 0.10$ dex.

Caon et al. (2000) observe counter rotation of the central regions of NGC 5044 with respect to the outer regions: The inner $r \leqslant 15''$ is counter-rotating in their PA$= 10^\circ$ spectra. This is consistent with the $r \sim 10''$ region counter-rotating in our spectra (PA$= 20^\circ$). They also see signs of a further nuclear counter-rotating component within this region of radius $\sim 2''$. We do not observe this nuclear counter-rotating component. However, we do note that the errors in our recession velocity and velocity dispersion measurements increase significantly within this region, suggesting that we do not have the velocity resolution to resolve this structure.

Despite the counter-rotating centre and gas emission, we found no correlation of age, metallicity or α-element enhancement with these features. The lack of a visible population of young stars, despite significant emission, is further evidence for this being an AGN and not a starburst galaxy. NGC 5044 also has a very shallow metallicity gradient, suggesting it has undergone at least one, likely to be dissipative, merger event.

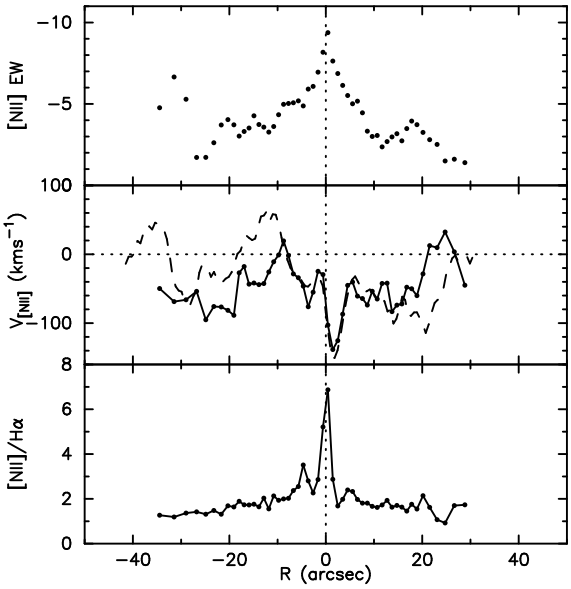

Figure 6. Distribution of gas emission in NGC 5044 along the major axis (PA $= 20^\circ$). The upper panel indicates the distribution of the equivalent width of the [NII]λ6583.6 emission velocity with radius. The middle panel indicates the velocity of the [NII] gas emission, relative to the stellar kinematics. The solid line indicates our data, while the dashed line gives the information from Caon et al. (2000), measured along an axis of PA $= 10^\circ$. The lower panel indicates the ratio of [NII] to Hα emission.

5.4 A754#1

The Abell 754 cluster consists of two major condensations - the most massive to the North-West containing the BCG and another $16'$ to the South-East, consistent with there having been a recent collision of two smaller clusters (Zabludoff & Zaritsky 1995). It also contains a weak cooling flow (White et al. 1997).

No previous age or metallicity measurements have been made of this galaxy or the other two BCGs of this sample.

We find this galaxy to be uniformly old (Figure 7), with a steep metallicity gradient, suggesting that the BCG has not undergone any merger event since its formation at high redshift. This also suggests that the BCG has not been affected by the cluster-cluster merger observed in the distribution of the X-ray emitting gas and optically observed galaxies by Zabludoff & Zaritsky (1995).

5.5 A970#1

The Abell 970 cluster, together with Abell 978, is a member of the Sextans supercluster (Einasto et al. 1997) and was found to have a weak cooling flow by White et al. (1997). The cluster was studied in detail by Sodré et al. (2001) who found A970#1 to lie at the spatial and kinematic centre of the cluster. They also found evidence for a galaxy group having recently fallen into the cluster.

We find A970#1 to be uniformly old with a steep metallicity gradient (Figure 8). This suggests that, like A754#1, A970#1 has not undergone any merger event since its formation at high redshift. There are no signs of star formation, suggesting that the infall of the group into this cluster has had no effect on the BCG.

5.6 A978#1

A978#1 was found to have a recession velocity of $V_0 = 16263 \pm 44$ kms^{-1} by the ESO Nearby Abell Cluster Survey (Katgert et al. 1996). This places it at the kinematic centre of the Abell 978 cluster as defined by Struble & Rood (1999).

The Abell 978 cluster has been found to have a cooling flow (Sarazin 1986) but no cold molecular gas was observed to be associated with it (Salomé & Combes 2003), suggesting that the cooling flow is not cooling sufficiently to form stars.

A978#1 shows strong rotation (Figure 9), very unusual in such a massive galaxy ($M_K \sim -26.5$ mag). We also find it to have a slightly younger central age, consistent with the observed low central α-element enhancement ratio. We also note its shallow metallicity gradient. These results all suggest that this galaxy has undergone a merger event. If this merger event was dissipative it must have happened *leq*10 Gyrs ago, however if it was a disspationless merger it could have occurred more recently.

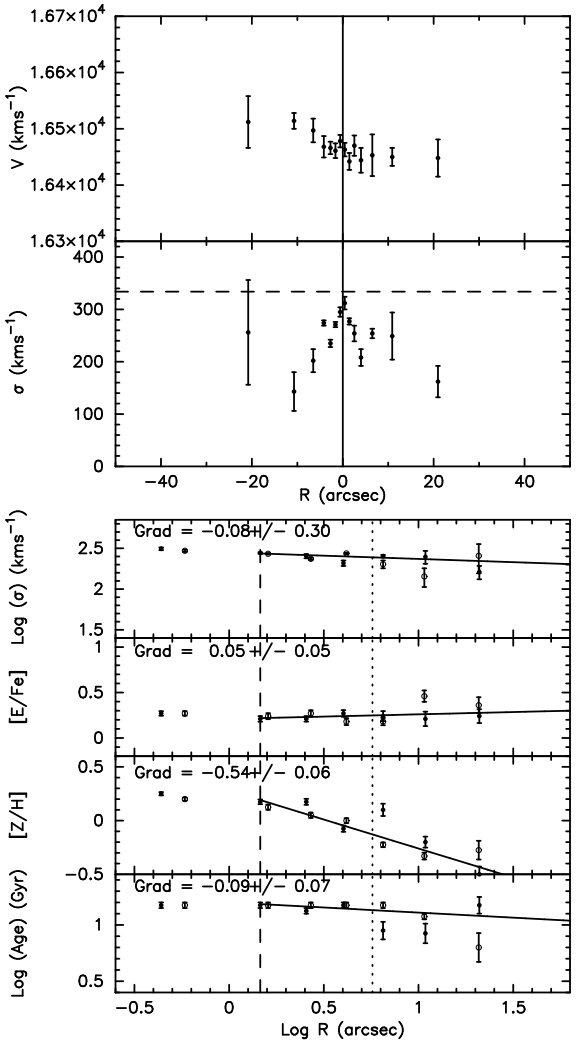

Figure 7. The radial profiles for A754#1, measured along a PA of 96° (major axis = 125°; Table 2). The caption is as for Figure 3.

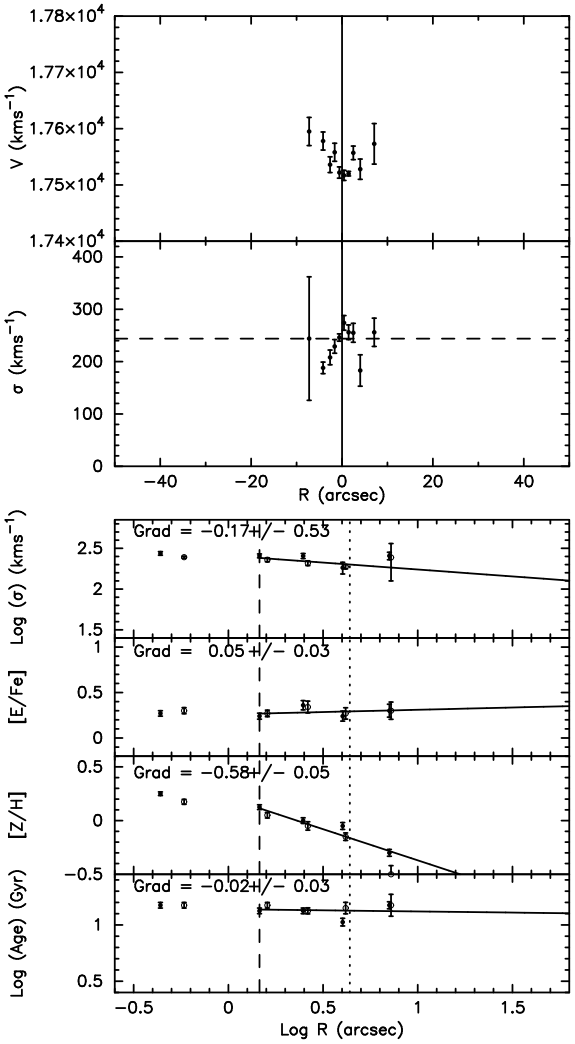

Figure 8. The radial profiles for A970#1, measured along a PA of 177° (major axis = 45°; Table 2). The caption is as for Figure 3.

Table 7. Linear fits to the relationships with environment. The significant relationships are illustrated in Figure 10.

Relationship (Y - X)	Gradient	Intercept	rms
Log(σ_0) - Log (L_X)	0.07± 0.03	-0.65± 0.08	0.08
M_K - Log (L_X)	-0.64± 0.17	2.32± 4.40	0.59
M_K - Log(σ_0)	-7.13± 0.07	-8.33± 1.98	0.80

6 RELATIONSHIP WITH ENVIRONMENT

Here we examine the dependence of BGG and BCG mass on the X-ray luminosity of their host group/cluster environment. X-ray luminosity is directly related to the density of the intra-group/cluster medium and therefore provides a quantitative measure of the density of the environment these galaxies reside in. In Figure 10 we compare the central velocity dispersions and absolute K-band magnitudes of the galaxies with the X-ray luminosity of their host environment. We fit linear relationships to these data using χ^2-minimization with errors in the Y-direction. We note that we only have an upper limit for the X-ray luminosity of the NGC 3640 group. It is possible to use the statistical tool of survival tasks to take upper (and lower) limits into account when fitting data (e.g. O'Sullivan et al. 2001; Brough et al. 2006). However, these tasks rely on there being values below the upper limit given and also assume that the upper limits are randomly distributed with respect to the independent parameter, neither of which are true here. We therefore fit to the X-ray luminosity of NGC 3640 as we do to the other X-ray luminosities, rather than as an upper limit.

The fits are given in Table 7. As a measure of whether or not these relationships are significantly different from the null hypothesis of no relationship, we take a relationship to be significant if the fitted gradient is at least a factor of 3 greater than the 1σ error on that gradient (i.e. $\geqslant 3\sigma_{gradient}$). In this and other plots in this paper, we only plot the significant relationships. We also examined the relationships with the dynamical mass of these galaxies, measured as $\propto \sigma_0^2 r_e$, and did not find these relationships to be more or less significant than the relationships with σ_0. We therefore only

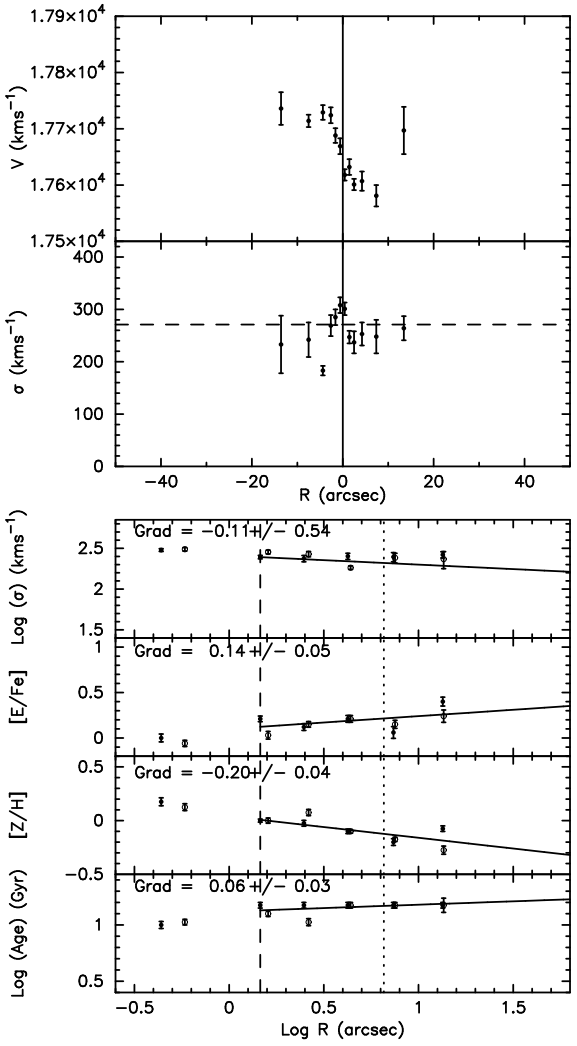

Figure 9. The radial profiles for A978#1, measured along a PA of 18° (major axis = 10°; Table 2). The caption is as for Figure 3.

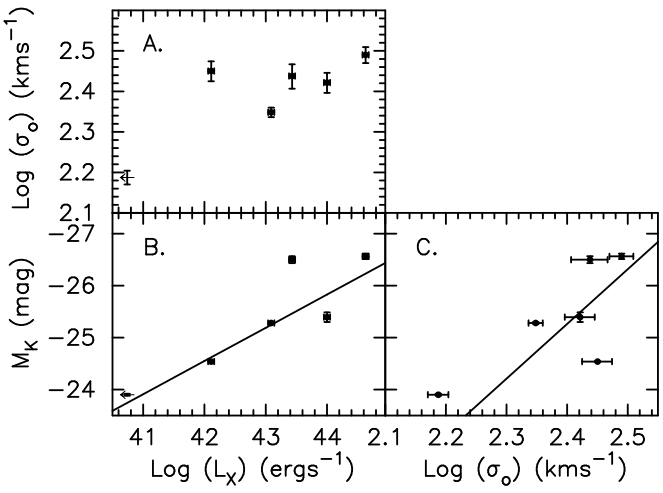

Figure 10. The relationship between the X-ray luminosity of the host system, L_X, and proxies for galaxy mass: central velocity dispersion (σ_0, panel A) and absolute K-band magnitude (M_K, panel B) and the relationship between the two mass proxies, i.e. the Faber-Jackson relation (panel C). The error bars indicate 1σ errors, the arrow indicates the upper limit in L_X measured for the NGC 3640 group. The solid lines indicate linear fits to our data that are statistically significant (all the fits are given in Table 7).

illustrate the relationships with σ_0 in this paper. The individual panels are discussed separately below:

A. Log (σ_0) − Log L_X: We see the suggestion of a trend between the central velocity dispersions of these galaxies and the X-ray luminosity of their host cluster: Galaxies in higher density clusters are more massive. The BCGs generally have higher velocity dispersions than the BGGs (Table 3). However, this relationship is not statistically significant (i.e. only $2\sigma_{gradient}$).

B. M_K − Log L_X: We observe that more X-ray luminous systems contain brightest group/cluster galaxies that are intrinsically brighter in the K-band than less X-ray luminous systems. This is consistent with studies of BCGs by Edge (1991) and Fisher et al. (1995a), and the results for BGGs found by Brough et al. (2006). However, it is in contrast to Brough et al. (2002) who found BCGs at redshifts < 0.1 in clusters with X-ray luminosities $L_X < 1.9 \times 10^{44}$ erg s^{-1} to exhibit a wide range of scatter in their absolute K-band magnitudes. The BCGs studied here are part of the Brough et al. (2002) sample, and therefore lie within the scatter they observed. However, the Brough et al. (2002) sample was significantly larger (92 BCGs with $z < 0.1$). In Brough et al. (2006) the correlation of the K-band luminosities of BGGs with the X-ray luminosity of their host group was driven by groups without extended group-scale X-ray emission detected (i.e. the X-ray luminosity of their host group was either solely that associated with the BGG itself or X-rays were not detected above $3\sigma_{background}$). We therefore conclude that the difference between this study and Brough et al. (2006), and that of Brough et al. (2002) is due to the smaller sample studied here and the inclusion of a BGG in a group without extended group-scale X-ray emission. We intend to investigate this issue in more detail with a significantly larger sample in a future paper.

C. Log (M_K − σ_0): Given that we are assuming that both central velocity dispersion and absolute K-band magnitude are good proxies for galaxy mass, we examine the relationship between them (the Faber-Jackson relation; Faber & Jackson 1976) here. BCGs have previously been found to lie off the Faber-Jackson relation for normal ellipticals at optical wavelengths, having brighter magnitudes than would be predicted by their velocity dispersions (e.g. Oegerle & Hoessel 1991; Bernardi et al. 2006b). Figure 10 illustrates that we find galaxies with larger velocity dispersions to be brighter, such that $M_K \propto \sigma^{-10.5\pm0.06}$.

Globally the only differences between BGGs and BCGs are the lower velocity dispersions and fainter absolute K-band magnitudes and, therefore, lower mass of the BGGs.

From the predictions of dLB we would expect BCGs to increase in mass in step with their host system. The trend of absolute magnitudes with cluster X-ray luminosity is, therefore, consistent with their predictions. However, it is surprising to note that galaxy velocity dispersion is only weakly related to cluster X-ray luminosity, as we would expect a much stronger correlation than this from the semi-analytic predictions.

Table 8. Linear fits to the relationships between the central values. The significant relationships from the upper section of this table are illustrated in Figure 11. The significant relationships from the lower section of this table are illustrated in Figure 12.

Relationship (Y-X)	Gradient	Intercept	rms
Log(age$_0$) - Log (L_X)	0.07± 0.01	-1.94± 0.04	0.06
[Z/H] - Log (L_X)	0.00± 0.00	0.16± 0.02	0.08
[E/Fe] - Log (L_X)	0.02± 0.01	-0.62± 0.01	0.09
Log(age)$_0$ - Log(σ_0)	0.78± 0.05	-0.78± 0.05	0.09
[Z/H]$_0$ - Log(σ_0)	0.13± 0.04	-0.14± 0.02	0.08
[E/Fe]$_0$ - Log(σ_0)	0.04± 0.05	0.15± 0.01	0.09
[Z/H]$_0$ - Log(age$_0$)	0.01± 0.04	0.16± 0.03	0.08
[E/Fe]$_0$ - Log(age$_0$)	0.45± 0.03	-0.24± 0.01	0.07

7 CENTRAL STELLAR POPULATIONS

Dissipative collapse scenarios predict that elliptical galaxies formed as a result of the collapse of gas clouds at $z \geqslant 3$ and have evolved quiescently since (e.g. Eggen et al. 1962; Larson 1974; Carlberg 1984; Arimoto & Yoshii 1987). In this scenario we expect to observe consistently old ages, with metallicities that scale with mass, high α-enhancement ratios and no dependence of these quantities on environment. In the hierarchical model of structure formation, elliptical galaxies are formed by mergers and accretion events over a Hubble time. If there is sufficient gas present in the progenitor galaxies then the mergers will induce star formation. dLB predict dissipationless mergers in the recent assembly of BCGs. Therefore, if their predictions are correct, we would expect to observe no correlation of metallicities with environment and no signs of star formation in the last ~ 5 Gyrs.

In the sections below we present the stellar population trends exhibited by our sample of galaxies. To compare with studies of the central values of ages and metallicities in normal early-type galaxies we use the measurements derived for the inner $a_e/8$ of our galaxies (i.e. an aperture $a_e/8 \times 0.5''$). These values are given in Tables 3 and 6. We note that three of our galaxies have hit the maximum age modelled of 15 Gyrs (Log (age)= 1.175 dex).

In Figure 11 we examine the relationships between the central stellar populations and their host environment. Linear relationships were fitted to the data and are given in the upper section of Table 8. The significant relationship is illustrated in Figure 11. Each panel is discussed individually below:

A. Log (L_X) − Log (age)$_0$: Semi-analytic models of hierarchical galaxy formation predict galaxies in the field have younger ages than those in clusters (Kauffmann & Charlot 1998): The dense central regions of the most massive clusters contain the oldest galaxies at any redshift.

We see that the galaxies in the 5 most X-ray luminous systems have very similar, old, ages, while the galaxy in the group without observed extended X-ray emission has the youngest central age. This is consistent with the results found for early-type galaxies in different environments by Rose et al. (1994); Trager et al. (2000); Kuntschner et al. (2002); Terlevich & Forbes (2002); Proctor et al. (2004a); Thomas et al. (2005); Bernardi et al. (2006a); Annibali et al. (2006); Smith et al. (2006).

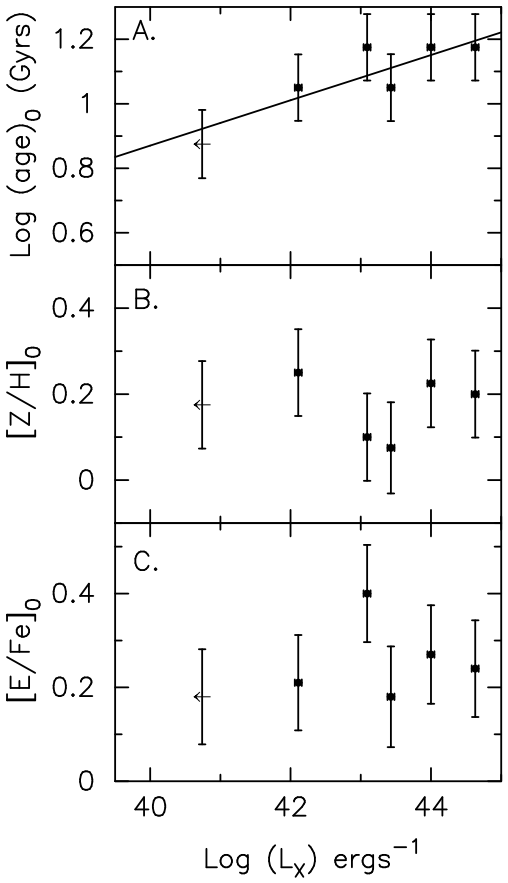

Figure 11. The relationship between the X-ray luminosity of the host system and central stellar population values. The error bars indicate 1σ errors in X-ray luminosity and the combined random and systematic errors in the central stellar populations. Linear fits to these relationships are given in Table 8, and the significant fit is illustrated.

B. Log (L_X) − [Z/H]$_0$: We observe no relationship between central metallicity and environment, consistent with observations of normal early-type galaxies by Bernardi et al. (2006a) and Smith et al. (2006), but in contrast to Rose et al. (1994); Proctor et al. (2004a); Thomas et al. (2005); Annibali et al. (2006).

C. Log (L_X) − [E/Fe]$_0$: We observe no relationship of central [E/Fe] with environment, consistent with studies of early-type galaxies by Thomas et al. (2005) and Annibali et al. (2006). Smith et al. (2006) find a significant trend with cluster-centric radius, after removing the relationship with galaxy mass. The result found here then suggests that, at the cluster centre, the [E/Fe] ratio does not depend on cluster density.

Figure 12 illustrates the relationships between the central stellar populations themselves. We also plot the significant relationships between our parameters (solid lines; Table 8). For comparison we have also illustrated the regions in which normal early-type galaxies lie in the relationships with velocity dispersion in high-density environments from Thomas et al. (2005; panels A, B, D). As Thomas et al. (2005) do not examine relationships with *age*, we also illus-

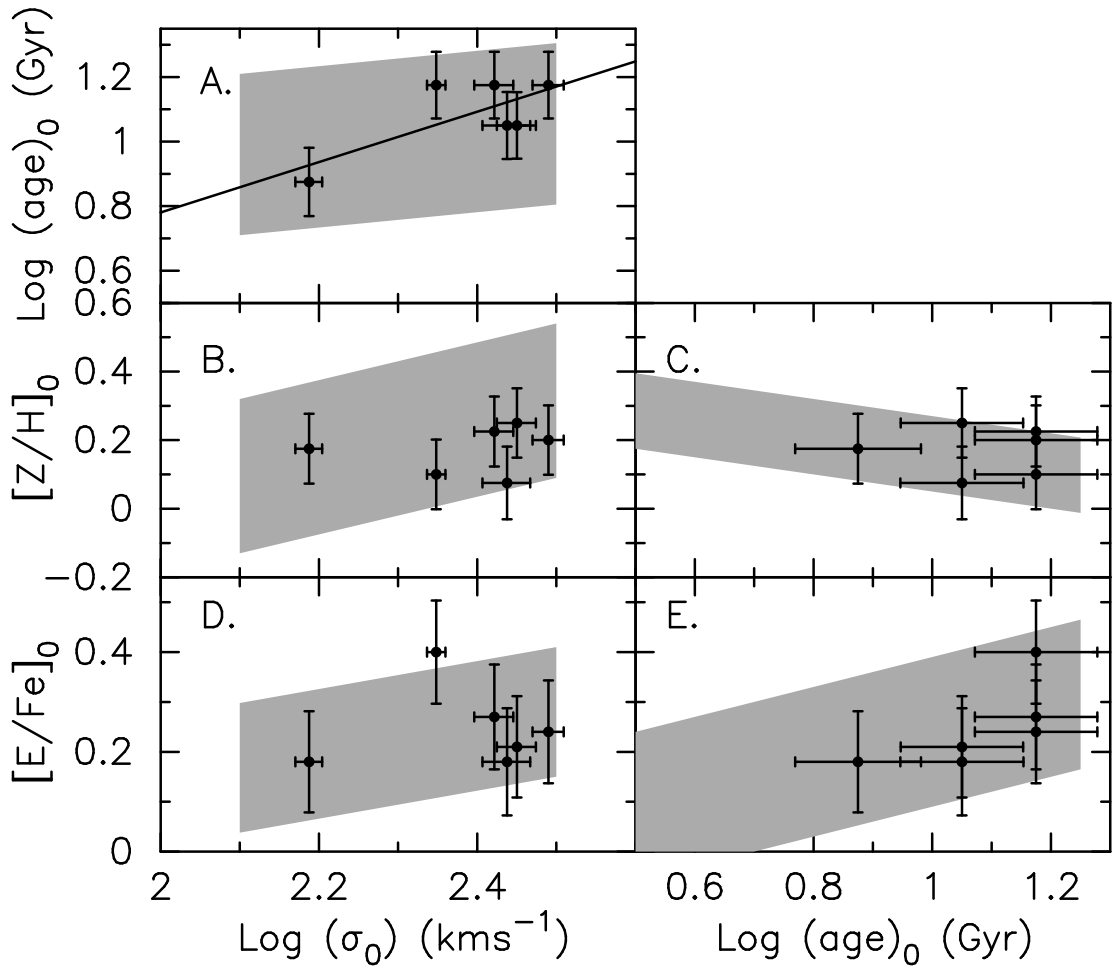

Figure 12. Relationships between central ages, metallicities ([Z/H]), α-element enhancements ([E/Fe]) and velocity dispersions (σ) measured in an aperture $a_e/8 \times 0.5''$. The error bars indicate 1σ errors in velocity dispersion and the combined random and systematic errors in the central stellar populations. The solid lines indicate straight-line fits to our data that are statistically significant (all the fits are given in Table 8). The shaded areas indicate the regions in which early-type galaxies lie in the relationships from Thomas et al. (2005; panels A, B, D) and Proctor et al. (2004a; panels C, E).

trate regions in which normal early-type galaxies lie in the relationships with age from Proctor et al. (2004a; panels C, E). Proctor et al. (2004a) studied galaxies in the field and loose groups, i.e. low-density environments. The individual panels are discussed below:

A. Log σ_0 – Log (age)$_0$: We observe that the 5 most massive galaxies have very similar masses and central ages, whilst the least massive galaxy, NGC 3640, has a much lower central age. As this is a luminosity-weighted central age, this means that the central stars of NGC 3640 are either, all 7.5 Gyrs old, or there is a small fraction of stars younger than 7.5 Gyrs superimposed on an older stellar population. Our sample is consistent with the ages measured for early-type galaxies in high-density environments by Thomas et al. (2005). The trend of older ages in more massive galaxies is consistent with studies of early-type galaxies by Trager et al. (2000); Proctor & Sansom (2002); Proctor et al. (2004a); Thomas et al. (2005); Denicoló et al. (2005); Nelan et al. (2005); Annibali et al. (2006); McDermid et al. (2006).

B. Log(σ_0) – [Z/H]$_0$: This is the classic mass-metallicity relationship. In contrast to the studies of early-type galaxies by Mehlert et al. (2003); Proctor et al. (2004a); Denicoló et al. (2005); Nelan et al. (2005); Thomas et al. (2005); Annibali et al. (2006); McDermid et al. (2006) we observe no relationship of mass with metallicity for the galaxies in this sample. However, we do note that our galaxies are consistent with the relationship followed by normal early-type galaxies in high-density environments from Thomas et al. (2005). Therefore, the lack of a strong trend is likely due to the small size of our sample and the small range in central velocity dispersion probed.

C. Log (age)$_0$ – [Z/H]$_0$: We do not observe a relationship between metallicity and age. However, we do note that our galaxies are consistent with the early-type galaxies studied by Proctor et al. (2004a). Trager et al. (2000); Kuntschner et al. (2002); Mehlert et al. (2003); Denicoló et al. (2005); Thomas et al. (2005); Sánchez-Blázquez et al. (2006a) also observe a correlation between these parameters for early-types. Therefore, the lack of a trend is likely to be a result of the small size of our sample.

D. Log (σ_0) − [E/Fe]$_0$: We observe no trend of [E/Fe] with mass. A positive relationship of [E/Fe] with velocity dispersion is observed for early-types by Trager et al. (2000); Terlevich & Forbes (2002); Proctor & Sansom (2002); Mehlert et al. (2003); Thomas et al. (2005); Denicoló et al. (2005); Nelan et al. (2005); Annibali et al. (2006); McDermid et al. (2006); Sánchez-Blázquez et al. (2006c).

E. Log (age)$_0$ − [E/Fe]$_0$: We observe no relationship between age and α-element enhancement ratio. However, our sample is consistent with the values found for normal early-type galaxies by Proctor et al. (2004a). A relationship of age with [E/Fe] ratio is also observed by Proctor & Sansom (2002); Mehlert et al. (2003); Proctor et al. (2004a); Denicoló et al. (2005); Thomas et al. (2005); Sánchez-Blázquez et al. (2006c). In contrast, Trager et al. (2000) found [E/Fe] to depend on σ, not age for their sample of early-types.

7.1 Summary

Our sample of BGGs and BCGs are very uniform in their velocity dispersions (masses) and stellar populations. We find one galaxy to be $\leqslant 8$ Gyrs old, while the remaining galaxies have a small range of central ages of 11-15 Gyrs.

We find that the age of these galaxies correlates with the X-ray luminosity (i.e. hot gas density) of their host cluster environment. We also find that the more massive galaxies are older than the least massive galaxy.

Comparing our results to those obtained for other early-type galaxies, we find that the stellar populations of these galaxies are consistent with those of normal early-type galaxies. This result is substantiated by von der Linden et al. (2006) who recently studied BCGs in the Sloan Digital Sky Survey. They found that, at the same stellar mass, the stellar populations of non-BCGs and BCGs are very similar, with the exception of their α-element enhancement ratios. They found these to be ~ 0.15 dex higher in BCGs (at our mean velocity dispersion). This difference is not visible in our sample, however, their sample is $\sim 100\times$ larger.

These results suggest that BGGs and BCGs have a similar stellar content and possibly star formation history to other early-type galaxies.

The lack of a relationship between the central metallicities and α-element enhancement ratios of these galaxies and their host environment and the uniformity of the metallicities and α-element enhancement ratios is consistent with both a dissipative collapse and the hierarchical merging predictions of dLB. The range of ages observed, and their relationship with the host cluster environment, is only consistent with the predictions of dLB. It is possible that we can discriminate between these models by studying the radial gradients in the stellar populations of these galaxies.

8 RADIAL GRADIENTS

In this section we examine whether the galaxies in our sample show evidence of radial gradients in their stellar populations and velocity dispersion and, if so, in what sense (positive or negative). Formation by dissipative collapse predicts strong negative metallicity gradients (i.e. metallicity decreases with increasing radius) that correlate with galaxy mass (Chiosi & Carraro 2002; Kawata & Gibson 2003), negative α-element enhancement gradients, and small positive to null age gradients. The predictions of dLB lead us to expect negative metallicity gradients that are shallower in more massive galaxies and in higher density environments.

The fitted gradients are given in Table 9 and the gradients themselves are illustrated in Figures 3, 4, 5, 7, 8 and 9. These are measured within the effective radius at the observed position angle, i.e. a_e, given in Table 2, and illustrated as the vertical dotted lines in Figures 3, 4, 5, 7, 8 and 9. We note that if we use the whole galaxy profile neither our gradients (within the errors) or our results are affected. Following our method for examining the relationships fitted to this sample; as a measure of whether or not these gradients are significantly different from the null hypothesis, we take a gradient to be significant if it is at least a factor of 3 greater than the 1σ error on that gradient (i.e. $\geqslant 3\sigma_{gradient}$).

8.1 Velocity Dispersion Gradients

Table 9 indicates that where a significant velocity dispersion gradient is observed, it is negative (i.e. velocity dispersion decreases with increasing radius) but that 5 galaxies in our sample (the exception being NGC 3557) have velocity dispersion gradients consistent with zero. Fisher et al. (1995a) also found that, with the exception of IC 1101 in the Abell 2029 cluster, the velocity dispersion gradients of their sample of 13 BCGs are negative. Examining velocity dispersion gradients to larger radii, Carter et al. (1999) found 1 out of their sample of 3 BCGs (NGC 6166 in the Abell 2199 cluster) to have a positive velocity dispersion gradient. Rising velocity dispersion profiles have been taken as evidence for the existence of high mass-to-light ratio components in these galaxies (Dressler 1979; Carter et al. 1981, 1985). These are clearly not present in this sample over the radii examined here.

8.2 Age Gradients

Our sample show small age gradients that are both positive and negative, but only 2 galaxies have significant age gradients (NGC 3557 and A970#1). This is consistent with the results of Mehlert et al. (2003) in their sample of early-type galaxies in the Coma cluster, Sánchez-Blázquez et al. (2006b) in their high-density environment early-type galaxy sample and also with the results of Sánchez-Blázquez et al. (2006c) for early-type galaxies in the field, groups and Virgo cluster environment. However, significant, positive, age gradients (i.e. young central ages and older outer regions) have been observed by, for example, Proctor et al. (2005) in the isolated elliptical galaxy NGC 821, and also by Sánchez-Blázquez et al. (2006b) in a larger sample of normal early-type galaxies in low-density environments. Positive age gradients suggest recent episodes of secondary star formation in the centres of galaxies. A lack of significant age gradients, together with the, generally, old central ages of BGGs/BCGs indicates that these galaxies have undergone few recent episodes of star formation.

Table 9. Velocity dispersion and stellar population gradients derived for the sample. Errors on the gradients (1σ) are also given.

Galaxy	ΔLog(σ) /ΔLog$r$ (dex/dex)	ΔLog (age) /ΔLog$r$ (dex/dex)	Δ[E/Fe] /ΔLog$r$ (dex/dex)	Δ[Z/H] /ΔLog$r$ (dex/dex)
NGC 3557	-0.31± 0.05	0.12± 0.02	0.12± 0.02	-0.40± 0.02
NGC 3640	-0.07± 0.02	0.07± 0.05	0.06± 0.03	-0.21± 0.04
NGC 5044	-0.04± 0.01	0.01± 0.04	0.00± 0.05	-0.17± 0.05
A754#1	-0.04± 0.03	-0.01± 0.01	0.02± 0.02	-0.41± 0.03
A970#1	-0.26± 0.02	-0.16± 0.03	0.08± 0.03	-0.47± 0.02
A978#1	-0.30± 0.04	0.06± 0.04	0.13± 0.04	-0.22± 0.03
Mean	-0.17±0.05	0.01±0.04	0.07±0.02	-0.31±0.05

Table 10. Linear fits to the relationships of the gradients, the significant relationships are illustrated in Figures 13 and 14.

Relationship (Y - X)	Gradient	Intercept	rms
Δ[Z/H]/ΔLog$r$ - Log(σ_0)	-0.72± 0.06	1.37± 0.02	0.12
Δ[Z/H]/ΔLog$r$ - M_K	-0.01± 0.07	-0.62± 0.06	0.16
Δ[Z/H]/ΔLog$r$ - [Z/H]$_0$	-1.42± 0.04	-0.09± 0.02	0.08
Δ[Z/H]/ΔLog$r$ - Log(age)$_0$	-0.66± 0.07	0.35± 0.03	0.15
Δ[Z/H]/ΔLog$r$ - Log (L_X)	-0.04± 0.01	1.34± 0.01	0.14

8.3 α-element enhancement gradients

Only 2 galaxies have significant α-element enhancement gradients (NGC 3557 and A978#1). This is consistent with Mehlert et al. (2003) who observe no significant α-element enhancement gradients in their sample of 35 early-type galaxies in Coma and with the study of the isolated elliptical galaxy NGC 821 by Proctor et al. (2005). In contrast, Sánchez-Blázquez et al. (2006c) find significant gradients that are both positive and negative in field, group and Virgo cluster early-type galaxies. Current models of the chemodynamical evolution of galaxies are currently unable to reproduce galaxies with flat [E/Fe] gradients (e.g. Matteucci & Francois 1989; Chiappini et al. 2001; Pipino & Matteucci 2004; Pipino et al. 2006).

8.4 Metallicity Gradients

We find that our sample covers a wide range of metallicity gradients. The self-consistent numerical GRAPE-SPH simulation of elliptical galaxy formation by Kobayashi (2004) found the mean metallicity gradients for galaxies produced by dissipative collapse (which includes minor dissipative mergers as the results are similar) and those produced through major mergers are: $\Delta[Z/H]/\Delta\log r \sim -0.30$ (collapse) and ~ -0.22 (major merger). Individually, the metallicity gradients suggest that three of the galaxies in our sample have dissipative collapse origins (i.e. NGC 3557, A754#1, A970#1 with $\Delta[Z/H]/\Delta\log r \leqslant -0.40$) whilst the other three have a merger origin (i.e. NGC 3640, NGC 5044, A978#1 with $\Delta[Z/H]/\Delta\log r \geqslant -0.22$). This range of gradients is surprising given the small dispersion observed in other BCG properties.

Any correlation of the gradients with mass is a further means by which to distinguish between the models of galaxy formation. In Figure 13 we show metallicity gradients as a function of proxies for galaxy mass, i.e. velocity dispersion, σ_0, and absolute K-band magnitude, M_K. We observe a tentative relationship between the metallicity gradient and the velocity dispersion: more massive galaxies have steeper gradients. However, we do not observe a relationship with M_K. Forbes et al. (2005) found a weak correlation with σ_0 *and* M_K in the same sense as we observe here for a sample of early-type galaxies. Sánchez-Blázquez et al. (2006c) observe a turnaround in this relationship at $\sigma_0 \sim 180$ kms^{-1} (Log(σ_0) = 2.2): Normal early-type galaxies with velocity dispersions less than this have gradients that steepen with increasing velocity dispersion, as expected from models of dissipative collapse and galaxies with velocity dispersions more than this value have shallower gradients, as expected for merger remnants. Examining a larger sample of early-type galaxies, Ogando et al. (2005) conclude that there is an increase in the scatter of this relationship above the same velocity dispersion, such that more massive galaxies show a wider range of metallicity gradients, and hence a wider range of evolutionary paths, than less massive galaxies. Our sample lies within the scatter of the data analysed by Ogando et al. (2005), suggesting that the opposite trend we observe is due to the small size of our sample.

In Figure 14 we show the relationships of the metallicity gradient with other galaxy properties, each panel is discussed individually below:

A. [Z/H]$_0$ − Δ[Z/H]/ΔLog$r$: We observe a relationship between the metallicity gradient and the central metallicity such that galaxies with steeper gradients are more centrally metal-rich. Mehlert et al. (2003) also found a weak hint of a correlation for early-type galaxies in the Coma cluster.

B. Log (age)$_0$ − Δ[Z/H]/ΔLog$r$: We find that galaxies with old central ages have a wide range of metallicity gradients. Previous research on normal early-type galaxies observed that galaxies with younger central ages have steeper metallicity gradients (e.g. Sánchez-Blázquez et al. 2006b,c; Kuntschner et al. 2006). However, our galaxies extend to older ages than these samples. The increased scatter at older ages illustrates the range of evolutionary histories these massive galaxies must have had.

C. Log (L_X) − Δ[Z/H]/ΔLog$r$: We observe a relationship such that galaxies in more massive clusters have steeper metallicity gradients, consistent with Sánchez-Blázquez et al. (2006b).

8.5 Summary

In contrast to the uniformity of the central stellar populations of our sample of BGGs and BCGs, we observe them to have a wide range of metallicity gradients. We find steeper gradients in galaxies with higher velocity dispersions, higher central metallicities and in galaxies with older central ages. The metallicity gradients are also steeper in galaxies in clusters with high X-ray luminosities.

We find no significant velocity dispersion, age or α-element enhancement ratio gradients in our BGGs or BCGs.

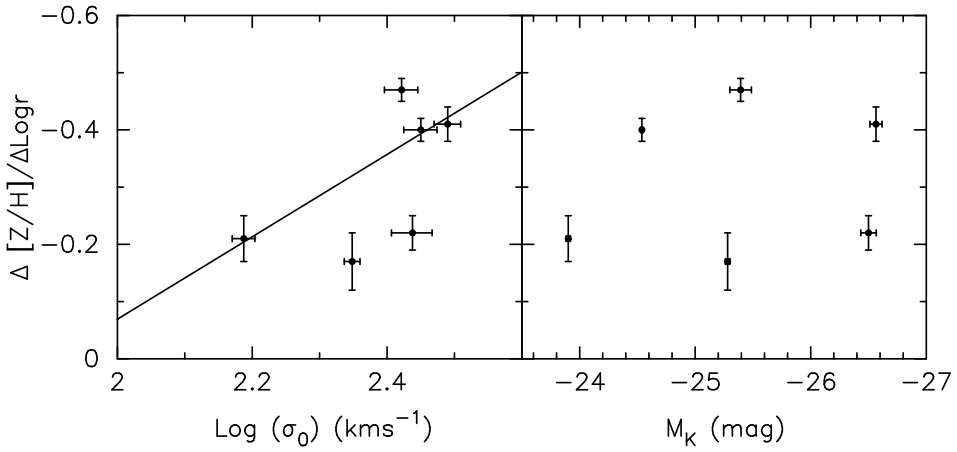

Figure 13. The relationship between metallicity gradient, and mass estimates: central velocity dispersion, σ_0, and K-band absolute magnitude, M_K. The error bars indicate 1σ errors. The solid lines indicate linear fits to our data that are statistically significant (all fits are given in Table 10).

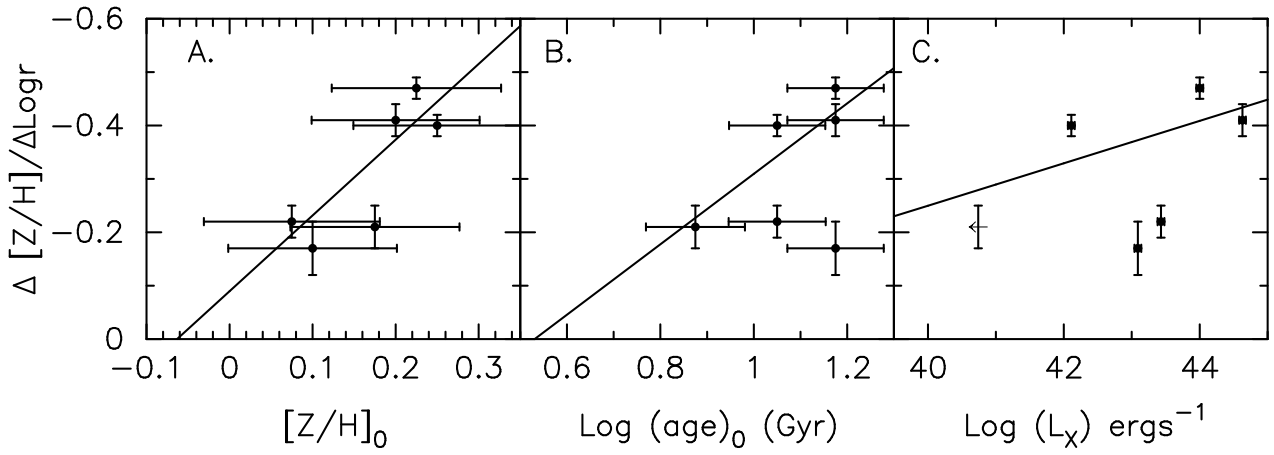

Figure 14. The relationship between metallicity gradient and A: central metallicity, B: central age, group/cluster X-ray luminosity. The error bars indicate 1σ errors. The solid lines indicate linear fits to our data that are statistically significant (all the fits are given in Table 10).

These results are consistent with studies of normal early-type galaxies in high-density environments. However, given the homogeneous environment that these galaxies sample, and the small dispersion of their luminosities, ages and masses, the range of metallicity gradients we observe is surprising. Even more surprising is the fact that the steepest gradients are found in the most massive galaxies and most X-ray luminous clusters.

We postulate two possible evolutionary scenarios that could produce the range of gradients we observe and the relationships that they follow:

If simulations of the formation of galaxies and the effects of mergers on their metallicity gradients are correct (e.g. Kobayashi 2004), then we expect galaxies that collapsed at $z > 2$ through the assembly of many, large, gas-rich galaxies, to display steep metallicity gradients, high central metallicities and old central ages today. These galaxies would also have shallow age and α-enhancement ratio gradients. However, if these galaxies undergo major mergers at $z < 2$ then the stellar populations observed today will depend on whether the merger induced star formation or not: If the merger did induce star formation then the merger would mix up the stellar populations, washing out the metallicity gradient, but the induced star formation would increase the central metallicity again. In this scenario we would observe shallower metallicity gradients, average central metallicities and the central ages would depend on when the last merger occurred. The galaxies might also have positive age and α-enhancement ratio gradients, depending on when the collapse occurred. In contrast, if there was no star formation induced in the merger, then the merger would wash out the metallicity gradient without adding a new population of stars. Therefore, we would observe shallower metallicity gradients, low central metallicities and old central ages today, even if the merger was a recent event. These galaxies would also show shallow age and α-enhancement ratio gradients. A combination of these various evolutionary histories are necessary to explain the relationships we observe with central metallicity (Figure 14 A) and age (Figure 14 B).

However, the models of metallicity gradients have not

been thoroughly tested on observations and it is also possible to explain these observations through a scenario in which galaxies assemble at high redshift with different efficiencies: In this scenario all the galaxies form at high redshift (> 10 Gyrs ago, $z > 2$) and, if the star formation efficiency remains the same, steep metallicity gradients are a result of galaxies assembling quickly from many gas-rich galaxies and passively evolving since, similar to the model above. Shallower gradients are then a result of the galaxies assembling more slowly (at $z \sim 2$) from a larger number of less gas-rich galaxies. This slower assembly allows the stellar populations to mix more efficiently, resulting in shallower gradients. As the assembly takes place relatively quickly at high redshifts this would also result in small age or α-element enhancement ratio gradients and uniform central stellar populations. NGC 3640 would still have had to undergo a relatively recent gaseous merger to explain its younger central age. This scenario is similar to the merger picture outlined above. The main difference is of timing – whether the galaxies assembled at $z \sim 2$ with little activity since, or over longer periods of time with either wet or dry major mergers occurring more recently.

It is also relevant to ask whether it is likely that some of the mergers occurred without any associated star formation? Figure 9 of dLB shows that, although the progenitors of BCGs since $z \sim 3$ are gas-poor, some still have non-zero gas fractions, consistent with observational evidence that most elliptical galaxies contain some cold gas (Morganti et al. 2006). Therefore, it seems unlikely that even these most massive galaxies would undergo 'star formation-less' mergers, despite their properties (e.g. structure, rotation; Fisher et al. 1995a; Brough et al. 2005; Bernardi et al. 2006b) being consistent with purely dissipationless models of galaxy formation (e.g. Boylan-Kolchin et al. 2006; Cox et al. 2006; Naab et al. 2006). These small gas fractions are likely to induce small amounts of star formation in the centres of galaxies that, although not apparent in photometry, would be visible in their spectra. We are clearly not observing such star formation.

The relationship of the metallicity gradients with cluster X-ray luminosity then suggests that the range of gradients amongst these galaxies is driven by their host cluster environment. This is either due to the lower probability of mergers since $z \sim 2$ in the high velocity dispersion cluster environment, or a higher efficiency of assembly in the same environments at $z > 2$.

It is not possible to determine between these two scenarios with only 6 galaxies. However, these observations are inconsistent with these galaxies forming simply through dissipative collapse *or* a series of dissipationless mergers with massive galaxies at recent times, like the predictions of semi-analytic models of hierarchical galaxy formation (e.g dLB). However, they do qualitatively agree with the results of purely N-body simulations of dark matter evolution in a Lambda Cold Dark Matter Universe, where the merger rates in massive cluster haloes are significantly higher than those in group-sized haloes at redshifts > 2, but the situation is reversed at redshifts < 1 (Gottlöber et al. 2001).

9 CONCLUSIONS

We have examined the kinematics and stellar populations of a sample of 3 BGGs and 3 BCGs in X-ray groups and clusters. We have found:

1. The central stellar population of BGGs and BCGs are remarkably similar to other early-type galaxies in high-density environments, being indistinguishable in terms of their central metallicities and α-element enhancement ratios.

2. On the other hand we find a wide range of metallicity gradients, suggesting that these galaxies have had very different assembly histories.

With a sample of only 6 galaxies, and the scatter observed in these trends for other early-type galaxies, a larger sample is necessary to confirm some of the trends we have observed. However, the similarity of the stellar populations of BCGs with those of normal early-type galaxies and the range of metallicity gradients we observe cannot simply be explained by cosmic variance. In particular, the range of metallicity gradients observed is more significant for our small sample size.

Our observations suggest that BCGs formed at redshifts $z > 2$ and that they must have followed a range of evolutionary histories, dependent on the density of their host cluster. Their evolutionary path could either be a result of the probability of mergers in the cluster environment since $z \sim 2$, or the efficiency of galaxy assembly in those environments at earlier times ($z > 2$).

A lower merger frequency with higher cluster X-ray luminosity is consistent with the findings from near-infrared photometry of BCGs by Brough et al. (2002) and Brough et al. (2005), that BCGs in high-mass clusters assembled their stellar mass at redshifts > 1, and have been passively evolving since, in contrast to BCGs in lower-mass clusters which appear to still be in the process of merging today. This is also consistent with that of N-body simulations (Gottlöber et al. 2001) where more mergers occur for galaxies in clusters than for galaxies in groups at $z > 2$, but that situation reverses at redshifts < 1.

A higher assembly efficiency is consistent with observations of large samples of early-type galaxies in various environments by, for example, Terlevich & Forbes (2002), Thomas et al. (2005) and Bernardi et al. (2006a). They showed that massive galaxies form earlier and faster than less massive galaxies. They suggest that galaxies in low-density environments form $\sim 1-2$ Gyrs after those in high-density environments, and that these galaxies are more likely to suffer star formation episodes since $z \sim 1$.

BCGs are a special case of the population of Luminous Red Galaxies (LRGs). The evolution of this population since redshifts $z \sim 1$ has been studied independently, and the results to date have been contradictory: Wake et al. (2006) did not find evidence for evolution beyond that expected from passive ageing since $z \sim 0.6$ in the luminosity function of their LRGs. They also find their luminosity functions to be consistent with those of Faber et al. (2005) at redshifts $z < 0.6$, despite the conclusion of Bell et al. (2004); Faber et al. (2005) and Yamada et al. (2005) that their samples of LRGs have increased in mass by up to a factor of 4 since $z \sim 1$. Brown et al. (2006) also found no evolution since $z \sim 1$ for their most massive ($> 4L^{\star}$) LRGs. Either

our merger or assembly alternatives for BCGs are consistent with these contradictory findings for the evolution of the whole LRG population. We also note that the Gemini Deep Deep Survey finds that the most massive galaxies have already assembled by $z \sim 1-2$ (Glazebrook et al. 2004).

Theoretically, our result that these most massive galaxies cannot all have formed through simple dissipative collapse, or through a series of dissipationless mergers with massive galaxies at recent times, is inconsistent with any single model of galaxy formation. These results clearly drive the need for more theoretical understanding of both the formation and evolution of stellar population gradients and of galaxy formation itself.

ACKNOWLEDGMENTS

We would like to thank George Hau and Harald Kuntschner for helpful comments. We would also like to thank the anonymous referee for their very constructive comments. SB, RP, DAF and WJC acknowledge the funding support of the Australian Research Council. DJB acknowledges the support of NASA contract NAS8-39073. This publication makes use of data products from the Two Micron All Sky Survey (2MASS) which is a joint project of the University of Massachusetts and the Infrared Processing and Analysis Center/California Institute of Technology, funded by the National Aeronautics and Space Administration and the National Science Foundation.

REFERENCES

Annibali F., Bressan A., Rampazzo R., Zeilinger W. W., Danese L., 2006, astro-ph/0609175
Arimoto N., Yoshii Y., 1987, A&A, 173, 23
Barnes J.E., 1991, IAUS, 146, 363
Bell E. F., et al., 2004, ApJ, 608, 752
Bekki K., Shioya Y., 1999, ApJ, 513, 108
Bender R., Burstein D., Faber S. M., 1992, ApJ, 399, 462
Bernardi M., Nichol R. C., Sheth R. K., Miller C J., Brinkmann J., 2006a, AJ, 131, 1288
Bernardi M., Hyde J. B., Sheth R. K., Miller C J., Nichol R. C., 2006b, astro-ph/0607117
Bernstein J. P., Bhavsar S. P., 2001, MNRAS, 322, 625
Boehringer H., et al., 2004, A&A, 425, 367
Boylan-Kolchin M., Ma C., Quataert E., 2006, MNRAS, 369, 1081
Brough S., Collins C. A., Burke D. J., Mann R. G., Lynam P. D., 2002, MNRAS, 329, 533
Brough S., Collins C. A., Burke D. J., Lynam P. D., Mann R. G., 2005, MNRAS, 364, 1354
Brough S., Forbes D. A., Kilborn V. A., Couch W., 2006, MNRAS, 370, 1223
Brown M. J. I., Dey A., Jannuzi B. T., Brand K., Benson A. J., Brodwin M., Croton D. J., Eisenhardt P. R., 2006, astro-ph/0609584
Bruzual A. G., Charlot S., 1993, ApJ, 405, 538
Buote D. A., Lewis A. D., Brighenti F., Mathews W. G., 2003, ApJ, 594, 741
Burke D. J., Collins C. A., Mann R. G., 2000, ApJL, 532, L105
Caon N., Macchetto D., Pastoriza M., 2000, ApJS, 127, 39
Carlberg R. G., 1984, ApJ, 286, 403
Carollo C. M., Danziger I. J., Buson L., 1993, MNRAS, 265, 553
Carter D., Efstathiou G., Ellis R. S., Inglis I., Godwin J., 1981, MNRAS, 195, 15
Carter D., Inglis I., Ellis R. S., Efstathiou G., Godwin J. G., 1985, MNRAS, 212, 471
Carter D., Bridges T. J., Hau G. K. T., 1999, MNRAS, 307, 131
Chiappini C., Matteucci F., Romano D., 2001, ApJ, 554, 1044
Chiosi C., Carraro G., 2002, MNRAS, 335, 335
Collins, C. A. & Mann, R. G. 1998, MNRAS, 297, 128
Condon J. J., Cotton W. D., Greisen E. W., Yin Q. F., Perley R. A., Taylor G. B., Broderick J. J., 1998, AJ, 115, 1693
Cox et al., astro-ph/0607446
Davidge T. J., Grinder M., 1995, AJ, 109, 1433
Davies R. L., Efstathiou G., Fall S. M., Illingworth G., Schechter P. L., 1983, ApJ, 266, 41
De Lucia G., Springel V., White S. D. M., Croton D., Kauffmann G., 2006, MNRAS, 366, 499
de Lucia G., Blaizot J., 2006, astro-ph/0606519, dLB
Denicoló G., Terlevich R., Terlevich E., Forbes D. A., Terlevich A., 2005, MNRAS, 358, 813
Dressler A., 1979, ApJ, 231, 659
Edge A. C., 1991, MNRAS, 250, 103
Eggen O. J., Lynden-Bell D., Sandage A. R., 1962, ApJ, 136, 748
Einasto M., Tago E., Jaaniste J., Einasto J., Andernach H., 1997, A&AS, 123, 119
Faber S. M., Jackson R. E., 1976, ApJ, 204, 668
Faber S. M., et al., 2005, astro-ph/0506044
Fisher D., Illingworth G., Franx M., 1995a, ApJ, 438, 539
Fisher D., Franx M., Illingworth G., 1995b, ApJ, 448, 119
Forbes D. A., Beasley M. A., Brodie J. P., Kissler-Patig M., 2001, ApJ, 563, 143
Forbes D. A., Sánchez-Blázquez P., Proctor R., 2005, MNRAS, 361, 6
Forbes D. A. et al. 2006, PASA, 23, 38
Franx M., Illingworth G., Heckman T., 1989, ApJ, 344, 613
Fried J. W., Illingworth G. D., 1994, AJ, 107, 992
Glazebrook K., et al., 2004, Nature, 430, 181
Gorgas J., Efstathiou G., Aragon-Salamanca A., 1990, MNRAS, 245, 217
Gottlöber S., Klypin A., Kravtsov A. V., 2001, ApJ, 546, 223
Goudfrooij P., Hansen L., Jorgensen H. E., Norgaard-Nielsen H. U., 1994, A&AS, 105, 341
Jarrett T. H., Chester T., Cutri R., Schneider S., Skrutskie M., Huchra J. P., 2000, AJ, 119, 2498
Jarrett T. H., Chester T., Cutri R., Schneider S. E., Huchra J. P., 2003, AJ, 125, 525
Jørgensen I., Franx M., Kjærgaard P., 1995, MNRAS, 276, 1341
Katgert P., Mazure A., den Hartog R., Adami C., Biviano A., Perea J., 1998, A&AS, 129, 399
Kauffmann G., Charlot S., 1998, MNRAS, 294, 705
Kawata D., Gibson, B. K., 2003, MNRAS, 340, 922
Kewley L. J., Groves B., Kauffmann G., Heckman T., astro-ph/0605681

Kobayashi C., 2004, MNRAS, 347, 740
Korn A. J., Maraston C., Thomas D., 2005, A&A, 438, 685
Kuntschner H., et al., 2006, MNRAS, 369, 497
Kuntschner H., Smith R. J., Colless M., Davies R. L., Kaldare R., Vazdekis A., 2002, MNRAS, 337, 172
Larson R. B., 1974, MNRAS, 169, 229
Macchetto F., Pastoriza M., Caon N., Sparks W. B., Giavalisco M., Bender R., Capaccioli M., 1996, A&AS, 120, 463
Martinelli A., Matteucci F., Colafrancesco S., 1998, MNRAS, 298, 42
Matteucci F., 1994, A&A, 288, 57
Matteucci F., Francois P., 1989, MNRAS, 239, 885
McDermid R. M., et al., 2006, astro-ph/0609452
Mehlert D., Thomas D., Saglia R. P., Bender R., Wegner G., 2003, A&A, 407, 423
Morganti R., et al., 2006, MNRAS, 371, 157
Naab T., Jesseit R., Burkert A., 2006, MNRAS, X, X
Nelan J. E. et al., 2005, ApJ, 632, 137
Norris M. A., Sharples R. M., Kuntschner H., 2006, MNRAS, 367, 815
Oegerle W. R., Hoessel J. G., 1991, ApJ, 375, 15
Ogando R. L. C., Maia M. A. G., Chiappini C., Pellegrini P. S., Schiavon R. P., da Costa L. N. 2005, ApJ, 632, 61
Osmond J. P. F., Ponman T. J., 2004, MNRAS, 350, 1511
O'Sullivan E., Forbes D. A., Ponman T. J., 2001, MNRAS, 328, 461
Pierce M., et al., 2006, MNRAS, 366, 1253
Pipino A., Matteucci F., 2004, MNRAS, 347, 968
Pipino A., Matteucci F., Chiappini C., 2006, ApJ, 638, 739
Proctor R. N., Sansom A. E., 2002, MNRAS, 333, 517
Proctor R. N., Forbes D. A., Hau G. K. T., Beasley M. A., De Silva G. M., Contreras R., Terlevich A. I., 2004a, MNRAS, 349, 1381
Proctor R. N., Forbes D. A., Beasley M. A., 2004b, MNRAS, 355, 1327
Proctor R. N., Forbes D. A., Forestell A., Gebhardt K., 2005, MNRAS, 362, 857
Proctor R. N. et al., 2007, in preparation
Rickes M. G., Pastoriza M. G., Bonatto Ch., 2004, A&A, 419, 449
Rose J. A., Bower R. G., Caldwell N., Ellis R. S., Sharples R. M., Teague P., 1994, AJ, 108, 2054
Salomé P., Combes F., 2003, A&A, 412, 657
Sánchez-Blázquez P., Gorgas J., Cardiel N., Gonzalez J. J., 2006a, astro-ph/0604568
Sánchez-Blázquez P., Gorgas J., Cardiel N., 2006b, astro-ph/0604571
Sánchez-Blázquez et al., 2006c, in preparation
Sarazin C. L., 1986, RvMP, 58, 1
Schlegel D. J., Finkbeiner D. P., Davis M., 1998, ApJ, 500, 525
Smith R. J. et al., 2004, AJ, 128, 1558
Smith R. J., Hudson M. J., Lucey J. R., Nelan J. E., Wegner G. A., 2006, MNRAS, 369, 1419
Sodré L. Jr., Proust D., Capelato H. V., Lima Neto G. B., Cuevas H., Quintana H., Fouqu P., 2001, A&A, 377, 428
Spolaor M., et al., 2006, in preparation
Springel V., et al., 2005, Nature, 435, 629
Struble M. F., Rood H. J., 1999, ApJS, 125, 35
Tamura T., Kaastra J. S., Makishima K., Takahashi I., 2003, A&A, 399, 497
Terlevich A. I., Forbes D. A., 2002, MNRAS, 330, 547
Thomas D., Kauffmann G., 1999, ASPC, 192, 261
Thomas D., Maraston C., Bender R., 2003, MNRAS, 339, 897
Thomas D., Maraston C., Korn A., 2004, MNRAS, 351, 19
Thomas D., Maraston C., Bender R., Mendes de Oliveira C., 2005, ApJ, 621, 673
Tonry J. L. et al., 2001, ApJ, 546, 681
Trager S. C., Worthey G., Faber S. M., Burstein D., Gonzalez J. J., 1998, ApJS, 116, 1
Trager S. C., Faber S. M., Worthey G., Gonzalez J. J., 2000, AJ, 120, 165
Tripicco M. J., Bell R. A., 1995, AJ, 110, 3035
van Albada T. S., 1982, MNRAS, 201, 939
von der Linden A., Best P. N., Kauffmann G., White S. D. M., astro-ph/0611196
Wake D.A., et al., 2006, MNRAS, 372, 537
White S. D. M., 1980, MNRAS, 191, 1
White D. A., Jones C., Forman W., 1997, MNRAS, 292, 419
Worthey G., Faber S. M., Gonzalez J. J., Burstein D., 1994, ApJS, 94, 687
Worthey G., Ottaviani D. L., 1997, ApJS, 111, 377
Yamada T., et al., 2005, ApJ, 634, 861
Yoshii Y., Takahara F., 1988, ApJ, 326, 1
Zabludoff A. I., Zaritsky D., 1995, ApJ, 447, 21
Zabludoff A. I., Mulchaey J. S., 1998, ApJ, 496, 39

APPENDIX A: CENTRAL APERTURE INDICES

Tables with indices measured in the central $a_e/8$ aperture and their errors per galaxy.

Table A1. Value of indices Hδ_A – Fe4531 and their errors (second line) for the central aperture of all galaxies.

Galaxy	Hδ_A Å	Hδ_F Å	CN$_1$ mag	CN$_2$ mag	Ca4227 Å	G4300 Å	Hγ_A Å	Hγ_F Å	Fe4383 Å	Ca4455 Å	Fe4531 Å
NGC 3557	-1.542	0.088	0.065	0.100	1.210	4.792	-6.534	-1.847	5.974	1.668	3.260
	0.232	0.166	0.013	0.004	0.064	0.087	0.159	0.069	0.213	0.167	0.104
NGC 3640	-0.884	0.254	0.026	0.058	1.125	4.837	-6.070	-1.498	5.425	1.509	2.985
	0.234	0.167	0.013	0.004	0.065	0.090	0.161	0.072	0.202	0.160	0.101
NGC 5044	-1.889	-0.363	0.093	0.126	1.168	5.203	-7.860	-3.092	5.293	1.395	2.931
	0.236	0.169	0.013	0.004	0.067	0.092	0.163	0.074	0.203	0.160	0.103
A754#1	-2.335	-0.070	0.108	0.148	1.233	5.493	-7.082	-2.224	5.743	1.685	3.429
	0.303	0.210	0.014	0.007	0.108	0.170	0.233	0.129	0.291	0.194	0.187
A970#1	-2.778	-0.315	0.124	0.171	1.412	5.684	-7.205	-2.365	5.595	1.609	3.269
	0.357	0.244	0.014	0.008	0.130	0.207	0.277	0.160	0.334	0.208	0.219
A978#1	-1.479	-0.342	0.044	0.086	1.171	5.409	-6.330	-1.731	5.188	1.950	3.132
	0.315	0.222	0.014	0.007	0.118	0.187	0.253	0.141	0.310	0.200	0.207

Table A2. Value of indices C4668 – Fe5782 and their errors (second line) for the central aperture of all galaxies.

Galaxy	C4668 Å	Hβ Å	Fe5015 Å	Mg$_1$ mag	Mg$_2$ mag	Mgb Å	Fe5270 Å	Fe5335 Å	Fe5406 Å	Fe5709 Å	Fe5782 Å
NGC 3557	7.332	1.485	6.255	0.134	0.302	4.706	2.857	2.628	1.904	0.774	1.028
	0.126	0.056	0.232	0.004	0.003	0.109	0.111	0.174	0.168	0.054	0.064
NGC 3640	6.468	1.899	5.783	0.107	0.260	4.153	2.745	2.420	1.596	0.984	0.870
	0.114	0.054	0.117	0.004	0.003	0.049	0.094	0.083	0.050	0.055	0.048
NGC 5044	6.353	-0.469	3.346	0.158	0.313	5.595	2.501	2.190	1.557	0.757	0.925
	0.118	0.056	0.165	0.004	0.003	0.054	0.095	0.087	0.056	0.055	0.049
A754#1	6.722	1.329	5.812	0.226	0.354	4.823	2.598	2.064	2.205	0.805	0.965
	0.250	0.105	0.259	0.004	0.004	0.122	0.141	0.157	0.254	0.085	0.082
A970#1	6.895	1.386	5.294	0.178	0.307	5.548	4.474	2.499	1.902	0.900	1.105
	0.302	0.123	0.287	0.004	0.004	0.133	0.158	0.177	0.141	0.097	0.093
A978#1	5.946	1.494	5.698	0.142	0.271	4.552	3.079	2.733	1.810	0.667	0.624
	0.286	0.120	0.303	0.004	0.004	0.137	0.159	0.205	0.171	0.101	0.097

APPENDIX B: RADIAL APERTURE INDICES

Tables with index values and their errors per aperture per galaxy.

Table B1. Value of indices Hδ_A – Fe4531 and their errors (second line) for apertures from $-45''$ – $+6''$ for NGC 3557.

Radius ($''$)	Hδ_A Å	Hδ_F Å	CN$_1$ mag	CN$_2$ mag	Ca4227 Å	G4300 Å	Hγ_A Å	Hγ_F Å	Fe4383 Å	Ca4455 Å	Fe4531 Å
-45.04	-4.822	1.469	0.257	0.303	-0.003	2.764	-2.556	-2.109	0.046	3.575	3.389
	0.469	0.275	0.016	0.013	0.211	0.320	0.347	0.225	0.482	0.251	0.312
-36.13	-4.314	0.300	0.233	0.267	-0.247	3.713	-3.662	-1.469	2.035	3.014	2.890
	0.493	0.306	0.017	0.014	0.223	0.325	0.369	0.230	0.484	0.259	0.327
-30.88	-3.339	1.089	0.176	0.203	-0.276	4.521	-5.070	-1.975	2.817	2.658	2.959
	0.511	0.311	0.017	0.014	0.232	0.342	0.401	0.251	0.509	0.270	0.342
-26.86	-4.237	0.250	0.188	0.206	0.557	3.850	-4.182	-1.519	3.009	2.374	2.857
	0.518	0.321	0.017	0.014	0.216	0.339	0.390	0.242	0.500	0.269	0.340
-23.65	-3.454	0.566	0.148	0.186	0.378	4.594	-4.619	-1.436	3.958	2.428	2.454
	0.521	0.326	0.017	0.014	0.221	0.344	0.403	0.249	0.501	0.272	0.349
-21.09	-4.255	-0.060	0.146	0.164	0.286	4.184	-5.114	-1.566	4.049	1.855	2.480
	0.523	0.333	0.017	0.014	0.218	0.345	0.405	0.248	0.496	0.275	0.346
-18.91	-2.942	0.515	0.105	0.126	0.743	4.074	-4.928	-1.580	4.153	1.884	2.644
	0.502	0.321	0.017	0.014	0.206	0.340	0.398	0.244	0.490	0.271	0.341
-17.08	-3.810	-0.467	0.099	0.115	0.739	4.411	-5.239	-1.518	3.761	1.726	2.521
	0.530	0.346	0.017	0.014	0.216	0.351	0.414	0.252	0.510	0.281	0.353
-15.55	-2.855	0.086	0.114	0.153	0.543	5.009	-5.370	-1.639	4.834	1.946	3.039
	0.510	0.335	0.017	0.014	0.213	0.334	0.404	0.247	0.485	0.272	0.339
-14.16	-2.365	-0.072	0.092	0.122	0.668	5.089	-5.525	-1.721	4.182	1.563	2.668
	0.499	0.333	0.017	0.014	0.208	0.330	0.403	0.245	0.489	0.274	0.339
-12.92	-2.382	-0.097	0.083	0.112	0.902	4.646	-5.942	-1.816	4.503	1.581	2.839
	0.497	0.330	0.017	0.014	0.202	0.332	0.401	0.243	0.485	0.272	0.336
-11.82	-1.831	0.290	0.059	0.092	0.935	4.640	-5.470	-1.718	4.253	1.520	2.356
	0.493	0.327	0.017	0.014	0.202	0.335	0.399	0.244	0.484	0.273	0.340
-10.80	-2.589	-0.455	0.064	0.082	1.023	4.538	-5.489	-1.406	4.852	1.656	3.112
	0.473	0.320	0.016	0.013	0.187	0.315	0.378	0.226	0.454	0.261	0.315
-9.78	-1.579	0.139	0.049	0.076	1.168	4.459	-5.836	-1.582	5.009	1.793	2.657
	0.444	0.300	0.016	0.012	0.175	0.295	0.358	0.212	0.428	0.249	0.296
-8.76	-2.344	-0.138	0.058	0.087	0.883	5.036	-6.107	-1.934	5.015	1.640	2.559
	0.427	0.287	0.016	0.011	0.168	0.273	0.341	0.204	0.405	0.239	0.278
-7.74	-2.000	0.192	0.049	0.088	0.863	4.531	-5.705	-1.548	5.053	1.694	2.828
	0.399	0.269	0.015	0.010	0.157	0.255	0.315	0.183	0.379	0.227	0.255
-6.72	-1.926	-0.020	0.047	0.076	1.096	4.960	-5.841	-1.682	4.950	1.589	2.899
	0.372	0.253	0.015	0.009	0.141	0.230	0.291	0.168	0.351	0.216	0.232
-5.69	-1.431	0.224	0.046	0.085	1.086	4.849	-6.173	-1.788	5.483	1.664	2.788
	0.345	0.237	0.014	0.009	0.128	0.209	0.270	0.153	0.323	0.206	0.211
-4.67	-1.932	-0.054	0.062	0.094	1.011	4.959	-6.102	-1.666	5.118	1.442	3.028
	0.325	0.224	0.014	0.008	0.117	0.189	0.249	0.138	0.301	0.198	0.191
-3.65	-1.519	-0.064	0.050	0.082	1.128	4.991	-6.499	-1.744	5.519	1.493	2.839
	0.302	0.210	0.014	0.007	0.105	0.170	0.230	0.124	0.278	0.190	0.173
-2.63	-1.633	-0.031	0.062	0.095	1.113	4.781	-6.341	-1.718	5.725	1.679	3.212
	0.282	0.198	0.014	0.007	0.094	0.152	0.211	0.109	0.257	0.181	0.153
-1.61	-1.415	0.119	0.065	0.099	1.151	4.778	-6.459	-1.761	5.756	1.665	3.185
	0.266	0.187	0.013	0.006	0.084	0.136	0.196	0.098	0.240	0.175	0.138
-0.58	-1.433	0.047	0.071	0.101	1.166	4.610	-6.500	-1.768	5.938	1.583	3.219
	0.259	0.183	0.013	0.006	0.081	0.130	0.190	0.093	0.233	0.173	0.133
0.44	-1.628	0.046	0.082	0.114	1.091	4.752	-6.922	-2.096	6.027	1.474	3.333
	0.260	0.183	0.013	0.006	0.081	0.130	0.191	0.093	0.233	0.174	0.134
1.46	-1.406	0.128	0.066	0.097	1.110	4.581	-6.478	-1.751	5.768	1.449	3.166
	0.260	0.183	0.013	0.006	0.081	0.132	0.192	0.094	0.235	0.174	0.134
2.48	-1.344	0.237	0.058	0.089	1.181	4.740	-6.492	-1.850	5.580	1.452	3.102
	0.269	0.189	0.014	0.006	0.087	0.142	0.202	0.102	0.247	0.179	0.146
3.50	-1.430	0.080	0.050	0.082	1.152	5.082	-6.406	-1.845	5.273	1.519	3.089
	0.286	0.200	0.014	0.007	0.098	0.157	0.218	0.115	0.267	0.186	0.162
4.53	-1.452	0.268	0.051	0.081	1.103	5.062	-6.753	-2.082	5.318	1.421	2.896
	0.307	0.212	0.014	0.007	0.108	0.176	0.239	0.130	0.287	0.193	0.181
5.55	-1.488	-0.084	0.043	0.076	1.022	4.943	-6.331	-1.750	5.107	1.365	2.849
	0.329	0.228	0.014	0.008	0.121	0.197	0.259	0.144	0.312	0.202	0.202

Table B2. Value of indices C4668 – Fe5782 and their errors (second line) for apertures from $-45''-+6''$ for NGC 3557.

Radius ($''$)	C4668 Å	Hβ Å	Fe5015 Å	Mg_1 mag	Mg_2 mag	Mgb Å	Fe5270 Å	Fe5335 Å	Fe5406 Å	Fe5709 Å	Fe5782 Å
-45.04	5.419	5.804	3.866	0.071	0.200	2.932	2.351	1.727	-0.677	-0.388	0.217
	0.462	0.154	0.364	0.006	0.005	0.172	0.199	0.220	0.171	0.148	0.124
-36.13	6.488	4.734	4.439	0.095	0.202	3.054	2.019	2.098	0.066	-0.314	0.217
	0.466	0.164	0.380	0.006	0.005	0.177	0.208	0.226	0.171	0.151	0.126
-30.88	6.512	3.997	4.917	0.091	0.227	3.359	2.091	2.028	0.361	0.209	0.345
	0.491	0.177	0.401	0.006	0.006	0.188	0.218	0.240	0.180	0.155	0.132
-26.86	6.257	3.740	5.469	0.097	0.228	3.030	2.195	2.097	0.397	0.401	0.521
	0.482	0.173	0.392	0.006	0.006	0.187	0.215	0.234	0.175	0.152	0.129
-23.65	5.810	3.353	5.068	0.099	0.236	3.620	0.828	1.720	0.649	0.477	0.659
	0.494	0.180	0.404	0.006	0.006	0.187	0.228	0.242	0.177	0.154	0.129
-21.09	6.280	3.014	5.144	0.101	0.240	3.592	1.314	1.717	0.755	0.533	0.576
	0.486	0.182	0.400	0.006	0.006	0.186	0.223	0.239	0.174	0.153	0.128
-18.91	5.759	2.739	4.440	0.099	0.247	3.678	1.341	1.802	0.714	0.381	0.566
	0.478	0.180	0.395	0.006	0.006	0.183	0.219	0.235	0.171	0.151	0.126
-17.08	5.809	2.523	5.446	0.104	0.252	3.729	1.405	1.890	0.957	0.569	0.552
	0.498	0.186	0.407	0.006	0.006	0.190	0.226	0.243	0.176	0.154	0.130
-15.55	5.518	2.185	4.875	0.113	0.252	4.013	2.138	1.661	1.102	0.788	0.498
	0.482	0.183	0.397	0.006	0.006	0.181	0.216	0.237	0.169	0.149	0.126
-14.16	6.386	2.067	5.152	0.109	0.261	3.921	2.330	2.088	0.874	0.698	0.734
	0.472	0.182	0.394	0.006	0.006	0.181	0.213	0.233	0.169	0.148	0.125
-12.92	6.531	2.175	5.320	0.113	0.263	3.982	2.239	1.796	1.131	0.720	0.687
	0.468	0.181	0.389	0.006	0.005	0.179	0.212	0.233	0.166	0.147	0.124
-11.82	5.953	2.103	5.095	0.117	0.261	3.828	2.368	2.082	1.008	0.581	0.837
	0.471	0.181	0.391	0.006	0.005	0.180	0.211	0.231	0.167	0.148	0.122
-10.80	5.437	1.767	5.564	0.120	0.257	3.832	2.163	1.891	1.040	0.728	0.686
	0.446	0.173	0.364	0.006	0.005	0.169	0.200	0.218	0.156	0.140	0.116
-9.78	5.911	2.119	5.232	0.113	0.270	4.109	2.567	2.075	1.392	0.722	0.778
	0.411	0.159	0.343	0.005	0.005	0.156	0.188	0.205	0.144	0.132	0.109
-8.76	6.233	1.802	4.929	0.118	0.275	3.968	2.449	2.347	1.291	0.759	0.631
	0.382	0.149	0.322	0.005	0.005	0.147	0.178	0.191	0.135	0.126	0.103
-7.74	6.025	1.568	5.456	0.121	0.275	4.158	2.493	2.374	1.476	0.743	0.750
	0.350	0.138	0.303	0.005	0.004	0.135	0.166	0.180	0.139	0.119	0.095
-6.72	6.392	1.792	5.502	0.123	0.282	4.329	2.365	2.113	1.588	0.796	0.765
	0.316	0.125	0.269	0.004	0.004	0.122	0.155	0.166	0.118	0.111	0.087
-5.69	6.607	1.710	5.465	0.126	0.279	4.206	2.645	2.139	1.446	0.929	0.815
	0.283	0.113	0.245	0.004	0.004	0.113	0.142	0.149	0.104	0.104	0.080
-4.67	6.375	1.588	5.830	0.125	0.288	4.360	2.564	2.168	1.387	0.823	0.926
	0.256	0.102	0.240	0.004	0.004	0.099	0.133	0.138	0.096	0.099	0.073
-3.65	6.778	1.712	5.949	0.128	0.293	4.432	2.591	2.218	1.457	0.803	0.935
	0.226	0.092	0.238	0.004	0.004	0.102	0.125	0.133	0.094	0.094	0.071
-2.63	7.194	1.696	6.017	0.130	0.297	4.390	2.743	2.421	1.607	0.802	1.002
	0.195	0.082	0.244	0.004	0.004	0.082	0.116	0.122	0.086	0.089	0.063
-1.61	7.571	1.666	6.273	0.131	0.305	4.528	2.813	2.473	1.645	0.789	0.987
	0.170	0.073	0.201	0.004	0.003	0.083	0.110	0.117	0.084	0.085	0.061
-0.58	8.147	1.496	5.960	0.138	0.313	4.676	2.864	2.524	1.645	0.764	1.030
	0.164	0.070	0.201	0.004	0.003	0.074	0.108	0.116	0.083	0.084	0.061
0.44	7.950	1.288	5.813	0.140	0.313	4.726	2.876	2.648	1.829	0.781	0.998
	0.178	0.069	0.168	0.004	0.003	0.120	0.127	0.109	0.076	0.083	0.071
1.46	7.814	1.663	5.857	0.131	0.303	4.523	2.811	2.568	1.750	0.751	0.929
	0.166	0.073	0.166	0.004	0.003	0.069	0.107	0.107	0.072	0.085	0.057
2.48	7.329	1.595	5.830	0.131	0.295	4.392	2.782	2.586	1.788	0.859	0.829
	0.195	0.078	0.188	0.004	0.004	0.117	0.131	0.120	0.085	0.088	0.070
3.50	6.898	1.637	5.613	0.127	0.292	4.512	2.718	2.437	1.819	0.824	0.889
	0.212	0.089	0.235	0.004	0.004	0.103	0.128	0.156	0.132	0.093	0.070
4.53	6.873	1.678	5.319	0.127	0.291	4.350	2.649	2.161	1.705	0.882	0.838
	0.240	0.098	0.264	0.005	0.004	0.097	0.130	0.137	0.096	0.098	0.073
5.55	6.594	1.762	5.292	0.124	0.286	4.399	2.536	2.310	1.668	0.780	0.799
	0.271	0.109	0.241	0.005	0.004	0.127	0.140	0.147	0.102	0.104	0.084

Table B3. Value of indices Hδ_A – Fe4531 and their errors (second line) for apertures from $+6'' - +45''$. The apertures from $+8 - +45''$ are contaminated by another galaxy in the slit.

Radius ($''$)	Hδ_A Å	Hδ_F Å	CN$_1$ mag	CN$_2$ mag	Ca4227 Å	G4300 Å	Hγ_A Å	Hγ_F Å	Fe4383 Å	Ca4455 Å	Fe4531 Å
6.57	-1.439	0.030	0.042	0.072	1.108	4.786	-6.180	-1.855	5.321	1.411	2.868
	0.354	0.244	0.015	0.009	0.133	0.219	0.280	0.161	0.337	0.212	0.223
7.59	-1.604	0.045	0.047	0.068	1.114	4.300	-5.690	-1.500	5.042	1.453	2.970
	0.378	0.259	0.015	0.010	0.144	0.242	0.300	0.173	0.362	0.222	0.242
8.61	-1.792	0.013	0.052	0.079	1.154	4.754	-5.950	-1.654	5.181	1.568	2.901
	0.403	0.275	0.015	0.011	0.155	0.261	0.325	0.190	0.389	0.233	0.264
9.64	-1.785	0.115	0.047	0.080	0.956	4.668	-5.655	-1.573	4.489	1.420	2.906
	0.428	0.290	0.016	0.012	0.171	0.282	0.346	0.206	0.421	0.246	0.286
10.66	-2.723	-0.037	0.062	0.089	1.355	4.875	-6.199	-1.814	4.635	1.347	3.261
	0.461	0.306	0.016	0.012	0.177	0.300	0.372	0.222	0.447	0.258	0.305
11.68	-1.624	0.237	0.041	0.066	0.815	4.902	-5.671	-1.621	4.735	1.432	2.831
	0.476	0.319	0.016	0.013	0.197	0.320	0.389	0.234	0.471	0.269	0.327
12.77	-1.715	0.280	0.066	0.098	0.757	4.527	-5.702	-1.699	4.637	1.661	2.641
	0.480	0.319	0.016	0.013	0.201	0.325	0.392	0.236	0.475	0.268	0.330
14.01	-2.221	-0.247	0.060	0.073	0.933	4.542	-5.887	-2.110	4.647	1.498	2.809
	0.488	0.330	0.017	0.014	0.201	0.331	0.399	0.245	0.483	0.273	0.334
15.40	-2.202	-0.115	0.069	0.093	0.741	4.382	-5.337	-1.763	4.366	1.605	2.772
	0.494	0.331	0.017	0.014	0.207	0.337	0.400	0.245	0.492	0.274	0.340
16.93	-2.556	0.151	0.108	0.118	1.123	4.072	-5.271	-1.758	4.008	1.264	2.903
	0.513	0.334	0.017	0.014	0.203	0.348	0.409	0.251	0.508	0.285	0.347
18.76	-3.214	0.024	0.109	0.117	0.943	4.711	-5.717	-1.761	4.320	1.485	2.843
	0.503	0.325	0.017	0.014	0.200	0.333	0.400	0.243	0.490	0.275	0.336
20.95	-1.400	0.451	0.070	0.092	0.501	4.348	-5.149	-1.336	3.893	1.355	2.501
	0.493	0.325	0.017	0.014	0.216	0.342	0.405	0.245	0.506	0.283	0.348
23.50	-3.902	-0.353	0.126	0.148	0.526	3.922	-4.793	-1.667	3.076	1.243	2.941
	0.525	0.339	0.017	0.014	0.216	0.351	0.405	0.251	0.519	0.287	0.348
26.72	-2.812	0.001	0.151	0.176	0.593	3.926	-5.300	-1.528	3.840	1.775	2.748
	0.504	0.331	0.017	0.014	0.215	0.343	0.403	0.243	0.504	0.279	0.348
30.73	-3.417	-0.049	0.142	0.150	0.017	3.451	-4.240	-1.476	1.920	0.777	1.971
	0.530	0.343	0.017	0.015	0.231	0.364	0.411	0.256	0.538	0.299	0.368
36.28	-4.970	-0.651	0.175	0.159	-0.253	4.269	-5.434	-1.869	2.765	1.838	2.183
	0.519	0.334	0.017	0.014	0.229	0.339	0.401	0.245	0.508	0.279	0.348
44.96	-3.041	0.952	0.150	0.148	-0.832	1.722	-2.335	-0.471	0.480	1.912	1.783
	0.487	0.306	0.017	0.014	0.226	0.356	0.371	0.225	0.509	0.310	0.344

Table B4. Value of indices C4668 – Fe5782 and their errors (second line) for apertures from $+6'' - +45''$. The apertures from +8 – $+45''$ are contaminated by another galaxy in the slit.

Radius ($''$)	C4668 Å	Hβ Å	Fe5015 Å	Mg$_1$ mag	Mg$_2$ mag	Mgb Å	Fe5270 Å	Fe5335 Å	Fe5406 Å	Fe5709 Å	Fe5782 Å
6.57	6.631	1.724	5.574	0.124	0.278	4.217	2.470	2.071	1.614	0.684	0.709
	0.303	0.121	0.278	0.004	0.004	0.124	0.155	0.174	0.135	0.111	0.088
7.59	6.003	1.550	4.959	0.119	0.276	4.287	2.491	2.012	1.427	0.771	0.654
	0.335	0.133	0.290	0.005	0.004	0.130	0.163	0.175	0.146	0.117	0.095
8.61	6.563	1.793	5.784	0.120	0.279	4.385	2.718	2.172	1.544	0.540	0.699
	0.364	0.145	0.338	0.005	0.004	0.147	0.176	0.196	0.143	0.126	0.103
9.64	6.255	1.825	5.189	0.115	0.266	4.292	2.433	2.152	1.512	0.599	0.917
	0.397	0.156	0.342	0.005	0.005	0.164	0.187	0.204	0.146	0.133	0.112
10.66	5.943	1.690	5.661	0.111	0.264	4.487	2.447	2.235	1.751	0.671	0.696
	0.430	0.168	0.366	0.005	0.005	0.166	0.199	0.253	0.213	0.140	0.116
11.68	5.860	2.244	5.366	0.113	0.269	4.359	2.445	2.323	1.462	0.428	0.654
	0.460	0.176	0.412	0.006	0.005	0.187	0.210	0.230	0.166	0.148	0.125
12.77	5.721	2.012	5.057	0.121	0.267	4.298	2.452	2.284	1.628	0.372	0.583
	0.464	0.179	0.393	0.006	0.005	0.178	0.211	0.240	0.181	0.149	0.125
14.01	5.929	1.936	5.415	0.111	0.261	4.496	2.476	2.273	1.474	0.393	0.904
	0.473	0.183	0.395	0.006	0.005	0.179	0.213	0.235	0.169	0.151	0.125
15.40	5.582	2.240	5.160	0.106	0.254	4.146	2.363	2.102	1.369	0.467	0.518
	0.480	0.183	0.401	0.006	0.006	0.184	0.218	0.240	0.172	0.153	0.128
16.93	5.388	1.858	5.368	0.099	0.246	4.107	2.441	2.034	1.321	0.221	0.623
	0.495	0.190	0.418	0.006	0.006	0.191	0.225	0.254	0.186	0.158	0.132
18.76	5.212	2.025	5.489	0.097	0.247	4.309	2.341	2.239	1.110	-0.180	0.745
	0.478	0.182	0.395	0.006	0.006	0.183	0.216	0.239	0.173	0.155	0.126
20.95	5.482	2.329	5.443	0.098	0.235	4.168	2.631	2.498	1.536	-0.021	0.972
	0.488	0.185	0.409	0.006	0.006	0.187	0.223	0.255	0.187	0.157	0.129
23.50	4.987	2.458	5.914	0.098	0.244	4.235	2.431	2.381	1.316	0.127	0.940
	0.500	0.187	0.407	0.006	0.006	0.187	0.221	0.243	0.177	0.159	0.130
26.72	5.700	2.261	4.996	0.089	0.231	4.137	2.400	2.006	1.124	-0.313	0.763
	0.490	0.185	0.409	0.006	0.006	0.185	0.219	0.242	0.174	0.159	0.130
30.73	6.064	2.786	6.341	0.090	0.238	4.908	2.359	2.476	1.548	-1.036	0.608
	0.511	0.189	0.455	0.006	0.006	0.203	0.231	0.269	0.198	0.168	0.138
36.28	5.310	2.291	5.079	0.085	0.204	3.593	2.145	2.690	1.131	-0.687	0.327
	0.485	0.183	0.424	0.006	0.006	0.190	0.222	0.271	0.196	0.159	0.132
44.96	4.892	2.472	6.190	0.092	0.203	3.658	2.524	2.386	-0.018	-1.640	0.615
	0.495	0.176	0.388	0.006	0.005	0.182	0.213	0.247	0.171	0.160	0.127

Table B5. Value of indices Hδ_A – Fe4531 and their errors (second line) for apertures from $-45''$ – $+10''$ for NGC 3640.

Radius ($''$)	Hδ_A Å	Hδ_F Å	CN$_1$ mag	CN$_2$ mag	Ca4227 Å	G4300 Å	Hγ_A Å	Hγ_F Å	Fe4383 Å	Ca4455 Å	Fe4531 Å
-44.9	2.659	0.573	-0.087	-0.063	1.331	3.467	-3.864	-0.993	2.400	1.799	2.977
	0.384	0.281	0.016	0.011	0.168	0.291	0.340	0.206	0.451	0.251	0.300
-31.5	2.830	0.673	-0.099	-0.088	0.965	4.190	-4.648	-0.601	3.682	1.275	2.946
	0.436	0.322	0.017	0.014	0.200	0.331	0.388	0.230	0.487	0.276	0.334
-25.5	1.495	0.785	-0.079	-0.071	1.122	3.836	-4.754	-0.798	3.705	1.177	3.328
	0.457	0.324	0.017	0.014	0.194	0.334	0.392	0.234	0.490	0.276	0.331
-21.5	0.485	0.190	-0.067	-0.032	0.729	3.626	-5.133	-1.110	4.983	1.611	2.845
	0.473	0.334	0.017	0.014	0.202	0.342	0.395	0.239	0.479	0.273	0.338
-18.7	0.520	0.546	-0.023	-0.003	0.803	4.710	-4.850	-1.100	4.076	1.270	2.323
	0.466	0.325	0.017	0.014	0.203	0.325	0.394	0.239	0.486	0.274	0.338
-16.4	-0.413	0.411	-0.015	0.012	1.493	4.106	-4.656	-0.738	4.615	1.188	2.688
	0.473	0.323	0.017	0.013	0.185	0.328	0.388	0.232	0.476	0.273	0.331
-14.6	0.244	0.614	-0.014	0.009	1.030	4.551	-5.274	-1.116	4.069	1.240	2.834
	0.479	0.330	0.017	0.014	0.199	0.329	0.399	0.240	0.488	0.277	0.337
-13.1	0.130	0.385	-0.033	-0.010	1.375	3.992	-4.314	-0.969	4.220	1.052	3.049
	0.484	0.336	0.017	0.014	0.195	0.341	0.399	0.243	0.492	0.280	0.339
-11.9	-0.065	0.181	-0.031	-0.006	0.873	4.673	-5.451	-1.248	5.108	1.289	2.811
	0.481	0.335	0.017	0.014	0.204	0.334	0.403	0.244	0.480	0.276	0.339
-10.8	0.083	0.542	-0.017	0.012	1.022	4.332	-5.250	-1.085	5.138	1.516	2.962
	0.480	0.330	0.017	0.014	0.200	0.334	0.400	0.239	0.478	0.272	0.335
-9.8	1.048	0.947	-0.057	-0.030	1.047	4.651	-5.173	-1.194	4.615	1.425	2.240
	0.447	0.311	0.016	0.013	0.189	0.312	0.378	0.227	0.458	0.262	0.321
-8.8	0.250	0.591	-0.033	0.000	0.968	4.574	-5.215	-1.251	4.438	1.268	2.403
	0.436	0.302	0.016	0.012	0.179	0.294	0.359	0.215	0.436	0.254	0.302
-7.7	0.309	0.542	-0.043	-0.016	1.214	4.527	-5.170	-1.322	4.578	1.445	2.615
	0.414	0.288	0.016	0.011	0.164	0.275	0.338	0.202	0.411	0.242	0.279
-6.7	-0.290	0.292	-0.021	0.009	0.857	4.698	-5.070	-1.117	4.155	1.095	2.573
	0.400	0.278	0.015	0.011	0.161	0.258	0.320	0.189	0.391	0.236	0.263
-5.7	-0.174	0.467	-0.031	-0.010	1.023	4.562	-5.199	-1.196	4.431	1.245	2.605
	0.376	0.260	0.015	0.010	0.146	0.238	0.299	0.175	0.362	0.223	0.243
-4.7	-0.073	0.571	-0.023	0.011	1.124	4.700	-5.378	-1.196	4.837	1.221	2.538
	0.354	0.246	0.015	0.009	0.134	0.217	0.279	0.160	0.336	0.213	0.223
-3.6	-0.417	0.287	-0.014	0.013	1.060	4.949	-6.032	-1.521	4.911	1.329	2.599
	0.335	0.233	0.014	0.008	0.123	0.196	0.260	0.147	0.311	0.203	0.202
-2.6	-0.452	0.487	-0.008	0.022	1.156	4.808	-5.684	-1.402	4.878	1.371	2.782
	0.312	0.217	0.014	0.007	0.111	0.173	0.236	0.130	0.285	0.193	0.179
-1.6	-0.495	0.343	0.002	0.033	1.039	4.831	-5.885	-1.305	5.334	1.464	2.837
	0.289	0.203	0.014	0.006	0.099	0.150	0.214	0.114	0.258	0.184	0.156
-0.6	-0.751	0.301	0.035	0.065	1.117	4.878	-6.030	-1.455	5.421	1.500	3.119
	0.268	0.189	0.014	0.006	0.086	0.127	0.192	0.098	0.234	0.175	0.132
0.4	-1.238	0.091	0.049	0.082	1.163	4.730	-6.170	-1.619	5.699	1.509	3.072
	0.255	0.181	0.013	0.005	0.078	0.115	0.181	0.089	0.222	0.171	0.123
1.5	-1.132	0.202	0.032	0.064	1.127	4.933	-6.276	-1.554	5.387	1.569	2.993
	0.262	0.185	0.013	0.006	0.084	0.125	0.191	0.097	0.234	0.175	0.136
2.5	-0.523	0.444	0.004	0.032	1.072	4.826	-6.081	-1.491	5.211	1.450	2.765
	0.280	0.196	0.014	0.006	0.096	0.148	0.213	0.113	0.259	0.184	0.160
3.5	-0.370	0.427	-0.013	0.012	1.069	4.753	-5.736	-1.360	5.075	1.370	2.536
	0.303	0.212	0.014	0.007	0.110	0.171	0.236	0.130	0.285	0.194	0.184
4.5	-0.279	0.478	-0.016	0.015	1.077	5.034	-6.086	-1.546	4.978	1.426	2.477
	0.326	0.226	0.014	0.008	0.122	0.193	0.259	0.146	0.311	0.204	0.206
5.5	0.031	0.457	-0.020	0.009	1.307	4.743	-5.617	-1.340	4.515	1.157	2.848
	0.344	0.240	0.015	0.009	0.130	0.214	0.279	0.160	0.339	0.215	0.224
6.6	-0.147	0.522	-0.022	0.004	1.081	4.607	-5.443	-1.272	4.655	1.377	2.655
	0.367	0.254	0.015	0.010	0.143	0.235	0.298	0.174	0.361	0.223	0.245
7.6	-0.149	0.543	-0.031	-0.007	1.024	4.528	-5.626	-1.481	4.587	1.111	2.742
	0.388	0.268	0.015	0.011	0.154	0.256	0.320	0.190	0.388	0.235	0.264
8.6	-0.339	0.283	-0.030	-0.002	1.213	4.393	-5.388	-1.233	4.589	1.378	2.747
	0.411	0.285	0.016	0.011	0.163	0.276	0.339	0.201	0.411	0.243	0.284
9.6	0.400	0.658	-0.038	-0.004	1.073	4.687	-5.824	-1.455	4.868	1.353	3.083
	0.427	0.295	0.016	0.012	0.174	0.289	0.361	0.215	0.430	0.254	0.299

Table B6. Value of indices C4668 – Fe5782 and their errors (second line) for apertures from $-45'' - +10''$ for NGC 3640.

Radius ($''$)	C4668 Å	Hβ Å	Fe5015 Å	Mg_1 mag	Mg_2 mag	Mgb Å	Fe5270 Å	Fe5335 Å	Fe5406 Å	Fe5709 Å	Fe5782 Å
-44.9	4.612	4.792	2.466	0.083	0.222	4.057	2.484	1.566	1.735	1.031	1.084
	0.432	0.150	0.358	0.005	0.005	0.157	0.192	0.213	0.150	0.126	0.115
-31.5	5.037	3.135	3.909	0.067	0.212	3.368	2.122	1.506	1.442	0.721	0.565
	0.478	0.176	0.393	0.006	0.006	0.181	0.215	0.236	0.167	0.140	0.130
-25.5	4.717	2.707	3.760	0.079	0.216	3.757	2.796	1.967	1.519	0.723	0.646
	0.480	0.179	0.395	0.006	0.006	0.177	0.210	0.231	0.167	0.140	0.129
-21.5	4.531	2.320	4.364	0.078	0.213	3.618	2.280	1.579	1.346	0.870	0.884
	0.483	0.182	0.393	0.006	0.006	0.179	0.215	0.236	0.168	0.139	0.128
-18.7	4.787	2.313	4.392	0.078	0.217	3.612	2.021	1.604	1.448	0.759	0.768
	0.478	0.181	0.391	0.006	0.006	0.178	0.215	0.234	0.166	0.139	0.127
-16.4	4.885	2.073	4.724	0.072	0.213	3.528	2.026	1.825	1.501	0.885	0.765
	0.471	0.181	0.385	0.006	0.005	0.177	0.212	0.229	0.164	0.136	0.125
-14.6	5.249	1.974	3.653	0.090	0.226	3.634	2.458	1.809	1.494	0.699	0.692
	0.477	0.183	0.398	0.006	0.006	0.179	0.213	0.232	0.167	0.139	0.127
-13.1	4.010	2.304	4.634	0.088	0.224	3.687	2.241	2.165	1.240	1.018	0.667
	0.491	0.184	0.399	0.006	0.006	0.182	0.217	0.234	0.171	0.139	0.130
-11.9	4.683	2.375	4.937	0.094	0.230	3.823	2.236	2.000	1.514	0.783	0.652
	0.482	0.181	0.393	0.006	0.006	0.179	0.214	0.232	0.167	0.139	0.128
-10.8	4.734	2.173	4.890	0.090	0.229	3.518	2.444	1.751	1.400	0.807	0.663
	0.478	0.181	0.390	0.006	0.005	0.180	0.211	0.232	0.166	0.138	0.127
-9.8	4.736	1.892	5.043	0.086	0.223	3.769	2.272	1.923	1.330	0.941	0.612
	0.450	0.173	0.368	0.006	0.005	0.168	0.201	0.218	0.158	0.131	0.122
-8.8	4.503	2.027	5.001	0.083	0.220	3.514	2.184	1.972	1.445	1.038	0.661
	0.423	0.162	0.346	0.005	0.005	0.159	0.191	0.206	0.148	0.123	0.115
-7.7	4.717	1.878	4.551	0.083	0.223	3.448	2.284	1.983	1.211	0.804	0.660
	0.393	0.152	0.325	0.005	0.005	0.149	0.180	0.193	0.140	0.117	0.108
-6.7	3.776	1.717	4.827	0.090	0.232	3.773	2.333	1.991	1.419	0.804	0.634
	0.371	0.143	0.305	0.005	0.004	0.138	0.171	0.181	0.131	0.111	0.102
-5.7	4.516	2.131	4.707	0.090	0.226	3.643	2.266	1.932	1.365	0.867	0.730
	0.338	0.130	0.281	0.005	0.004	0.127	0.160	0.169	0.121	0.103	0.095
-4.7	4.515	1.977	4.983	0.089	0.230	3.722	2.404	2.007	1.512	0.873	0.659
	0.308	0.119	0.257	0.004	0.004	0.116	0.148	0.155	0.110	0.096	0.088
-3.6	5.190	1.890	4.687	0.094	0.232	3.744	2.374	1.952	1.363	0.969	0.737
	0.273	0.108	0.233	0.004	0.004	0.104	0.137	0.141	0.100	0.087	0.081
-2.6	5.859	1.803	5.444	0.094	0.244	3.815	2.516	2.218	1.466	0.941	0.818
	0.237	0.096	0.206	0.004	0.004	0.090	0.125	0.126	0.089	0.080	0.074
-1.6	5.573	1.884	5.488	0.105	0.254	4.010	2.632	2.281	1.516	0.947	0.900
	0.203	0.082	0.179	0.004	0.004	0.078	0.114	0.112	0.078	0.072	0.066
-0.6	6.807	1.921	5.900	0.116	0.273	4.234	2.829	2.523	1.692	1.008	0.905
	0.165	0.070	0.155	0.004	0.003	0.066	0.104	0.099	0.068	0.066	0.061
0.4	7.169	1.913	6.149	0.112	0.272	4.386	2.887	2.549	1.613	1.022	0.819
	0.151	0.067	0.149	0.004	0.003	0.064	0.103	0.098	0.068	0.067	0.062
1.5	6.418	1.877	5.615	0.104	0.253	4.066	2.776	2.438	1.602	0.924	0.910
	0.175	0.075	0.169	0.004	0.004	0.074	0.112	0.109	0.076	0.073	0.067
2.5	5.718	1.980	5.510	0.093	0.240	3.990	2.484	2.174	1.556	1.011	0.861
	0.213	0.088	0.195	0.004	0.004	0.087	0.123	0.124	0.087	0.080	0.074
3.5	5.273	1.835	5.054	0.089	0.234	3.868	2.495	2.077	1.495	1.015	0.830
	0.251	0.102	0.223	0.004	0.004	0.100	0.135	0.139	0.099	0.089	0.082
4.5	4.959	1.878	4.740	0.082	0.226	3.871	2.509	1.930	1.490	0.991	0.725
	0.285	0.115	0.249	0.004	0.004	0.112	0.146	0.154	0.109	0.096	0.089
5.5	4.451	1.959	4.987	0.089	0.226	3.783	2.283	2.049	1.619	0.928	0.694
	0.317	0.125	0.271	0.005	0.004	0.123	0.157	0.166	0.118	0.103	0.096
6.6	4.716	2.065	4.957	0.087	0.225	3.585	2.415	1.695	1.414	0.773	0.690
	0.345	0.135	0.294	0.005	0.004	0.135	0.167	0.180	0.129	0.111	0.102
7.6	4.505	1.958	4.813	0.084	0.227	3.732	2.179	2.076	1.463	0.797	0.782
	0.374	0.146	0.317	0.005	0.005	0.146	0.179	0.192	0.138	0.118	0.108
8.6	5.331	1.913	4.921	0.081	0.222	3.736	2.153	1.974	1.620	0.850	0.771
	0.400	0.158	0.339	0.005	0.005	0.155	0.190	0.204	0.147	0.125	0.116
9.6	4.220	1.918	4.954	0.085	0.223	3.928	2.217	2.020	1.506	0.786	0.704
	0.431	0.167	0.359	0.006	0.005	0.164	0.199	0.217	0.156	0.132	0.122

Table B7. Value of indices Hδ_A – Fe4531 and their errors (second line) for apertures from $+10'' - +43''$ for NGC 3640.

Radius ($''$)	Hδ_A Å	Hδ_F Å	CN_1 mag	CN_2 mag	Ca4227 Å	G4300 Å	Hγ_A Å	Hγ_F Å	Fe4383 Å	Ca4455 Å	Fe4531 Å
10.7	-0.384	0.547	-0.019	0.008	1.115	4.938	-5.001	-1.099	4.377	1.333	2.678
	0.455	0.311	0.016	0.013	0.185	0.306	0.377	0.227	0.457	0.264	0.322
11.8	-0.208	0.554	-0.038	-0.013	0.992	4.747	-5.169	-1.267	4.236	1.237	2.701
	0.451	0.310	0.016	0.013	0.188	0.307	0.377	0.229	0.462	0.266	0.321
13.0	0.866	0.643	-0.056	-0.033	1.056	4.215	-4.905	-0.933	4.813	0.950	2.683
	0.449	0.314	0.016	0.013	0.189	0.317	0.381	0.227	0.462	0.272	0.328
14.5	0.133	0.056	-0.041	-0.012	1.269	4.832	-5.397	-1.194	4.403	1.048	2.191
	0.450	0.317	0.016	0.013	0.184	0.306	0.379	0.228	0.460	0.268	0.327
15.5	2.021	1.273	-0.085	-0.054	1.487	4.900	-5.573	-0.941	4.822	1.536	2.297
	0.673	0.469	0.022	0.020	0.297	0.519	0.629	0.380	0.755	0.398	0.556
17.1	0.752	0.555	-0.037	-0.011	1.130	4.732	-5.543	-1.423	4.416	1.165	2.403
	0.419	0.295	0.016	0.012	0.172	0.287	0.358	0.215	0.434	0.254	0.304
19.9	0.211	0.648	-0.032	-0.010	1.212	4.452	-5.225	-0.972	4.759	1.439	2.954
	0.429	0.295	0.016	0.012	0.175	0.293	0.360	0.213	0.437	0.254	0.303
23.9	0.542	0.539	-0.035	-0.008	1.374	4.266	-4.803	-0.803	4.295	1.177	2.388
	0.428	0.300	0.016	0.012	0.171	0.298	0.358	0.212	0.439	0.259	0.309
29.9	1.374	1.144	-0.056	-0.044	0.565	4.018	-4.812	-0.773	3.787	0.840	2.558
	0.425	0.295	0.016	0.012	0.186	0.300	0.359	0.213	0.446	0.263	0.315
43.3	2.885	-0.008	-0.105	-0.111	0.992	4.184	-5.539	-1.075	4.341	0.832	2.210
	0.392	0.299	0.016	0.012	0.172	0.289	0.354	0.208	0.434	0.259	0.309

Table B8. Value of indices C4668 – Fe5782 and their errors (second line) for apertures from $+10'' - +43''$ for NGC 3640.

Radius ($''$)	C4668 Å	Hβ Å	Fe5015 Å	Mg_1 mag	Mg_2 mag	Mgb Å	Fe5270 Å	Fe5335 Å	Fe5406 Å	Fe5709 Å	Fe5782 Å
10.7	4.665	2.031	4.897	0.085	0.222	3.616	2.307	2.091	1.396	0.914	0.643
	0.458	0.178	0.383	0.006	0.005	0.177	0.211	0.230	0.167	0.139	0.130
11.8	4.708	1.709	4.791	0.086	0.231	3.911	2.487	2.149	1.341	0.898	0.485
	0.461	0.181	0.384	0.006	0.005	0.177	0.210	0.229	0.167	0.139	0.130
13.0	4.724	2.046	4.588	0.081	0.228	3.890	2.519	2.109	1.767	1.160	0.752
	0.469	0.181	0.391	0.006	0.006	0.179	0.213	0.233	0.167	0.140	0.130
14.5	4.561	1.857	4.822	0.079	0.219	3.690	2.534	1.934	1.528	0.889	0.726
	0.462	0.179	0.385	0.006	0.005	0.177	0.211	0.231	0.166	0.140	0.128
15.5	5.340	2.036	3.998	0.083	0.220	3.746	2.605	2.125	1.706	0.896	0.881
	0.792	0.307	0.663	0.008	0.009	0.304	0.347	0.388	0.282	0.232	0.212
17.1	4.380	1.820	3.825	0.070	0.206	3.574	2.442	1.881	1.566	0.845	0.481
	0.432	0.167	0.363	0.006	0.005	0.165	0.199	0.217	0.155	0.131	0.122
19.9	4.658	1.957	5.221	0.071	0.211	3.590	2.232	1.951	1.688	0.881	0.735
	0.435	0.169	0.361	0.006	0.005	0.167	0.201	0.218	0.157	0.133	0.122
23.9	4.746	1.993	4.552	0.075	0.204	3.523	2.742	1.969	1.409	1.084	0.806
	0.436	0.169	0.364	0.006	0.005	0.167	0.199	0.218	0.159	0.132	0.123
29.9	6.783	1.989	4.017	0.065	0.203	3.794	2.306	1.772	1.581	0.794	0.393
	0.428	0.169	0.371	0.006	0.005	0.168	0.202	0.222	0.159	0.135	0.126
43.3	6.235	1.521	3.178	0.057	0.196	3.726	2.648	1.513	2.082	1.026	0.356
	0.422	0.167	0.362	0.005	0.005	0.161	0.195	0.217	0.150	0.129	0.121
43.3	2.885	-0.008	-0.105	-0.111	0.992	4.184	-5.539	-1.075	4.341	0.832	2.210
	0.392	0.299	0.016	0.012	0.172	0.289	0.354	0.208	0.434	0.259	0.309

Table B9. Value of indices Hδ_A – Fe4531 and their errors (second line) for apertures from $-50'' - 0''$ for NGC 5044.

Radius ($''$)	Hδ_A Å	Hδ_F Å	CN$_1$ mag	CN$_2$ mag	Ca4227 Å	G4300 Å	Hγ_A Å	Hγ_F Å	Fe4383 Å	Ca4455 Å	Fe4531 Å
-49.6	-1.714	1.579	0.049	0.048	1.181	3.112	-3.993	-0.035	6.195	2.221	2.366
	0.447	0.283	0.016	0.013	0.182	0.323	0.368	0.213	0.446	0.255	0.329
-42.8	0.079	-0.347	0.042	0.064	0.998	4.447	-4.980	-1.295	4.661	0.960	1.950
	0.465	0.327	0.017	0.014	0.198	0.332	0.396	0.241	0.488	0.281	0.351
-38.2	1.824	1.570	0.005	0.037	1.663	3.782	-4.600	-0.882	5.405	0.723	3.135
	0.459	0.307	0.017	0.014	0.193	0.338	0.392	0.234	0.477	0.282	0.341
-34.5	-1.241	0.493	0.040	0.069	1.268	4.474	-5.713	-1.525	4.270	1.681	2.057
	0.494	0.326	0.017	0.014	0.202	0.337	0.404	0.243	0.491	0.273	0.352
-31.5	0.094	-0.042	0.011	0.023	0.691	5.564	-8.108	-2.759	5.554	1.227	3.258
	0.490	0.343	0.017	0.014	0.223	0.338	0.435	0.264	0.499	0.286	0.355
-29.0	-0.441	0.435	0.019	0.038	0.899	5.230	-7.279	-2.626	5.082	1.715	2.036
	0.491	0.333	0.017	0.014	0.211	0.332	0.420	0.258	0.494	0.273	0.357
-26.8	1.273	1.178	-0.013	0.012	1.108	5.820	-5.692	-1.196	4.215	1.283	3.205
	0.472	0.322	0.017	0.014	0.200	0.321	0.407	0.243	0.493	0.276	0.343
-24.9	-0.706	0.728	0.025	0.101	0.828	4.716	-5.662	-1.710	4.712	1.096	2.877
	0.495	0.331	0.017	0.014	0.204	0.339	0.410	0.250	0.495	0.281	0.349
-23.2	-0.698	0.328	0.042	0.073	0.649	4.519	-5.619	-2.035	4.056	1.564	2.783
	0.496	0.333	0.017	0.014	0.205	0.336	0.403	0.249	0.494	0.273	0.345
-21.7	-1.379	-0.190	0.032	0.061	1.051	4.520	-6.440	-2.050	4.404	1.303	2.490
	0.498	0.337	0.017	0.014	0.199	0.335	0.406	0.248	0.487	0.275	0.342
-20.3	-1.071	-0.014	0.032	0.053	1.087	4.852	-7.034	-2.649	5.590	1.273	2.568
	0.492	0.333	0.017	0.014	0.199	0.330	0.408	0.252	0.472	0.271	0.342
-19.1	-1.280	-0.108	0.035	0.055	0.980	4.085	-6.201	-2.347	5.105	1.053	3.075
	0.495	0.335	0.017	0.014	0.202	0.340	0.405	0.251	0.480	0.275	0.339
-18.0	0.303	1.327	-0.021	0.004	0.928	4.802	-6.986	-2.751	5.125	1.013	2.668
	0.490	0.324	0.017	0.014	0.209	0.337	0.420	0.262	0.493	0.280	0.350
-16.9	-1.823	-0.553	0.058	0.083	1.033	5.261	-6.298	-2.098	4.212	1.497	2.319
	0.491	0.335	0.017	0.014	0.201	0.318	0.399	0.244	0.478	0.269	0.339
-15.9	-2.584	-0.218	0.078	0.096	1.403	4.997	-6.857	-2.123	5.002	1.259	3.054
	0.484	0.319	0.016	0.013	0.184	0.308	0.387	0.233	0.456	0.263	0.319
-14.9	-1.974	-0.016	0.065	0.100	1.229	4.955	-6.677	-2.408	4.310	1.548	2.730
	0.462	0.307	0.016	0.012	0.179	0.293	0.370	0.225	0.444	0.251	0.306
-13.9	-1.291	-0.189	0.052	0.074	1.272	5.283	-6.931	-2.415	5.027	1.360	2.977
	0.440	0.299	0.016	0.012	0.172	0.279	0.356	0.215	0.419	0.244	0.291
-12.8	-1.649	-0.235	0.073	0.098	1.428	4.929	-6.640	-2.312	5.107	1.395	3.264
	0.428	0.288	0.016	0.011	0.162	0.268	0.341	0.204	0.402	0.238	0.276
-11.8	-0.912	-0.098	0.041	0.068	1.027	4.939	-6.400	-2.234	5.342	1.255	2.674
	0.409	0.278	0.015	0.011	0.162	0.257	0.326	0.195	0.384	0.231	0.267
-10.8	-1.497	-0.495	0.052	0.080	1.266	4.826	-6.704	-2.483	4.661	1.308	3.336
	0.401	0.275	0.015	0.010	0.150	0.246	0.315	0.188	0.376	0.225	0.252
-9.8	-1.290	-0.023	0.067	0.093	0.929	5.030	-6.792	-2.399	5.224	1.344	3.260
	0.384	0.259	0.015	0.010	0.147	0.231	0.301	0.178	0.355	0.218	0.239
-8.8	-1.767	-0.974	0.049	0.070	1.197	4.915	-7.001	-2.606	5.106	1.575	3.092
	0.375	0.259	0.015	0.009	0.139	0.222	0.290	0.171	0.343	0.210	0.229
-7.7	-1.560	-0.345	0.072	0.104	1.167	5.370	-6.973	-2.451	5.441	1.531	3.007
	0.360	0.245	0.015	0.009	0.133	0.205	0.277	0.161	0.325	0.205	0.218
-6.7	-1.724	-0.168	0.058	0.093	1.297	4.727	-6.861	-2.579	5.225	1.379	2.769
	0.347	0.233	0.014	0.008	0.124	0.198	0.262	0.151	0.311	0.199	0.206
-5.7	-1.346	-0.167	0.064	0.100	1.045	5.049	-7.144	-2.592	5.316	1.283	2.841
	0.333	0.225	0.014	0.008	0.120	0.183	0.250	0.142	0.297	0.194	0.194
-4.7	-1.450	-0.061	0.067	0.098	1.207	5.132	-7.208	-2.592	5.223	1.365	2.809
	0.319	0.215	0.014	0.007	0.111	0.169	0.236	0.132	0.281	0.188	0.181
-3.6	-1.357	-0.176	0.077	0.112	1.275	5.297	-7.692	-2.828	5.437	1.364	2.798
	0.307	0.208	0.014	0.007	0.104	0.158	0.225	0.124	0.268	0.183	0.171
-2.6	-1.621	-0.155	0.082	0.117	1.147	5.073	-7.657	-3.043	5.185	1.373	3.007
	0.299	0.202	0.014	0.006	0.100	0.148	0.215	0.117	0.259	0.179	0.161
-1.6	-1.920	-0.466	0.086	0.117	1.166	5.087	-7.325	-2.727	5.316	1.428	2.887
	0.291	0.197	0.014	0.006	0.095	0.140	0.207	0.110	0.249	0.176	0.152
-0.6	-1.929	-0.477	0.094	0.127	1.131	5.268	-8.207	-3.268	5.295	1.308	2.928
	0.284	0.193	0.014	0.006	0.091	0.133	0.201	0.106	0.241	0.173	0.146

Table B10. Value of indices C4668 – Fe5782 and their errors (second line) for apertures from $-50'' - 0''$ for NGC 5044.

Radius ($''$)	C4668 Å	Hβ Å	Fe5015 Å	Mg_1 mag	Mg_2 mag	Mgb Å	Fe5270 Å	Fe5335 Å	Fe5406 Å	Fe5709 Å	Fe5782 Å
-49.6	4.856	0.656	2.929	0.126	0.256	4.089	2.986	0.720	2.039	1.193	1.567
	0.465	0.193	0.393	0.006	0.005	0.178	0.208	0.234	0.164	0.157	0.122
-42.8	3.715	0.565	4.931	0.135	0.287	4.911	2.851	1.184	1.464	1.218	1.427
	0.495	0.203	0.407	0.006	0.006	0.187	0.219	0.246	0.184	0.162	0.130
-38.2	2.629	0.825	5.309	0.151	0.304	4.422	2.524	1.199	1.460	0.745	1.478
	0.497	0.200	0.400	0.006	0.006	0.186	0.218	0.241	0.175	0.164	0.127
-34.5	4.890	-0.763	5.450	0.152	0.295	5.028	2.370	1.616	1.258	0.901	0.831
	0.490	0.211	0.406	0.006	0.006	0.184	0.223	0.242	0.180	0.165	0.131
-31.5	5.427	-1.199	4.821	0.152	0.283	5.032	2.753	1.269	1.533	0.723	1.260
	0.502	0.220	0.420	0.006	0.006	0.189	0.226	0.251	0.185	0.169	0.132
-29.0	6.196	-0.152	5.707	0.126	0.270	4.647	2.421	1.851	1.536	0.810	0.905
	0.490	0.210	0.407	0.006	0.006	0.189	0.224	0.245	0.181	0.167	0.133
-26.8	5.806	0.411	4.921	0.135	0.276	4.851	2.873	1.461	1.541	0.854	0.796
	0.483	0.203	0.405	0.006	0.006	0.186	0.220	0.244	0.179	0.166	0.132
-24.9	5.574	0.751	4.614	0.130	0.267	4.647	2.267	1.835	1.272	0.446	0.902
	0.490	0.204	0.419	0.006	0.006	0.193	0.226	0.252	0.184	0.169	0.134
-23.2	4.934	0.440	4.916	0.132	0.272	4.509	2.264	1.835	1.417	0.846	0.812
	0.487	0.203	0.404	0.006	0.006	0.186	0.221	0.242	0.180	0.166	0.131
-21.7	5.542	0.238	4.244	0.142	0.282	4.750	1.136	1.884	1.526	0.707	0.675
	0.478	0.203	0.403	0.006	0.006	0.182	0.225	0.237	0.176	0.165	0.131
-20.3	6.389	0.333	4.730	0.139	0.282	4.790	0.992	1.786	1.683	0.844	0.861
	0.472	0.202	0.397	0.006	0.006	0.181	0.225	0.237	0.172	0.164	0.130
-19.1	4.498	-0.035	4.878	0.139	0.289	4.822	1.134	2.003	1.546	0.838	0.982
	0.485	0.205	0.400	0.006	0.006	0.183	0.225	0.236	0.176	0.164	0.130
-18.0	4.635	0.420	5.392	0.148	0.292	4.803	1.463	2.373	1.552	0.709	0.882
	0.496	0.207	0.417	0.006	0.006	0.189	0.228	0.243	0.192	0.168	0.134
-16.9	5.870	0.435	4.840	0.137	0.295	4.794	1.658	2.117	1.461	0.755	0.845
	0.468	0.199	0.397	0.006	0.006	0.181	0.218	0.234	0.183	0.162	0.128
-15.9	5.452	0.307	4.081	0.140	0.298	4.793	1.307	1.946	1.460	0.745	0.691
	0.448	0.192	0.379	0.006	0.005	0.171	0.212	0.225	0.169	0.157	0.124
-14.9	5.938	0.218	4.701	0.136	0.293	4.874	1.872	2.047	1.382	0.669	0.669
	0.425	0.184	0.358	0.005	0.005	0.162	0.200	0.212	0.157	0.153	0.119
-13.9	6.582	0.257	4.314	0.143	0.303	4.961	1.949	1.924	1.409	0.757	0.966
	0.401	0.176	0.348	0.005	0.005	0.156	0.192	0.205	0.152	0.148	0.113
-12.8	6.519	0.709	4.672	0.146	0.306	5.134	2.272	2.042	1.371	0.681	0.696
	0.382	0.167	0.326	0.005	0.005	0.147	0.183	0.194	0.145	0.145	0.111
-11.8	5.943	0.251	4.723	0.143	0.302	4.874	2.425	2.107	1.466	0.594	0.621
	0.367	0.162	0.310	0.005	0.004	0.142	0.175	0.186	0.139	0.141	0.106
-10.8	6.080	0.530	4.585	0.145	0.308	5.038	2.418	1.954	1.550	0.700	0.998
	0.347	0.154	0.296	0.005	0.004	0.134	0.171	0.187	0.131	0.137	0.101
-9.8	6.295	0.446	4.978	0.140	0.302	5.060	2.269	2.058	1.505	0.566	0.975
	0.326	0.148	0.280	0.005	0.004	0.130	0.162	0.170	0.127	0.134	0.097
-8.8	6.146	0.329	4.388	0.144	0.312	5.060	2.312	2.064	1.362	0.819	0.883
	0.311	0.142	0.267	0.004	0.004	0.130	0.156	0.161	0.120	0.130	0.093
-7.7	6.110	0.308	4.434	0.152	0.311	5.098	2.495	1.981	1.495	0.777	0.913
	0.294	0.136	0.253	0.004	0.004	0.121	0.149	0.153	0.115	0.127	0.091
-6.7	6.283	0.289	4.530	0.149	0.309	5.269	2.254	2.229	1.539	0.804	0.821
	0.273	0.129	0.238	0.004	0.004	0.114	0.143	0.145	0.109	0.123	0.086
-5.7	6.296	0.336	4.353	0.149	0.310	5.183	2.368	2.191	1.536	0.722	0.887
	0.256	0.123	0.223	0.004	0.004	0.101	0.137	0.136	0.102	0.120	0.082
-4.7	6.502	0.549	4.311	0.150	0.313	5.181	2.378	2.140	1.570	0.746	0.865
	0.235	0.115	0.212	0.004	0.004	0.095	0.130	0.130	0.099	0.117	0.078
-3.6	6.493	0.123	4.182	0.153	0.317	5.337	2.529	2.113	1.673	0.759	0.886
	0.219	0.111	0.196	0.004	0.004	0.088	0.124	0.158	0.148	0.114	0.075
-2.6	6.557	0.008	4.167	0.158	0.320	5.364	2.550	2.173	1.583	0.771	0.915
	0.204	0.107	0.184	0.004	0.004	0.084	0.133	0.161	0.088	0.112	0.072
-1.6	6.481	-0.039	4.027	0.156	0.319	5.440	2.521	2.184	1.471	0.727	0.877
	0.191	0.102	0.174	0.004	0.004	0.119	0.116	0.110	0.085	0.110	0.076
-0.6	6.044	-0.734	2.618	0.159	0.312	5.678	2.428	2.091	1.477	0.794	0.961
	0.180	0.099	0.181	0.004	0.003	0.079	0.114	0.110	0.086	0.109	0.068

Table B11. Value of indices Hδ_A – Fe4531 and their errors (second line) for apertures from $0'' - +50''$ for NGC 5044.

Radius ($''$)	Hδ_A Å	Hδ_F Å	CN$_1$ mag	CN$_2$ mag	Ca4227 Å	G4300 Å	Hγ_A Å	Hγ_F Å	Fe4383 Å	Ca4455 Å	Fe4531 Å
0.4	-2.142	-0.418	0.110	0.146	1.198	5.350	-8.450	-3.455	5.289	1.338	2.879
	0.284	0.192	0.014	0.006	0.091	0.133	0.201	0.106	0.241	0.173	0.146
1.5	-1.832	-0.361	0.089	0.121	1.191	5.132	-7.558	-2.945	5.131	1.504	2.900
	0.292	0.198	0.014	0.006	0.095	0.141	0.207	0.111	0.250	0.176	0.153
2.5	-1.751	-0.202	0.088	0.120	1.163	5.262	-7.747	-2.978	5.539	1.434	3.009
	0.306	0.206	0.014	0.006	0.103	0.154	0.222	0.122	0.263	0.181	0.166
3.5	-2.137	-0.532	0.086	0.119	1.250	5.103	-7.392	-2.846	5.372	1.320	2.948
	0.316	0.214	0.014	0.007	0.107	0.164	0.230	0.128	0.274	0.185	0.175
4.5	-1.185	0.027	0.065	0.098	1.196	5.186	-7.028	-2.482	5.122	1.540	2.996
	0.325	0.220	0.014	0.007	0.115	0.175	0.242	0.135	0.288	0.189	0.186
5.5	-1.676	-0.317	0.069	0.102	1.061	5.287	-7.294	-2.488	5.569	1.133	2.886
	0.340	0.230	0.014	0.008	0.121	0.187	0.255	0.145	0.300	0.196	0.198
6.6	-1.467	-0.001	0.071	0.104	1.209	5.122	-6.964	-2.359	5.013	1.230	3.202
	0.351	0.236	0.014	0.008	0.128	0.200	0.267	0.153	0.318	0.202	0.209
7.6	-0.940	0.019	0.049	0.083	1.195	4.673	-6.833	-2.607	4.898	1.336	2.904
	0.362	0.246	0.015	0.009	0.134	0.214	0.280	0.164	0.334	0.208	0.222
8.6	-1.392	-0.372	0.052	0.085	1.061	4.875	-6.556	-2.215	5.230	1.356	3.065
	0.382	0.261	0.015	0.010	0.144	0.228	0.295	0.173	0.350	0.215	0.236
9.6	-1.064	0.203	0.043	0.071	1.376	4.786	-6.508	-2.192	5.293	1.420	2.940
	0.395	0.265	0.015	0.010	0.150	0.243	0.310	0.184	0.366	0.222	0.250
10.7	-1.350	-0.107	0.051	0.079	1.214	4.768	-6.634	-2.266	5.246	1.365	3.004
	0.411	0.278	0.015	0.011	0.158	0.257	0.326	0.194	0.384	0.229	0.263
11.7	-1.335	0.095	0.065	0.103	1.162	5.208	-6.138	-1.861	4.469	1.601	2.683
	0.427	0.286	0.016	0.011	0.165	0.265	0.336	0.201	0.405	0.235	0.279
12.7	-0.190	0.267	0.041	0.077	0.925	5.395	-6.852	-2.516	4.910	1.224	2.939
	0.435	0.298	0.016	0.012	0.178	0.278	0.358	0.219	0.421	0.245	0.291
13.7	-0.907	0.272	0.038	0.057	1.082	4.807	-6.457	-2.559	4.788	1.390	2.892
	0.460	0.308	0.016	0.013	0.186	0.299	0.369	0.228	0.442	0.253	0.306
14.7	-1.494	-0.216	0.068	0.092	1.514	4.620	-5.926	-1.712	5.500	1.451	2.776
	0.480	0.325	0.016	0.013	0.186	0.312	0.383	0.230	0.453	0.261	0.322
15.8	-0.642	0.666	0.037	0.073	1.199	5.160	-6.430	-1.901	4.974	1.271	2.944
	0.489	0.326	0.017	0.014	0.195	0.321	0.402	0.243	0.473	0.270	0.336
16.8	-0.879	0.137	0.044	0.082	0.679	5.117	-6.262	-2.142	5.211	1.503	2.568
	0.511	0.348	0.017	0.014	0.216	0.337	0.418	0.257	0.491	0.276	0.350
17.8	-1.221	0.157	0.032	0.059	1.117	4.583	-6.045	-1.631	4.782	1.478	2.129
	0.530	0.354	0.018	0.015	0.214	0.356	0.429	0.260	0.512	0.285	0.369
18.9	-0.548	0.301	0.043	0.063	1.173	5.956	-7.486	-2.492	5.394	1.394	2.508
	0.512	0.348	0.018	0.015	0.208	0.338	0.434	0.267	0.501	0.281	0.360
20.1	0.872	0.861	0.018	0.044	1.729	4.341	-5.440	-1.531	5.185	1.103	2.263
	0.484	0.332	0.017	0.014	0.195	0.341	0.410	0.249	0.492	0.279	0.354
21.5	0.078	0.027	-0.011	0.010	1.087	4.431	-5.730	-2.133	4.353	0.931	2.458
	0.498	0.348	0.017	0.014	0.214	0.348	0.416	0.258	0.503	0.282	0.357
23.1	-0.951	0.707	0.034	0.059	1.349	4.838	-5.072	-1.578	3.971	0.998	2.559
	0.512	0.337	0.018	0.015	0.205	0.347	0.415	0.255	0.509	0.286	0.358
24.7	-0.225	-0.073	-0.037	-0.009	1.149	4.803	-6.976	-1.781	5.195	1.398	2.023
	0.513	0.356	0.018	0.015	0.216	0.356	0.437	0.260	0.510	0.286	0.369
26.6	0.303	-0.725	-0.021	-0.023	1.067	4.844	-6.137	-2.377	5.271	1.319	3.375
	0.503	0.360	0.018	0.015	0.216	0.346	0.427	0.267	0.505	0.285	0.354
28.8	2.349	1.410	-0.068	-0.030	0.776	4.974	-6.983	-2.410	5.890	1.298	2.932
	0.482	0.336	0.018	0.015	0.223	0.348	0.433	0.266	0.502	0.287	0.362
31.3	1.659	0.784	-0.068	-0.025	1.229	5.476	-7.149	-2.273	6.665	1.614	3.744
	0.502	0.348	0.018	0.015	0.215	0.347	0.443	0.272	0.499	0.286	0.359
34.3	3.606	0.984	-0.152	-0.139	0.916	5.755	-6.522	-2.399	6.211	1.547	2.635
	0.467	0.342	0.018	0.015	0.219	0.336	0.428	0.265	0.494	0.280	0.358
38.0	2.359	0.974	-0.108	-0.098	-0.339	5.035	-4.882	-1.292	4.927	1.901	3.778
	0.480	0.335	0.018	0.015	0.239	0.340	0.413	0.253	0.500	0.279	0.348
42.7	5.253	2.821	-0.192	-0.171	1.347	3.734	-5.089	-1.447	6.923	1.826	2.996
	0.449	0.309	0.018	0.015	0.214	0.363	0.421	0.256	0.491	0.282	0.357
49.4	5.015	2.000	-0.253	-0.202	0.985	6.309	-4.477	-0.133	5.751	2.114	2.803
	0.437	0.315	0.017	0.014	0.219	0.327	0.407	0.237	0.503	0.277	0.350

Table B12. Value of indices C4668 – Fe5782 and their errors (second line) for apertures from $0'' - +50''$ for NGC 5044.

Radius ($''$)	C4668 Å	Hβ Å	Fe5015 Å	Mg_1 mag	Mg_2 mag	Mgb Å	Fe5270 Å	Fe5335 Å	Fe5406 Å	Fe5709 Å	Fe5782 Å
0.4	6.188	-1.171	1.744	0.159	0.304	5.798	2.488	2.172	1.446	0.783	0.922
	0.181	0.100	0.173	0.004	0.003	0.080	0.114	0.111	0.087	0.109	0.068
1.5	6.360	-0.173	3.892	0.158	0.316	5.527	2.486	2.255	1.657	0.725	0.886
	0.191	0.102	0.218	0.004	0.004	0.080	0.116	0.112	0.087	0.110	0.069
2.5	6.581	-0.404	4.442	0.156	0.313	5.651	2.549	2.282	1.771	0.726	0.988
	0.211	0.111	0.193	0.004	0.004	0.089	0.122	0.122	0.096	0.113	0.073
3.5	6.366	0.063	4.397	0.155	0.318	5.468	2.534	2.221	1.805	0.801	0.890
	0.225	0.113	0.255	0.004	0.004	0.091	0.126	0.124	0.095	0.115	0.076
4.5	6.598	0.208	4.386	0.148	0.313	5.191	2.506	2.198	1.597	0.792	0.857
	0.242	0.119	0.214	0.004	0.004	0.097	0.144	0.173	0.099	0.118	0.079
5.5	6.406	0.275	4.475	0.145	0.309	5.204	2.573	2.298	1.666	0.787	0.992
	0.260	0.124	0.229	0.004	0.004	0.104	0.138	0.140	0.144	0.120	0.082
6.6	6.056	0.198	4.598	0.143	0.302	5.245	2.262	2.229	1.839	0.754	0.857
	0.280	0.131	0.248	0.004	0.004	0.112	0.146	0.160	0.135	0.124	0.087
7.6	5.586	0.351	4.225	0.147	0.306	5.033	2.403	2.049	1.424	0.694	0.800
	0.301	0.138	0.262	0.004	0.004	0.118	0.152	0.157	0.118	0.127	0.090
8.6	5.794	0.641	4.907	0.142	0.306	5.077	2.472	2.134	1.656	0.697	0.862
	0.321	0.144	0.274	0.005	0.004	0.124	0.159	0.167	0.127	0.132	0.095
9.6	5.666	0.773	4.860	0.139	0.295	4.992	2.408	1.886	1.590	0.614	1.064
	0.342	0.151	0.291	0.005	0.004	0.132	0.168	0.181	0.131	0.136	0.099
10.7	5.778	0.676	4.867	0.144	0.310	5.020	2.324	1.834	1.796	0.687	0.947
	0.363	0.159	0.309	0.005	0.004	0.143	0.176	0.188	0.143	0.140	0.105
11.7	6.089	0.858	5.543	0.138	0.301	4.941	2.438	1.994	1.550	0.529	0.812
	0.381	0.166	0.324	0.005	0.005	0.148	0.181	0.193	0.144	0.144	0.109
12.7	5.885	0.979	4.324	0.140	0.305	5.085	2.639	2.104	1.770	0.770	0.896
	0.404	0.173	0.343	0.005	0.005	0.159	0.189	0.202	0.149	0.148	0.113
13.7	5.567	0.450	4.141	0.141	0.301	4.856	2.443	1.871	1.870	0.833	0.901
	0.428	0.183	0.363	0.005	0.005	0.165	0.204	0.230	0.159	0.153	0.118
14.7	6.154	0.639	5.399	0.129	0.292	5.197	2.256	2.235	1.657	0.733	0.644
	0.446	0.190	0.379	0.006	0.005	0.172	0.210	0.236	0.186	0.158	0.125
15.8	6.025	0.827	4.398	0.135	0.291	4.741	2.504	1.873	1.337	0.774	0.853
	0.468	0.198	0.396	0.006	0.006	0.180	0.215	0.236	0.179	0.163	0.128
16.8	6.602	0.274	4.868	0.138	0.287	5.132	2.503	1.507	1.490	0.850	0.978
	0.484	0.208	0.413	0.006	0.006	0.187	0.224	0.247	0.182	0.167	0.133
17.8	5.189	0.022	4.970	0.134	0.292	4.796	2.540	1.967	1.257	0.642	0.877
	0.512	0.217	0.426	0.006	0.006	0.195	0.230	0.252	0.187	0.172	0.139
18.9	5.600	0.324	4.426	0.130	0.289	4.828	2.138	2.012	1.909	0.921	0.887
	0.502	0.212	0.430	0.006	0.006	0.197	0.231	0.256	0.197	0.169	0.136
20.1	5.824	0.090	4.168	0.119	0.283	4.758	2.022	1.730	1.571	0.668	1.046
	0.487	0.210	0.415	0.006	0.006	0.187	0.225	0.244	0.179	0.168	0.133
21.5	4.871	0.119	4.954	0.124	0.280	4.806	1.872	1.688	1.664	0.658	0.769
	0.498	0.211	0.415	0.006	0.006	0.189	0.228	0.248	0.206	0.169	0.135
23.1	4.694	0.666	4.465	0.124	0.279	4.657	2.548	1.962	1.581	0.957	0.826
	0.504	0.209	0.421	0.006	0.006	0.192	0.226	0.263	0.209	0.169	0.136
24.7	6.219	0.718	5.290	0.124	0.271	4.433	2.567	1.715	1.715	0.803	0.828
	0.506	0.213	0.435	0.006	0.006	0.202	0.235	0.259	0.195	0.172	0.139
26.6	5.219	-0.242	4.996	0.125	0.278	4.905	2.323	2.006	1.549	0.744	1.234
	0.505	0.216	0.423	0.006	0.006	0.193	0.230	0.251	0.186	0.171	0.134
28.8	3.877	0.264	6.749	0.142	0.291	5.072	2.082	1.793	2.245	0.668	1.423
	0.517	0.215	0.434	0.006	0.006	0.212	0.236	0.271	0.245	0.172	0.145
31.3	5.914	0.040	5.814	0.126	0.297	5.493	2.562	1.489	1.919	0.586	1.036
	0.511	0.218	0.429	0.006	0.006	0.195	0.233	0.260	0.197	0.173	0.139
34.3	7.072	0.045	5.383	0.136	0.307	6.010	2.428	1.670	1.913	0.632	1.665
	0.490	0.212	0.437	0.006	0.006	0.204	0.231	0.259	0.207	0.169	0.140
38.0	7.595	-0.053	5.544	0.143	0.285	4.968	2.411	1.670	1.667	0.471	1.319
	0.485	0.213	0.423	0.006	0.006	0.195	0.230	0.255	0.194	0.169	0.135
42.7	5.068	0.441	3.778	0.132	0.301	5.539	2.336	1.631	1.764	0.894	1.590
	0.510	0.214	0.437	0.006	0.006	0.200	0.234	0.255	0.190	0.168	0.138
49.4	4.122	-1.429	6.944	0.129	0.295	5.957	2.142	0.926	1.579	0.539	1.793
	0.498	0.216	0.408	0.006	0.006	0.185	0.227	0.252	0.181	0.165	0.129
49.4	5.015	2.000	-0.253	-0.202	0.985	6.309	-4.477	-0.133	5.751	2.114	2.803
	0.437	0.315	0.017	0.014	0.219	0.327	0.407	0.237	0.503	0.277	0.350

Table B13. Value of indices Hδ_A – Fe4531 and their errors (second line) for apertures from $-21''-+21''$ for A754#1.

Radius ($''$)	Hδ_A Å	Hδ_F Å	CN_1 mag	CN_2 mag	Ca4227 Å	G4300 Å	Hγ_A Å	Hγ_F Å	Fe4383 Å	Ca4455 Å	Fe4531 Å
-20.8	1.520	2.012	0.001	0.015	0.983	5.376	-3.985	-1.589	6.312	1.633	4.186
	0.351	0.240	0.010	0.013	0.198	0.355	0.391	0.248	0.614	0.372	0.319
-10.7	0.607	0.755	0.029	0.044	0.361	5.474	-4.681	-0.817	5.469	0.829	2.765
	0.382	0.269	0.010	0.013	0.202	0.356	0.393	0.242	0.606	0.333	0.320
-6.5	-1.870	0.462	0.042	0.064	1.215	5.159	-5.352	-1.605	5.346	0.811	3.085
	0.399	0.264	0.010	0.013	0.190	0.350	0.390	0.244	0.604	0.332	0.315
-4.2	-2.740	-0.329	0.092	0.125	1.173	5.979	-6.092	-2.063	5.596	1.511	3.328
	0.393	0.265	0.009	0.013	0.187	0.336	0.383	0.239	0.595	0.325	0.306
-2.7	-2.178	-0.154	0.100	0.126	1.192	5.399	-6.100	-1.846	5.411	1.479	3.152
	0.367	0.248	0.009	0.012	0.174	0.324	0.363	0.224	0.577	0.316	0.289
-1.6	-2.322	0.054	0.098	0.129	1.354	5.966	-6.886	-2.218	5.520	1.540	3.451
	0.313	0.208	0.007	0.011	0.149	0.286	0.323	0.199	0.548	0.299	0.243
-0.6	-2.521	0.010	0.125	0.155	1.328	6.219	-6.952	-2.095	5.543	1.559	3.697
	0.250	0.166	0.006	0.009	0.123	0.249	0.273	0.166	0.514	0.283	0.193
0.4	-2.726	0.095	0.123	0.167	1.436	5.773	-6.841	-2.193	5.828	1.549	3.943
	0.251	0.165	0.006	0.009	0.123	0.252	0.271	0.165	0.504	0.283	0.200
1.5	-2.813	-0.026	0.108	0.139	1.117	6.119	-6.867	-2.206	5.582	1.367	3.759
	0.318	0.210	0.007	0.011	0.151	0.283	0.320	0.197	0.538	0.298	0.237
2.6	-2.718	0.036	0.110	0.139	1.284	5.764	-6.246	-2.142	5.791	1.205	3.562
	0.378	0.250	0.009	0.012	0.173	0.322	0.363	0.226	0.575	0.316	0.284
4.0	-1.460	0.977	0.067	0.117	1.364	5.763	-6.068	-1.606	5.874	1.295	3.224
	0.393	0.252	0.009	0.013	0.181	0.339	0.384	0.236	0.592	0.324	0.304
6.5	-1.365	0.795	0.061	0.090	1.304	6.254	-5.667	-1.566	5.805	1.233	3.807
	0.382	0.254	0.009	0.013	0.184	0.334	0.379	0.235	0.590	0.324	0.296
10.9	0.898	1.921	-0.022	0.010	1.686	4.954	-4.036	-0.312	7.317	1.677	3.811
	0.400	0.267	0.010	0.013	0.197	0.379	0.406	0.247	0.611	0.337	0.326
20.9	2.491	2.728	-0.092	-0.061	1.341	4.731	-2.947	-0.773	6.498	2.073	4.125
	0.353	0.235	0.010	0.013	0.188	0.360	0.386	0.245	0.600	0.325	0.313

Table B14. Value of indices C4668 – Fe5782 and their errors (second line) for apertures from $-21''$ – $+21''$ for A754#1.

Radius ($''$)	C4668 Å	Hβ Å	Fe5015 Å	Mg_1 mag	Mg_2 mag	Mgb Å	Fe5270 Å	Fe5335 Å	Fe5406 Å	Fe5709 Å	Fe5782 Å
-20.8	7.707	0.234	5.863	0.173	0.179	2.582	-0.442	-0.090	2.215	0.205	1.076
	0.484	0.200	0.502	0.004	0.008	0.182	0.591	0.377	0.273	0.148	0.132
-10.7	8.033	1.124	4.149	0.129	0.181	2.476	0.320	0.897	1.098	0.783	0.565
	0.483	0.193	0.503	0.004	0.008	0.186	0.595	0.381	0.255	0.146	0.133
-6.5	7.737	1.213	4.187	0.135	0.215	3.491	1.147	0.746	2.119	0.590	0.777
	0.479	0.191	0.507	0.004	0.008	0.187	0.598	0.386	0.253	0.145	0.129
-4.2	6.548	1.109	5.188	0.154	0.257	4.052	1.879	1.788	1.749	0.732	0.910
	0.477	0.191	0.509	0.004	0.008	0.189	0.600	0.407	0.324	0.141	0.125
-2.7	7.232	1.350	4.585	0.181	0.292	4.171	1.942	1.624	1.874	0.832	0.693
	0.457	0.184	0.502	0.004	0.008	0.184	0.595	0.378	0.250	0.134	0.119
-1.6	7.269	1.383	5.269	0.192	0.311	4.550	2.442	2.339	2.026	0.846	0.890
	0.408	0.162	0.463	0.003	0.008	0.160	0.587	0.360	0.328	0.116	0.100
-0.6	7.377	1.372	5.698	0.206	0.328	4.622	2.625	2.333	2.223	0.812	0.840
	0.333	0.136	0.424	0.002	0.008	0.137	0.579	0.344	0.226	0.095	0.080
0.4	7.560	1.304	5.939	0.210	0.331	4.934	3.008	2.642	2.378	0.906	0.915
	0.328	0.133	0.426	0.002	0.008	0.139	0.583	0.385	0.333	0.092	0.079
1.5	7.558	1.107	5.341	0.199	0.315	4.641	2.509	2.494	1.981	1.035	0.880
	0.388	0.159	0.454	0.003	0.008	0.209	0.589	0.400	0.233	0.110	0.111
2.6	7.259	1.264	4.652	0.190	0.298	4.423	2.783	2.655	1.975	0.581	0.990
	0.451	0.181	0.508	0.003	0.008	0.191	0.593	0.377	0.256	0.130	0.119
4.0	7.403	1.063	4.249	0.163	0.266	3.899	2.624	2.980	1.531	0.833	0.672
	0.471	0.190	0.503	0.004	0.008	0.186	0.595	0.379	0.254	0.138	0.123
6.5	6.877	0.954	4.209	0.135	0.222	3.180	2.274	2.464	1.907	0.866	0.890
	0.463	0.186	0.519	0.003	0.008	0.181	0.593	0.375	0.252	0.136	0.121
10.9	7.279	0.484	3.147	0.138	0.202	3.468	2.094	2.723	1.872	0.687	0.563
	0.499	0.201	0.525	0.004	0.008	0.200	0.595	0.379	0.259	0.150	0.138
20.9	5.595	0.090	1.985	0.139	0.180	2.659	0.652	2.572	1.193	0.317	0.787
	0.499	0.203	0.507	0.004	0.008	0.179	0.591	0.369	0.251	0.148	0.130

Table B15. Value of indices Hδ_A – Fe4531 and their errors (second line) for apertures from $-7''$ – $+7''$ for A970#1.

Radius ($''$)	Hδ_A Å	Hδ_F Å	CN_1 mag	CN_2 mag	Ca4227 Å	G4300 Å	Hγ_A Å	Hγ_F Å	Fe4383 Å	Ca4455 Å	Fe4531 Å
-7.2	-0.106	0.901	-0.064	-0.036	0.493	5.048	-6.547	-1.822	3.755	1.451	1.866
	0.688	0.459	0.021	0.020	0.330	0.538	0.642	0.397	0.832	0.436	0.608
-4.2	-0.250	-0.067	0.052	0.061	1.347	4.792	-6.452	-2.205	3.728	1.362	2.046
	0.680	0.479	0.021	0.020	0.283	0.515	0.604	0.380	0.786	0.409	0.579
-2.6	-0.750	0.658	0.025	0.061	1.100	6.406	-6.535	-2.182	5.179	1.767	2.443
	0.687	0.460	0.021	0.019	0.296	0.493	0.611	0.383	0.763	0.405	0.570
-1.6	-2.313	0.343	0.079	0.120	1.416	5.671	-7.326	-2.582	5.015	1.361	2.436
	0.555	0.361	0.018	0.015	0.218	0.371	0.458	0.283	0.601	0.334	0.446
-0.6	-2.499	-0.105	0.117	0.163	1.326	5.719	-6.902	-2.316	5.394	1.707	3.416
	0.426	0.280	0.015	0.010	0.154	0.266	0.330	0.194	0.472	0.277	0.347
0.4	-3.047	-0.125	0.125	0.169	1.449	5.658	-7.018	-2.352	5.601	1.590	3.201
	0.378	0.248	0.014	0.009	0.132	0.231	0.289	0.166	0.437	0.265	0.325
1.5	-2.202	0.354	0.097	0.143	1.259	5.298	-6.452	-2.282	5.530	1.697	3.632
	0.426	0.278	0.015	0.011	0.162	0.281	0.347	0.207	0.493	0.288	0.369
2.5	-1.687	0.291	0.064	0.101	1.108	4.964	-5.428	-1.684	5.070	1.382	2.144
	0.549	0.364	0.018	0.015	0.228	0.397	0.467	0.285	0.629	0.350	0.479
4.0	-0.789	0.720	0.035	0.077	1.038	5.252	-6.343	-1.604	5.197	1.428	3.036
	0.566	0.372	0.018	0.016	0.243	0.414	0.500	0.302	0.650	0.358	0.486
7.1	-1.090	0.585	-0.037	-0.003	0.475	4.792	-5.501	-1.742	2.989	2.309	-0.552
	0.632	0.419	0.019	0.018	0.284	0.482	0.563	0.353	0.760	0.387	0.571

Table B16. Value of indices C4668 – Fe5782 and their errors (second line) for apertures from $-7''-+7''$ for A970#1.

Radius ($''$)	C4668 Å	Hβ Å	Fe5015 Å	Mg_1 mag	Mg_2 mag	Mgb Å	Fe5270 Å	Fe5335 Å	Fe5406 Å	Fe5709 Å	Fe5782 Å
-7.2	2.063	2.048	2.444	0.117	0.197	3.157	0.294	1.119	0.663	1.073	1.127
	0.878	0.315	0.707	0.007	0.009	0.317	0.372	0.418	0.358	0.239	0.245
-4.2	5.382	2.525	4.847	0.124	0.236	3.904	0.328	1.450	1.221	1.078	1.253
	0.811	0.288	0.632	0.007	0.008	0.289	0.345	0.383	0.334	0.220	0.225
-2.6	4.970	1.809	4.772	0.145	0.267	4.653	1.135	1.369	1.644	1.197	0.379
	0.815	0.293	0.629	0.007	0.008	0.284	0.339	0.381	0.333	0.214	0.227
-1.6	5.635	1.302	5.672	0.167	0.288	5.101	1.303	2.284	1.530	0.949	0.693
	0.625	0.217	0.466	0.006	0.006	0.204	0.247	0.278	0.273	0.154	0.173
-0.6	6.604	1.576	5.293	0.179	0.309	5.267	3.432	2.272	1.802	0.839	1.062
	0.490	0.152	0.311	0.005	0.005	0.182	0.179	0.203	0.232	0.110	0.147
0.4	7.216	1.268	5.576	0.175	0.301	5.620	4.549	2.486	1.993	0.844	1.017
	0.455	0.140	0.300	0.005	0.005	0.140	0.193	0.244	0.286	0.106	0.138
1.5	6.425	1.349	5.517	0.166	0.290	5.344	2.392	2.351	2.108	1.002	0.990
	0.530	0.180	0.410	0.006	0.005	0.179	0.218	0.254	0.267	0.143	0.165
2.5	5.839	1.549	4.679	0.161	0.275	4.947	1.804	1.893	2.027	0.515	1.064
	0.683	0.248	0.547	0.006	0.007	0.256	0.296	0.344	0.322	0.204	0.212
4.0	5.041	2.040	4.176	0.142	0.236	4.368	1.747	1.392	1.198	1.437	1.050
	0.707	0.255	0.555	0.006	0.007	0.253	0.300	0.348	0.313	0.201	0.214
7.1	1.315	0.993	4.574	0.119	0.228	3.741	2.687	1.448	0.918	0.351	0.927
	0.802	0.290	0.621	0.007	0.008	0.289	0.321	0.387	0.339	0.230	0.233

Table B17. Value of indices Hδ_A – Fe4531 and their errors (second line) for apertures from $-14''-+13''$ for A978#1.

Radius ($''$)	Hδ_A Å	Hδ_F Å	CN_1 mag	CN_2 mag	Ca4227 Å	G4300 Å	Hγ_A Å	Hγ_F Å	Fe4383 Å	Ca4455 Å	Fe4531 Å
-13.6	-0.189	-0.077	-0.036	0.002	1.120	4.049	-5.546	-2.409	3.442	1.059	2.970
	0.430	0.311	0.016	0.012	0.186	0.334	0.380	0.245	0.480	0.265	0.334
-7.5	-1.308	0.321	0.011	0.047	0.866	4.802	-6.797	-1.890	4.561	1.395	3.379
	0.427	0.296	0.016	0.011	0.179	0.313	0.369	0.227	0.449	0.260	0.320
-4.4	-1.148	-0.264	0.023	0.049	1.032	4.646	-6.089	-1.882	4.448	1.411	3.134
	0.358	0.259	0.015	0.009	0.142	0.256	0.299	0.185	0.369	0.220	0.263
-2.6	-1.307	-0.286	0.034	0.073	1.101	5.231	-6.040	-1.650	5.593	2.213	3.093
	0.368	0.266	0.015	0.009	0.148	0.263	0.310	0.190	0.377	0.224	0.275
-1.6	-1.495	-0.343	0.044	0.083	1.200	5.278	-6.529	-1.813	5.323	1.860	3.441
	0.306	0.224	0.014	0.007	0.112	0.207	0.244	0.148	0.309	0.199	0.218
-0.6	-1.624	-0.188	0.055	0.092	1.110	5.527	-6.814	-1.933	6.044	2.155	3.644
	0.272	0.202	0.014	0.006	0.092	0.179	0.205	0.124	0.268	0.186	0.181
0.4	-1.846	-0.410	0.057	0.096	1.227	5.503	-6.655	-1.790	5.961	2.086	3.634
	0.281	0.208	0.014	0.007	0.095	0.182	0.211	0.127	0.283	0.183	0.182
1.5	-1.091	-0.079	0.047	0.090	1.179	5.419	-6.555	-1.789	5.411	1.847	2.904
	0.329	0.239	0.014	0.008	0.122	0.220	0.260	0.158	0.318	0.197	0.223
2.5	-1.157	-0.346	0.033	0.065	1.351	5.095	-6.582	-2.030	5.183	1.811	3.458
	0.402	0.289	0.015	0.010	0.159	0.282	0.333	0.206	0.402	0.232	0.285
4.2	-0.257	0.240	0.010	0.046	1.387	4.917	-5.933	-2.016	5.221	1.565	3.025
	0.378	0.272	0.015	0.010	0.150	0.273	0.317	0.198	0.388	0.228	0.276
7.4	-0.732	0.242	-0.005	0.029	1.757	5.286	-7.053	-1.941	5.308	1.091	2.844
	0.448	0.314	0.016	0.012	0.179	0.328	0.393	0.242	0.468	0.265	0.336
13.4	1.898	1.333	-0.075	-0.032	1.498	4.272	-4.924	-1.984	4.381	-0.068	1.648
	0.445	0.318	0.016	0.013	0.193	0.350	0.396	0.253	0.499	0.282	0.354

Table B18. Value of indices C4668 – Fe5782 and their errors (second line) for apertures from $-14''$ – $+13''$ for A978#1.

Radius ($''$)	C4668 Å	Hβ Å	Fe5015 Å	Mg_1 mag	Mg_2 mag	Mgb Å	Fe5270 Å	Fe5335 Å	Fe5406 Å	Fe5709 Å	Fe5782 Å
-13.6	0.847	0.575	6.912	0.134	0.219	3.295	2.453	0.978	1.331	0.298	-0.252
	0.513	0.198	0.399	0.006	0.005	0.197	0.444	0.254	0.187	0.164	0.147
-7.5	4.809	1.212	4.718	0.135	0.234	3.643	2.108	2.411	1.470	1.003	0.384
	0.487	0.188	0.392	0.006	0.005	0.188	0.441	0.239	0.172	0.159	0.138
-4.4	5.452	1.515	5.284	0.131	0.251	4.167	2.717	2.398	1.209	0.662	0.629
	0.404	0.155	0.316	0.005	0.004	0.153	0.425	0.199	0.139	0.139	0.114
-2.6	6.379	1.590	5.567	0.142	0.267	4.292	2.907	2.552	1.892	0.660	0.497
	0.419	0.163	0.371	0.005	0.005	0.175	0.431	0.236	0.184	0.145	0.122
-1.6	5.801	1.547	6.015	0.146	0.276	4.776	3.057	2.830	1.745	0.737	0.712
	0.337	0.127	0.326	0.005	0.004	0.163	0.419	0.239	0.140	0.121	0.098
-0.6	4.943	1.463	6.102	0.148	0.285	5.104	1.175	3.209	2.218	0.940	0.754
	0.285	0.103	0.235	0.004	0.004	0.120	0.406	0.173	0.136	0.104	0.074
0.4	5.100	1.485	6.422	0.156	0.288	4.920	0.918	2.586	2.176	0.922	0.997
	0.288	0.103	0.222	0.004	0.004	0.110	0.405	0.149	0.117	0.103	0.073
1.5	5.918	1.605	5.413	0.144	0.277	4.462	2.904	2.021	1.768	0.838	0.763
	0.345	0.128	0.301	0.004	0.004	0.145	0.417	0.195	0.121	0.117	0.091
2.5	5.667	1.451	5.453	0.148	0.270	4.219	3.053	1.587	1.857	0.844	0.818
	0.432	0.164	0.343	0.005	0.005	0.169	0.430	0.217	0.160	0.141	0.118
4.2	4.149	1.584	4.863	0.149	0.256	3.814	2.849	1.813	1.804	0.835	0.379
	0.421	0.160	0.333	0.005	0.004	0.160	0.426	0.209	0.161	0.137	0.113
7.4	3.687	1.362	5.179	0.167	0.258	3.694	3.643	0.984	1.618	0.769	0.508
	0.506	0.193	0.397	0.006	0.005	0.191	0.439	0.245	0.175	0.162	0.139
13.4	0.097	1.378	4.916	0.172	0.272	3.987	3.074	-1.703	2.088	0.141	0.217
	0.537	0.201	0.426	0.006	0.005	0.209	0.449	0.271	0.225	0.169	0.147

APPENDIX C: DERIVED APERTURE DATA

Derived recession velocity, velocity dispersion, age, metallicity, [Z/H], and α-element enhancement, [E/Fe], and their 1σ errors for each aperture for each galaxy.

This paper has been typeset from a TEX/ LATEX file prepared by the author.

Table C1. Derived parameters and errors per aperture for NGC 3557. The apertures from +8 – +45″ are contaminated by another galaxy in the slit but the data are included here for completeness.

Radius (″)	RV (kms^{-1})	σ (kms^{-1})	Log(Age) Gyrs	[Z/H] dex	[E/Fe] dex
-45.04	2929± 8	36±23	0.550±0.091	-0.100±0.055	0.270±0.065
-36.13	2924± 6	63±18	1.175±0.028	-0.350±0.027	0.400±0.053
-30.88	2924± 8	73±15	1.175±0.028	-0.275±0.030	0.400±0.060
-26.86	2921± 7	89±18	1.175±0.032	-0.250±0.028	0.320±0.057
-23.65	2925± 2	99±17	1.175±0.007	-0.225±0.025	0.420±0.053
-21.09	2918± 5	107±12	1.175±0.041	-0.200±0.033	0.360±0.060
-18.91	2915± 5	111±18	1.175±0.011	-0.200±0.022	0.420±0.047
-17.08	2909± 6	149±12	1.150±0.023	-0.125±0.027	0.340±0.053
-15.55	2928± 5	146±16	1.175±0.027	-0.125±0.028	0.340±0.040
-14.16	2933± 3	156±15	1.175±0.012	-0.100±0.025	0.340±0.044
-12.92	2921± 3	164±11	1.175±0.011	-0.075±0.023	0.300±0.038
-11.82	2923± 7	162±11	1.150±0.012	-0.100±0.022	0.360±0.041
-10.80	2922± 6	149±11	1.175±0.026	-0.100±0.023	0.300±0.033
-9.78	2934± 4	181±15	1.050±0.018	0.025±0.022	0.300±0.035
-8.76	2917± 5	183±12	1.175±0.004	-0.050±0.022	0.270±0.032
-7.74	2919± 7	209±11	1.075±0.015	0.050±0.022	0.270±0.031
-6.72	2937± 5	204±12	1.075±0.009	0.075±0.015	0.300±0.024
-5.69	2922± 5	200± 6	1.075±0.010	0.075±0.016	0.270±0.023
-4.67	2928± 5	207± 8	1.125±0.000	0.050±0.014	0.300±0.021
-3.65	2930± 7	224±12	1.075±0.000	0.125±0.015	0.270±0.021
-2.63	2934± 9	229±11	1.000±0.030	0.225±0.027	0.240±0.021
-1.61	2952± 9	223±13	0.975±0.037	0.275±0.027	0.270±0.019
-0.58	3014± 7	226±13	1.075±0.004	0.225±0.014	0.270±0.016
0.44	3124± 8	245± 8	1.175±0.000	0.175±0.014	0.210±0.019
1.46	3203± 5	228± 7	1.025±0.016	0.250±0.019	0.210±0.016
2.48	3231± 5	246± 9	1.075±0.004	0.175±0.018	0.210±0.020
3.50	3223± 5	246±17	1.075±0.000	0.125±0.013	0.270±0.022
4.53	3236± 5	223± 8	1.150±0.000	0.050±0.015	0.270±0.022
5.55	3233± 5	217± 5	1.075±0.004	0.100±0.016	0.270±0.021
6.57	3236± 5	218±13	1.150±0.004	0.000±0.016	0.300±0.028
7.59	3246± 5	209± 7	1.175±0.000	-0.050±0.023	0.340±0.029
8.61	3232± 11	230±14	1.075±0.018	0.075±0.020	0.270±0.029
9.64	3230± 8	219± 8	1.075±0.019	0.000±0.023	0.300±0.033
10.66	3231± 9	238± 8	1.125±0.008	0.000±0.020	0.240±0.038
11.68	3222± 5	221± 8	1.000±0.039	0.075±0.034	0.300±0.034
12.77	3232± 9	210±10	1.075±0.017	0.000±0.026	0.320±0.038
14.01	3241± 9	231± 5	1.100±0.007	0.000±0.025	0.240±0.036
15.40	3235± 13	201±12	1.175±0.015	-0.100±0.024	0.300±0.038
16.93	3240± 15	229±18	1.125±0.015	-0.100±0.020	0.270±0.037
18.76	3237± 14	213±17	1.125±0.014	-0.075±0.023	0.240±0.036
20.95	3227± 17	229±20	0.850±0.082	0.050±0.049	0.210±0.042
23.50	3253± 12	219±26	1.000±0.054	0.000±0.041	0.210±0.044
26.72	3246± 14	237±36	1.000±0.048	-0.050±0.034	0.210±0.044
30.73	3260± 23	267±58	0.900±0.105	0.000±0.063	0.180±0.057
36.28	3254± 20	242±86	1.125±0.054	-0.300±0.039	0.380±0.074
44.96	3212± 79	254±136	0.750±0.116	-0.150±0.074	0.440±0.106

Table C2. Derived parameters and errors per aperture for NGC 3640.

Radius ($''$)	RV (kms^{-1})	σ (kms^{-1})	Log(Age) Gyrs	[Z/H] dex	[E/Fe] dex
-44.9	1199.± 10.	139.± 26.	0.850±0.080	-0.050±0.039	0.270±0.048
-31.5	1207.± 10.	131.± 12.	0.950±0.068	-0.175±0.033	0.270±0.048
-25.5	1212.± 4.	121.± 21.	0.950±0.080	-0.125±0.038	0.240±0.046
-21.5	1214.± 8.	125.± 14.	0.950±0.070	-0.125±0.041	0.180±0.052
-18.7	1216.± 6.	115.± 15.	0.950±0.067	-0.150±0.045	0.270±0.058
-16.4	1227.± 4.	119.± 17.	0.875±0.080	-0.100±0.039	0.180±0.042
-14.6	1227.± 6.	120.± 17.	1.025±0.044	-0.150±0.035	0.270±0.035
-13.1	1229.± 4.	120.± 10.	0.925±0.071	-0.100±0.036	0.270±0.045
-11.9	1240.± 6.	116.± 10.	1.100±0.008	-0.150±0.019	0.240±0.049
-10.8	1252.± 7.	126.± 14.	0.950±0.076	-0.075±0.041	0.210±0.042
-9.8	1253.± 3.	140.± 8.	1.000±0.037	-0.125±0.030	0.270±0.039
-8.8	1266.± 5.	128.± 10.	0.975±0.051	-0.125±0.031	0.180±0.045
-7.7	1269.± 5.	136.± 7.	1.050±0.025	-0.175±0.023	0.240±0.034
-6.7	1281.± 6.	150.± 6.	1.100±0.007	-0.175±0.019	0.300±0.038
-5.7	1288.± 5.	133.± 8.	0.975±0.047	-0.100±0.025	0.240±0.036
-4.7	1289.± 4.	145.± 6.	1.000±0.026	-0.100±0.019	0.210±0.030
-3.6	1294.± 5.	135.± 7.	1.050±0.012	-0.100±0.017	0.210±0.028
-2.6	1297.± 6.	136.± 9.	0.975±0.032	0.000±0.024	0.180±0.025
-1.6	1303.± 5.	144.± 7.	0.975±0.026	0.050±0.020	0.180±0.019
-0.6	1327.± 5.	143.± 7.	0.850±0.039	0.225±0.020	0.180±0.021
0.4	1352.± 5.	153.± 7.	0.875±0.031	0.250±0.017	0.180±0.013
1.5	1375.± 4.	156.± 7.	0.950±0.032	0.125±0.022	0.120±0.016
2.5	1389.± 5.	155.± 7.	1.000±0.023	0.000±0.016	0.150±0.022
3.5	1392.± 6.	151.± 6.	0.975±0.030	-0.025±0.019	0.150±0.024
4.5	1397.± 5.	152.± 10.	1.025±0.029	-0.075±0.022	0.120±0.023
5.5	1402.± 7.	153.± 4.	1.050±0.010	-0.125±0.017	0.210±0.031
6.6	1408.± 4.	145.± 9.	1.025±0.024	-0.125±0.022	0.210±0.040
7.6	1417.± 4.	147.± 10.	1.025±0.042	-0.125±0.026	0.210±0.036
8.6	1415.± 5.	148.± 7.	1.000±0.046	-0.100±0.027	0.180±0.032
9.6	1436.± 6.	145.± 8.	1.100±0.011	-0.175±0.023	0.210±0.038
10.7	1431.± 2.	150.± 6.	0.950±0.076	-0.100±0.040	0.210±0.046
11.8	1441.± 8.	143.± 7.	1.050±0.026	-0.125±0.020	0.270±0.046
13.0	1446.± 8.	150.± 10.	0.850±0.071	-0.025±0.035	0.180±0.045
14.5	1455.± 6.	130.± 6.	1.000±0.051	-0.125±0.031	0.180±0.038
15.5	1458.± 5.	131.± 2.	0.900±0.102	-0.050±0.061	0.150±0.073
17.1	1457.± 2.	128.± 6.	1.100±0.007	-0.250±0.017	0.180±0.043
19.9	1455.± 5.	138.± 6.	0.925±0.076	-0.100±0.040	0.120±0.033
23.9	1464.± 4.	134.± 9.	0.900±0.074	-0.125±0.036	0.150±0.042
29.9	1478.± 4.	109.± 5.	1.025±0.034	-0.250±0.029	0.300±0.055
43.3	1497.± 3.	125.± 13.	1.175±0.000	-0.330±0.020	0.150±0.062

Table C3. Derived parameters and errors per aperture for NGC 5044.

Radius ($''$)	RV (kms^{-1})	σ (kms^{-1})	Log(Age) Gyrs	[Z/H] dex	[E/Fe] dex
-49.6	2792.± 14.	196.± 21.	0.250±0.026	0.800±0.095	0.150±0.037
-42.8	2805.± 12.	225.± 17.	0.950±0.078	0.175±0.052	0.400±0.050
-38.2	2779.± 14.	198.± 16.	0.875±0.093	0.100±0.071	0.500±0.055
-34.5	2802.± 11.	201.± 12.	1.125±0.013	-0.075±0.042	0.360±0.056
-31.5	2801.± 12.	200.± 12.	1.175±0.008	0.075±0.030	0.480±0.052
-29.0	2791.± 8.	204.± 10.	1.075±0.042	0.100±0.033	0.380±0.043
-26.8	2756.± 8.	202.± 9.	1.050±0.018	0.100±0.038	0.480±0.036
-24.9	2774.± 15.	220.± 13.	1.175±0.007	-0.025±0.031	0.480±0.039
-23.2	2757.± 9.	197.± 12.	1.175±0.000	-0.050±0.022	0.420±0.033
-21.7	2754.± 12.	192.± 10.	1.175±0.000	-0.025±0.025	0.360±0.043
-20.3	2758.± 2.	185.± 16.	1.075±0.027	0.100±0.029	0.460±0.040
-19.1	2763.± 6.	187.± 14.	1.175±0.004	0.000±0.026	0.360±0.035
-18.0	2730.± 15.	209.± 10.	1.175±0.041	0.175±0.039	0.320±0.048
-16.9	2725.± 10.	209.± 11.	1.175±0.000	0.050±0.023	0.360±0.035
-15.9	2746.± 12.	201.± 15.	1.175±0.000	0.050±0.022	0.360±0.046
-14.9	2738.± 8.	186.± 3.	1.175±0.000	0.025±0.020	0.400±0.032
-13.9	2733.± 9.	207.± 9.	1.000±0.067	0.150±0.034	0.500±0.045
-12.8	2731.± 9.	199.± 3.	1.175±0.004	0.075±0.015	0.440±0.026
-11.8	2726.± 6.	190.± 8.	1.100±0.053	-0.200±0.063	0.180±0.079
-10.8	2725.± 9.	193.± 3.	1.175±0.004	0.075±0.017	0.420±0.026
-9.8	2736.± 10.	200.± 8.	1.175±0.000	0.075±0.023	0.420±0.038
-8.8	2727.± 9.	197.± 2.	1.175±0.000	0.075±0.020	0.500±0.031
-7.7	2731.± 9.	198.± 4.	1.175±0.000	0.075±0.020	0.460±0.032
-6.7	2733.± 10.	200.± 6.	1.100±0.027	-0.075±0.051	0.180±0.054
-5.7	2738.± 9.	197.± 2.	1.100±0.004	0.125±0.017	0.480±0.028
-4.7	2732.± 10.	203.± 7.	1.175±0.000	0.125±0.018	0.420±0.024
-3.6	2741.± 9.	210.± 4.	1.175±0.000	0.125±0.017	0.480±0.029
-2.6	2749.± 9.	213.± 4.	1.075±0.017	0.000±0.044	0.240±0.054
-1.6	2751.± 11.	216.± 4.	1.175±0.000	0.125±0.015	0.460±0.023
-0.6	2754.± 15.	223.± 8.	1.175±0.004	0.050±0.021	0.360±0.028
0.4	2758.± 16.	226.± 9.	1.175±0.000	0.075±0.014	0.360±0.025
1.5	2758.± 10.	224.± 6.	1.150±0.023	0.300±0.014	0.440±0.024
2.5	2761.± 13.	229.± 8.	0.975±0.085	0.225±0.080	0.340±0.057
3.5	2765.± 9.	224.± 5.	1.050±0.054	0.000±0.046	0.180±0.052
4.5	2761.± 10.	213.± 4.	1.150±0.000	0.125±0.013	0.440±0.021
5.5	2768.± 8.	209.± 6.	1.175±0.000	0.125±0.017	0.340±0.029
6.6	2772.± 7.	210.± 11.	1.175±0.000	0.075±0.018	0.380±0.030
7.6	2766.± 9.	204.± 8.	1.050±0.056	-0.125±0.061	0.240±0.063
8.6	2769.± 8.	198.± 12.	1.175±0.000	0.075±0.014	0.380±0.026
9.6	2765.± 7.	195.± 6.	1.175±0.000	0.050±0.016	0.400±0.028
10.7	2768.± 7.	207.± 13.	1.175±0.000	0.075±0.013	0.400±0.026
11.7	2761.± 9.	202.± 7.	1.175±0.000	0.050±0.017	0.420±0.025
12.7	2740.± 9.	197.± 4.	1.175±0.022	0.075±0.025	0.420±0.035
13.7	2764.± 10.	214.± 7.	1.175±0.000	0.025±0.018	0.460±0.033
14.7	2760.± 10.	212.± 9.	1.175±0.000	0.025±0.019	0.420±0.040
15.8	2756.± 5.	193.± 6.	0.975±0.081	0.125±0.042	0.480±0.041
16.8	2745.± 5.	206.± 11.	1.175±0.000	0.100±0.033	0.460±0.036
17.8	2755.± 6.	199.± 3.	1.175±0.000	0.000±0.025	0.420±0.040
18.9	2765.± 10.	228.± 17.	1.050±0.053	0.025±0.031	0.560±0.052
20.1	2748.± 8.	197.± 17.	1.075±0.019	0.025±0.025	0.440±0.046
21.5	2753.± 8.	209.± 6.	1.150±0.010	-0.050±0.029	0.500±0.036
23.1	2755.± 7.	210.± 5.	1.150±0.005	-0.050±0.023	0.460±0.041
24.7	2741.± 16.	222.± 14.	1.175±0.004	0.000±0.026	0.240±0.036
26.6	2741.± 11.	227.± 6.	1.175±0.000	0.000±0.023	0.320±0.040
28.8	2779.± 14.	243.± 12.	1.175±0.036	0.200±0.028	0.300±0.053
31.3	2740.± 13.	209.± 13.	1.175±0.000	0.100±0.024	0.180±0.045
34.3	2739.± 20.	258.± 19.	1.175±0.022	0.100±0.025	0.400±0.049
38.0	2751.± 13.	228.± 18.	0.900±0.102	0.300±0.054	0.480±0.045
42.7	2770.± 15.	221.± 12.	0.475±0.372	0.400±0.219	0.560±0.067
49.4	2706.± 44.	296.± 40.	0.475±0.127	0.275±0.184	0.560±0.135

Table C4. Derived parameters and errors per aperture for A754#1.

Radius ($''$)	RV (kms^{-1})	σ (kms^{-1})	Log(Age) Gyrs	[Z/H] dex	[E/Fe] dex
-20.8	16512.± 46.	256.±100.	0.800±0.128	-0.275±0.087	0.360±0.088
-10.7	16514.± 14.	143.± 37.	1.075±0.023	-0.330±0.032	0.460±0.063
-6.5	16497.± 21.	202.± 22.	1.175±0.015	-0.225±0.022	0.180±0.040
-4.2	16468.± 19.	274.± 5.	1.175±0.000	0.000±0.023	0.180±0.038
-2.7	16466.± 11.	235.± 7.	1.175±0.000	0.050±0.025	0.270±0.035
-1.6	16461.± 13.	271.± 5.	1.175±0.000	0.125±0.025	0.240±0.033
-0.6	16478.± 11.	295.± 9.	1.175±0.000	0.200±0.015	0.270±0.025
0.4	16463.± 12.	312.± 12.	1.175±0.005	0.250±0.015	0.270±0.025
1.5	16442.± 15.	277.± 6.	1.175±0.008	0.175±0.022	0.210±0.031
2.6	16470.± 18.	254.± 15.	1.125±0.012	0.175±0.028	0.210±0.030
4.0	16444.± 22.	208.± 16.	1.175±0.008	-0.075±0.029	0.270±0.036
6.5	16453.± 37.	254.± 9.	0.950±0.078	0.100±0.057	0.240±0.055
10.9	16450.± 16.	249.± 45.	0.925±0.087	-0.200±0.051	0.210±0.079
20.9	16448.± 33.	162.± 30.	1.175±0.074	-0.500±0.072	0.240±0.076

Table C5. Derived parameters and errors per aperture for A970#1.

Radius ($''$)	RV (kms^{-1})	σ (kms^{-1})	Log(Age) Gyrs	[Z/H] dex	[E/Fe] dex
-7.2	17595.± 25.	244.±118.	1.175±0.097	-0.500±0.081	0.300±0.095
-4.2	17578.± 16.	188.± 11.	1.150±0.051	-0.150±0.035	0.270±0.062
-2.6	17536.± 14.	208.± 14.	1.125±0.027	-0.050±0.039	0.340±0.065
-1.6	17558.± 16.	229.± 13.	1.175±0.004	0.050±0.026	0.270±0.036
-0.6	17522.± 10.	246.± 7.	1.175±0.004	0.175±0.023	0.300±0.034
0.4	17517.± 9.	274.± 14.	1.175±0.000	0.250±0.017	0.270±0.030
1.5	17520.± 4.	256.± 14.	1.125±0.009	0.125±0.022	0.240±0.033
2.5	17557.± 12.	255.± 18.	1.125±0.007	0.000±0.026	0.360±0.051
4.0	17528.± 18.	183.± 30.	1.025±0.034	-0.050±0.032	0.240±0.055
7.1	17573.± 36.	256.± 27.	1.175±0.031	-0.300±0.032	0.300±0.071

Table C6. Derived parameters and errors per aperture for A978#1.

Radius ($''$)	RV (kms^{-1})	σ (kms^{-1})	Log(Age) Gyrs	[Z/H] dex	[E/Fe] dex
-13.6	17736.± 29.	233.± 55.	1.175±0.063	-0.275±0.038	0.240±0.068
-7.5	17714.± 11.	242.± 33.	1.175±0.011	-0.175±0.020	0.150±0.044
-4.4	17729.± 13.	183.± 9.	1.175±0.000	-0.100±0.017	0.210±0.037
-2.6	17724.± 14.	269.± 20.	1.025±0.031	0.075±0.029	0.150±0.031
-1.6	17688.± 13.	285.± 15.	1.100±0.008	0.000±0.024	0.030±0.042
-0.6	17669.± 14.	308.± 15.	1.025±0.025	0.125±0.032	-.060±0.034
0.4	17618.± 10.	301.± 12.	1.000±0.031	0.175±0.037	0.000±0.043
1.5	17632.± 14.	247.± 12.	1.175±0.000	0.000±0.014	0.210±0.031
2.5	17601.± 10.	237.± 21.	1.175±0.007	-0.025±0.027	0.120±0.037
4.2	17607.± 17.	253.± 22.	1.175±0.004	-0.100±0.021	0.210±0.037
7.4	17581.± 19.	248.± 32.	1.175±0.007	-0.200±0.031	0.060±0.064
13.4	17697.± 42.	264.± 23.	1.175±0.020	-0.075±0.026	0.400±0.049